Tuning and Optimization of the Field Distribution for 4-Rod Radio Frequency Quadrupole Linacs

DISSERTATION

zur Erlangung des Doktorgrades
der Naturwissenschaften

vorgelegt beim Fachbereich Physik
der Johann Wolfgang Goethe-Universität
in Frankfurt am Main
von

Janet Susan Schmidt
aus Frankfurt am Main

Frankfurt am Main, 2014
(D 30)

vom Fachbereich Physik der
Johann Wolfgang von Goethe - Universität als Dissertation angenommen.

Dekan:	Prof. Dr. Joachim Stroth
Gutachter:	Prof. Dr. Alwin Schempp
	Prof. Dr. Oliver Kester

Datum der Disputation: 15.07.2014

Contents

0 Zusammenfassung

Der Radiofrequenzquadrupol (RFQ) wird typischerweise in Beschleunigeranlagen als erste Beschleunigungsstruktur nach der Ionenquelle eingesetzt. Mit Hilfe eines hochfrequenten elektrischen Quadrupolfeldes werden Ionen fokussiert und beschleunigt. Zudem ist der RFQ in der Lage aus einem kontinuierlichen Ionenstrahl Teilchenpakete (Bunche) zu formen, die von den nachfolgenden Strukturen benötigt werden. Ziel der vorliegenden Arbeit war die Optimierung der Feldverteilungen im 4-rod RFQ im Bezug auf die Systematisierung des Tuning Prozesses und Untersuchungen zu Randfeldeffekten. Hierbei wurde an vier verschiedenen RFQs für aktuelle Linearbeschleunigerprojekte gearbeitet. Hierzu zählen Upgrades von Injektoren bei Fermi National Laboratory (FNAL) [55] und Los Alamos National Laboratory (LANL) [13] sowie RFQs für neue Beschleunigerkomplexe wie ReA3 am National Superconducting Cylclotron Laboratory (NSCL) an der Michigan State Universität (MSU) [18] und das Tumortherapiezentrum für Ionenbestrahlung MedAustron [23]. Für diese Projekte wurden RFQs im Frequenzbereich von 80–216 MHz entwickelt und gebaut. In den letzten Jahren ist der Bedarf an hoch intensiven Ionenstrahlen mit gleichzeitig besten Strahlqualitäten stark gestiegen. Um die Anforderungen solcher Projekte zu erfüllen, wird das Design und die Fertigung der Beschleuniger stetig weiter entwickelt. Hierbei greifen die verschiedenen Schritte, also die teilchendynamische Auslegung, das HF Design, die mechanische Realisierbarkeit und Rahmenbedingen des Projekts selbst ineinander. In diesem Umfeld wurden im Rahmen dieser Arbeit die Einflüsse von Hochfrequenz (HF) Designelementen auf die Feldverteilungen im 4-rod RFQ untersucht und Simulationsmethoden zur Vorhersage der longitudinalen Spannungsverteilung entwickelt und analysiert. Zusätzlich wurden Simulationen zu Randfeldern der 4-rod Elektroden, die am Strahleingang und -ausgang der Struktur auftreten können, durchgeführt und an Messungen verifiziert. Basierend auf diesen Studien wurde das 4-rod RFQ Design in Bezug auf seine Feldgeometrien weiter entwickelt.

Die grundlegenden Prinzipien des RFQs werden in Kapitel 2 eingeführt. Hier wird das teilchendynamische Design mit den verschiedenen Sektionen der Elektrodenmodulation beschrieben. Diese Modulation entspricht einer sinusoidalen Störung des Quadrupolfeldes der Elektroden, wodurch eine beschleunigende Feldkomponente entsteht. Typischerweise kann das Elektrodendesign anhand von vier Sektionen beschrieben werden. Hierbei wird nach dem Prinzip des adiabatischen Bunchens, durch kontinuierliches Verschieben der Phase des Sollteilchens, der Ionenstrahl in den RFQ eingefangen, fokussiert, gebuncht und schließlich beschleunigt. Die entsprechenden Potentiale werden hergeleitet [59] und die verschiedenen Resonanzstrukturen diskutiert. Hervorgehoben wird hierbei der in Frankfurt entwickelte 4-rod RFQ, ein Leitungsresonator, dessen Modenspektrum näher untersucht wird. Für diesen RFQ Typ wurde in Zusammenarbeit mit C. Y. Tan von FNAL eine Beschreibung anhand seines Ersatzschaltbildes weiterentwickelt und im Folgenden auf das Tuning der longitudinalen Spannungsverteilung angewandt [56]. Die Grundlagen dieses Models werden in Kapitel 2.3 eingeführt.

Im folgenden Kapitel 3 werden die vier RFQ Projekte, an denen im Rahmen dieser Arbeit gearbeitet wurde, vorgestellt. Der ReA3 RFQ bei MSU ist Teil einer Strahlführung zur Nachbeschleunigung abgebremster Ionen, die zur Untersuchung seltener Isotope dient. Dieser 80 MHz RFQ ist 3.5 m lang und ist für cw-Betrieb ausgelegt. Das typische Tastverhältnis für 4-rod RFQs liegt bei ca. 0.1%, somit ist für hohe Tastverhältnisse und besonders für cw-Betrieb ein verstärktes Kühlsystem notwendig. Dieser RFQ wurde 2011 in Betrieb genommen. Der zweite RFQ für schwere Ionen wurde für das Tumortherapie-Zentrum MedAustron entwickelt und gebaut. Hier werden Krebstumore basierend auf den Prinzipien, die bei GSI in Darmstadt und HIT in Heidelberg untersucht wurden, mit Kohlenstoffionen bestrahlt. Dabei wird die charakteristische Energiedeposition im Gewebe, der Bragg-Peak, genutzt um Tumorzellen lokal abzutöten und gleichzeitig das umliegende Gewebe zu schonen. Dieser RFQ wird bei 216 MHz betrieben und ist seit 2013 im Testbetrieb der Anlage. Neben diesen Schwerionenbeschleunigern wurden zwei weitere 200 MHz RFQs für H^--Ionen, bzw. Protonen entwickelt, die bestehende Cockcroft-Walton Beschleuniger ersetzen. Der H^--Injektor am FNAL wurde nach intensiver Testphase [50] 2012 voll in Betrieb genommen. An diesem RFQ wurde ein Großteil der Daten zur Untersuchung des Tuningverhaltens von 200 MHz Strukturen

gesammelt und die Signifikanz von Randfeldeffekten auf die Ausgangsparameter des Strahls untersucht. Die Erkenntnisse aus diesen Studien wurden im Design für den Protonen Injektor an LANL bereits umgesetzt. Dieser RFQ steht zur Zeit kurz vor der Fertigung. Die Kenndaten der RFQs sind in Tabelle 3.1 zusammengefasst.

Im Kapitel 4 werden grundlegende Untersuchungen zur longitudinalen Spannungsverteilung im 4-rod RFQ beschrieben. Die zwei gängigsten Konzepte für diese Verteilung sind zum einen eine konstante Spannung entlang der Elektroden und zu anderen eine zum Beschleunigungsteil hin ansteigende Spannung. Je nach Auslegung des RFQs finden beide Konzepte ihre Anwendung. Abweichungen in der Spannungsverteilung von ihrem Designverlauf haben Auswirkungen auf die Transmission des RFQs, da die Fokussierstärke B direkt proportional zur Elektrodenspannung V ist. Es wurde gezeigt, dass Spannungsminima in der Bunchersektion des RFQs deutlich stärkere Auswirkungen haben, als vergleichbare Änderungen an den Enden der Struktur. In dieser Studie führte eine maximale Abweichung von 30% in der Bunchersektion zu einer Senkung der Transmission um ca. 40%. Dies kann durch Erhöhung der mittleren Spannung ausgleichen werden, was allerdings eine erhöhte Leistungsaufnahme bedingt [50] und damit durch die Auslegung der Verstärker limitiert ist. Desweiteren werden in diesem Kapitel die Einflüsse verschiedener HF-Designparameter auf die longitudinale Spannungsverteilung im Detail untersucht. Dabei handelt es sich um die generelle Geometrie des RFQs wie dem Überhang der Elektroden über die Endstützen hinaus oder dem Abstand der Stützen, genauso wie um Tuningelemente der 4-rod Struktur wie Tuningplatten und dynamische Tuner.

Aufbauend auf diese Basisuntersuchungen werden in Kapitel 5 drei verschiedene Ansätze zur Simulation der longitudinalen Spannungsverteilung untersucht. Die allgemeinste dieser Methoden ist die Simulation mit CST Microwavestudio® (MWS) [35]. Hierbei werden die Feldverteilungen der Moden simuliert und die Spannungsverteilung anhand von Integrationslinien bestimmt. Diese Methode liefert gute Ergebnisse zur relativen Änderung der Spannungsverteilung durch Verschiebung der Tuningplatten. Die Rechendauer solcher Simulationen liegt bei einigen Stunden, was für den direkten Einsatz im Labor ungeeignet ist. Abgesehen davon stimmen die absoluten Verteilungen trotz gezielter Anpassungen der Auflösung des Simulationsbereichs und Simulation

von importieren CAD-Modellen nicht genau genug mit den Messung überein, um MWS sinnvoll im Tuningprozess einzusetzten. Daher wird in den beiden alternativen Simulationsmethoden ein Model auf Grund von Messungen der RFQ Struktur an diese angepasst. Zum einen gibt es hier den von P. Fischer eingeführten Ansatz der Wirkfunktionen [10], der im Rahmen dieser Arbeit untersucht und weiter entwickelt wurde. Dieser Ansatz liefert gute Ergebnisse für RFQs im Frequenzbereich von ca. 100 MHz. Bei höheren Frequenzen um 200 MHz verstärken sich jedoch die Abweichungen zwischen diesem Modell und Messungen, sodass eine weitere Simulationsmethode, die auf dem Ersatzschaltbild des 4-rod RFQs als Kette induktiv gekoppelter Schwingkreise beruht, verfolgt wurde. Dieser Ansatz liefert die höchste Genauigkeit dieser drei Modell im Vergleich zu Messungen an einem 200 MHz RFQ.

Der letzte Schwerpunkt dieser Arbeit sind die Untersuchungen der Randfeldeffekte, die in Kapitel 6 dargestellt sind. Im Vergleich von statischen und resonanten Simulationen treten in der Resonanz deutliche Feldspitzen an den Rändern der Elektroden auf. Diese Peaks sind nicht im teilchendymischen Design des RFQs enthalten und haben abhängig von verschieden Faktoren mehr oder weniger starke Einflüsse auf die Ausgangsparameter des Ionenstrahls. Wichtig ist hierbei die s.g. *Crandall Cell*, eine Übergangszelle am Ende des RFQs, die für eine symmetrische Ausgangsverteilung des Strahls eingesetzt wird. Durch diese Zelle wird die Phase des Sollteilchens beim Eintreten in den Bereich zwischen den Elektroden und Tankwand im Vergleich zum Design ohne Crandall Cell so verschoben, dass die Amplitude des Randfeldes grade im Anstieg bei 90% ihres Maximums ist und damit maximalen Einfluss auf das Teilchen hat. Dies wird bei Betrachtung des Transittime-Faktors dieses Feldpeaks deutlich. Im Fall ohne Crandall Cell liegt die Amplitude an dieser Stelle bei 50% der maximalen Feldstärke an der abfallenden Flanke. In der Studie zu diesen Effekten, wurden verschiedene Parameter zur Minimierung der Randfelder untersucht [51]. Hierbei hat sich vor allem die Öffnung und Positionierung des HF Abschirmung in den Endflanschen des RFQs als Einflussmöglichkeit ergeben [50]. Als Größen zur Quantifizierung des Einflusses der verschiedenen Elemente wurde zum einen die zusätzliche Beschleunigungsspannung, die auf die Teilchen auf Grund der Randfelder wirkt, und zum anderen die Spannung, die zwischen einer Stütze und der Tankwand herrscht, genutzt. Diese *Stützenspannung* dient als Indikator der gleichmäßigen Stromverteilung auf den Stützen.

Aus diesen Untersuchungen ging unter anderem hervor, dass das magnetische Feld um die letzten Stützen mehr Raum braucht, um die volle Stärke, wie an den mittleren Stützen, zu entwickeln. Dies führt zu einer Verbesserung der Feldsymmetrie insgesamt.

Aus der Summe dieser Untersuchungen wurde ein modifiziertes RFQ Model entwickelt, das in Kapitel 7.1 vorgestellt wird. In diesem Model sind drei wesentliche Punkte eingearbeitet: Eine Modifizierung der Positionierung der HF-Abschirmung, verbesserte Geometrie für das magnetische Feld um die letzten Stützen, sowie reduzierte Längen der äußeren HF-Zellen zur Optimierung der Feldverteilung und Positionierung der Tuningelemente.

Zusammenfassend wurde in Messungen und Simulationen gezeigt, dass die Entwicklung von 4-rod RFQs mit hohen Anforderungen und engen Spezifikationen heute möglich ist, wenn klassische Design Codes wie Parmteq mit numerischen Simulationsmethoden wie CST Mircowave® und Particle Studio® sowie modernsten Fertigungsmethoden und verbesserten Strategien im Tuning Prozess der Struktur kombiniert werden.

1 Introduction

In modern injectors for ion accelerator complexes, the Radio Frequency Quadrupole (RFQ) is the standard device for the first acceleration step after the ion source. During the last years the requirements for high intensity beams and high power operation of accelerators have increased a lot, pushing the limits of the machines. The RFQ projects which have been part of this thesis are presented in chapter 3. They include the injector upgrades for the Fermi National Accelerator Laboratory (FNAL) and Los Alamos National Laboratory (LANL) as well as for the new reaccelerator facility ReA3 at Michigan State University (MSU) and the cancer therapy center for ion radiation MedAustron. In this challenging surrounding the careful design of RFQs is really important in order to obtain highest beam quality and the best performance of the machine. The goal of this thesis is to optimize the field distributions in the 4-rod RFQ. Therefore, the influence of RF design elements of the RFQ on its fields has been studied in detail and a simulation method for the longitudinal voltage distribution along the electrodes has been developed. To complete these studies, simulations on the boundary fields of the 4-rod RFQ have been performed and this results have led to an improved RFQ design.

1.1 Design of 4-rod RFQs

The design process of an RFQ can be split into three main parts. In each of them the requirements and limitations of the other parts need to be considered. In the first step, there is the layout of the particle dynamic properties of the accelerating structure with Parmteq$_M$ which fixes the modulation profile of the electrodes, the length of the RFQ and its electrode voltage. The second step is the RF design, where the behavior of the resonant structure is studied and optimized for the operating frequency and the field distributions of the RFQ which have to match the particle dynamics. Here it is possible to observe also the power distribution on the structure for example to support decisions about the required cooling system. This brings us to the last step in the

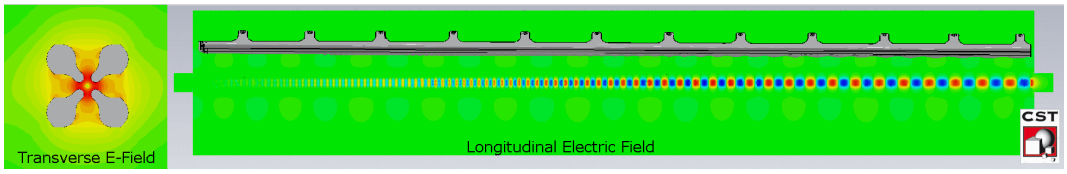

Figure 1.1: The transverse and longitudinal electric field of the RFQ. The transverse quadrupole field focuses the beam and the longitudinal component provides the accelerating potential.

chain, the mechanical design. Based on the results of the RF simulations and using the data from the particle dynamic design, the mechanical setup of the RFQ is elaborated and than cross checked again in RF and particle dynamic simulations.

For the RF simulation of 4-rod RFQs CST Microwave Studio® (MWS) is used. The simulation technique has improved a lot in the last few years, so that detailed simulations of the fully imported technical models are possible and tests using prototypes can be reduced considerably. The simulations can be used to predict the resonant frequency within the range of a few MHz, to study field distributions or the impact of changes in the modulation of the electrodes. An important result from these simulations are the comparisons of mechanical variations in reference to the power consumption of the RFQ.

In the RFQ, it is important to take care of the fringe fields between the electrodes and the tank walls. For the 4-rod structure, this can be done with particle dynamic simulations performed with CST Particle Studio® (PS). It is used to cross check the Parmteq$_M$ design with a focus on the influence of boundary conditions. Especially these simulations on the fringe fields where not possible up to now as a high resolution in the field calculation is necessary to study its effects.

1.2 Electric Field Distribution in the 4-rod RFQ

The electric quadrupole field is the heart of an RFQ. All efforts in RF design and the different types of RFQ structures are performed to provide the electric field distribution that is fixed in the particle dynamic layout. This distribution defines the properties of the ion beam as it travels through the RFQ. The theoretical background of the particle dynamics and the RF properties of the RFQ are given in chapter 2.

Fig. 1.1 shows the distribution of the transverse and longitudinal electric field in a 4-rod RFQ in comparison with the size of an electrode. The transverse fields are dominating the focusing and can be mainly influenced by the electrode voltage, the mean aperture or higher harmonics as well as variations in the longitudinal voltage distribution or a dipole field added onto the quadrupole field. The longitudinal electric field determines the beam in its energy gain and phase bunching.

Inside the RFQ electrodes, the fields are completely defined by the machining of the electrodes' modulation and their potentials. Any aberration of the potential from each electrode can cause a shift in the beam line. In most cases this will do no harm, but as soon as high currents are transported in the quadrupole, these errors can cause changes in the output emittance or even particle losses. Looking at local changes in the potential distribution along the electrodes, particle losses can be generated as the focusing strength of the quadrupole is lowered locally. In chapter 4, studies on the influence of the mechanical parts of the 4-rod RFQ on the longitudinal voltage distribution, the so called *field flatness* are presented. Techniques of its simulation have been developed and are discussed in chapter 5.

As in every part of an accelerating structure, also in the RFQ the boundary conditions require special consideration as they have a strong influence on the RFQ's output parameters like the emittance or output energy for example. In this case boundaries means the end of the electrodes, especially in the context of the gap between the electrodes and the vessel wall with the beam pipe to the next part of the accelerator system. In this part of the 4-rod RFQ, there are a number of parameters influencing the fringe fields of the quadrupole which are discussed in chapter 6.

2 Theory

2.1 The Radio Frequency Quadrupole

The Radio Frequency Quadrupole (RFQ) is a linear accelerator which combines acceleration, focusing and bunching of the beam using electric RF fields of four alternately loaded electrodes. The electric quadrupole field is perturbed with a wave form modulation on the tips of the electrodes following the principles introduced by Kapchinskiy and Tepliakov [16]. The resonant structure around the electrodes can have many different forms depending on the operating parameters like the frequency or the duty cycle. It can be either a cavity or a transmission line resonator. The velocity independent focusing strength of the RF quadrupole and the possibility to bunch a continuous beam in the RFQ explains its advantages in the low energy section of an accelerator complex just after the ion source. As its shunt impedance decreases with $1/\beta^2$ as the acceleration cell length grows with the ratio of the particle velocity to the speed of light β. So the RFQ is used for energies up to 2-3 MeV/u typically [1].

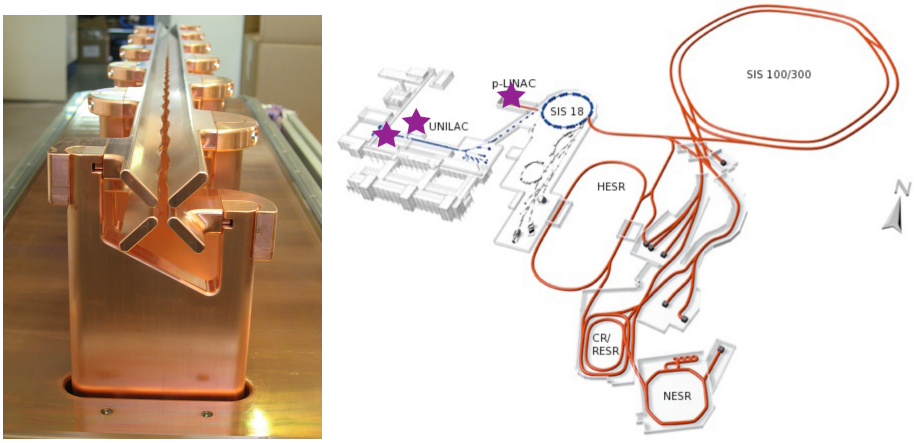

Figure 2.1: The RFQ (left [14]) is the standard accelerator following the ion sources (see stars right) in injectors of modern accelerator complexes like e.g. FAIR [36].

2.1.1 Focusing and Acceleration

In a classical linear accelerator like an Alvarez structure or other drift tube LINACs like Wideröe, IH- or CH-structures, for example, magnetic lenses are added between the accelerating elements to provide focusing. In contrast, the RFQ uses the internal electric quadrupole field of its four electrodes to provide homogeneous electric RF focusing and acceleration. The electrodes are alternately loaded with a potential of $\pm V/2$ to form a quadrupole field as pictured in Fig. 2.2 (left) which can transport the beam in the quadrupole channel. In the static case, a beam in the quadrupole experiences a focusing force in one and a defocusing force in the other plane. Due to the RF the polarization of the electrodes changes sign with its period resulting in an alternating focusing and defocusing force in one plane as the beam travels through the structure. Because of the radial gradient of the quadrupole field, this chain of lenses results in an overall focusing effect following the Alternating Gradient Focusing [6] method as illustrated in Fig. 2.2 (right). The application limit of this method lies in the size of the cells L which has to be big compared to the aperture a of the quadrupole $L \ll a$.

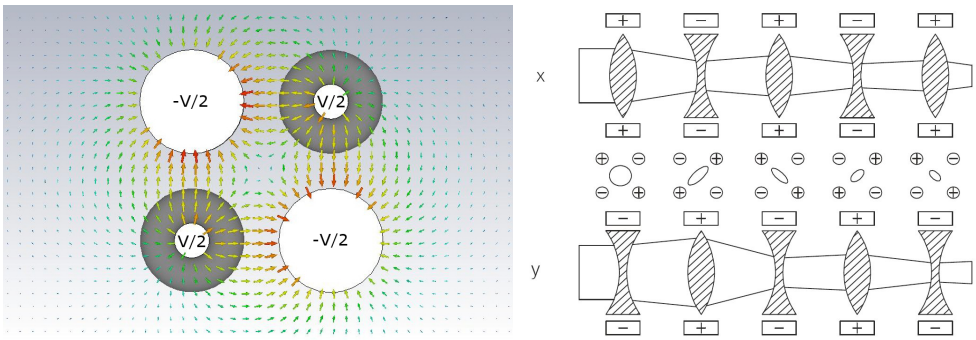

Figure 2.2: Alternating gradient focusing in the quadrupole field of the RFQ. In one plane the beam is alternately focused and defocused leading to an overall focusing effect in both transverse planes.

The acceleration component of the electric field is generated by applying a modulation profile onto the quadrupole electrodes as it was introduced by Kapchinskiy and Tepliakov [16]. In the picture of the electric field lines of a sinusoidal modulated electrode (Fig. 2.3) the perturbation of the field is visible. A wave profile on the electrodes forms acceleration cells with a mid to mid distance of $\beta\lambda/2$ with β describing the ratio of the particles velocity to the speed of light and λ the RF wavelength. Every second of these cells is filled

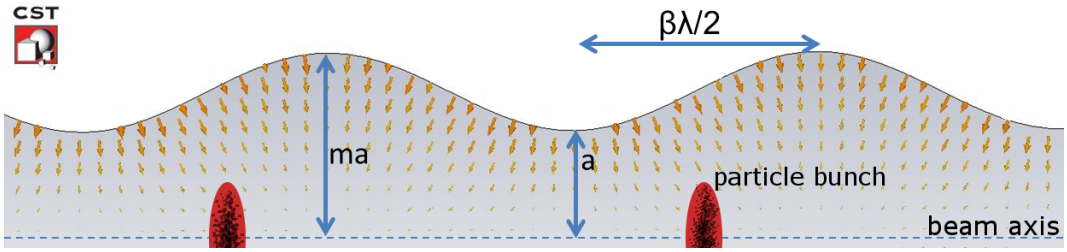

Figure 2.3: Particle bunches (red) in the electric field of the modulated quadrupole. A sinusoidal modulation on the tips of the electrodes forms acceleration cells with the length of $\beta\lambda/2$. The aperture a corresponded to the minimal distance between the electrodes and the beam axis. Its product with the modulation factor m defines its the maximum.

with a bunch of ions, so that the bunch to bunch distance is $\beta\lambda$. As the length of the acceleration cell is proportional to β, it gets longer along the RFQ. But this is not the only value that has to be adapted for each acceleration cell. Each of them is defined by two additional geometrical values, the aperture a which is the minimum distance from the beam axis (dashed line in Fig. 2.3) and the modulation factor m whose product ma is the maximal distance in an acceleration cell.

2.1.2 Sections in the Electrode Design of RFQs

By variation of the aperture, the modulation and the cell length the profile of the electrodes is shaped so that different sections of the particle dynamics in the RFQ are generated. These sections which are shown in Fig. 2.4 are used to focus and to bunch a DC beam from the ion source and to accelerate the beam with an electric field. First of all the beam from the ion source is captured in a short section of typically four cells with $m = 1$, the *radial matcher* (RM). A large acceptance of the RFQ is needed to avoid losses at this critical point. This is realized by setting the synchronous phase *Phi* Φ_S of the design particle to $-90°$. On this phase, the separatrix captures the maximum ratio of particles [59]. The beam from the ion source is continuous in most applications of RFQs and is bunched in the RFQ itself. To prepare the beam for bunching it is focused transversely in the *shaper* section and Φ_S begins to be shifted to a value closer to the acceleration point, e.g. -70 to $-80°$. This is continued in the *buncher* section where the bunching takes place. Special for the bunching in the RFQ is the concept of adiabatic bunching. Bunching in the longitudinal

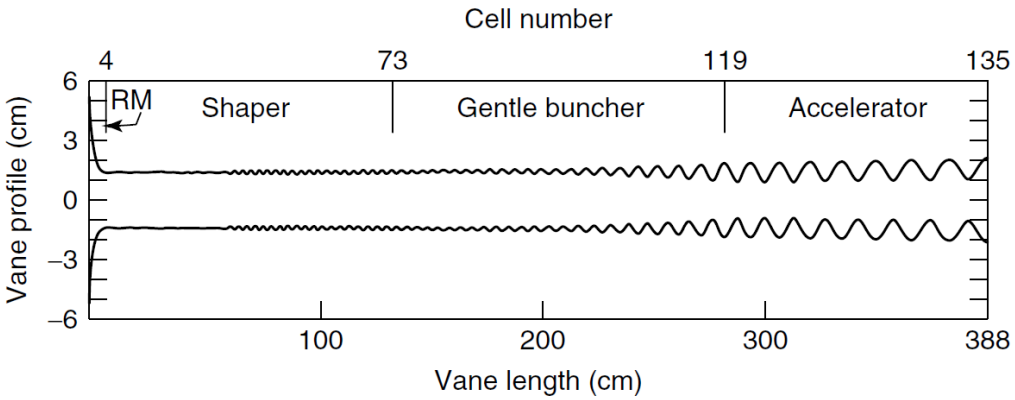

Figure 2.4: Scheme of the typical electrode design of an RFQ [59]. The beam is captures in the radial matcher, then focused and bunched in the shaper and the gentle buncher, before it is accelerated in the last section.

phase space can lead to a blow up of the beam transversely. This effect can be described by the development of the transverse emittance along the structure. The basic idea of adiabatic bunching is to change the parameters of the acceleration cells slowly from cell to cell, so that the geometric bunch length is keep constant which is controlled by a constant length of the separatrix. This can be expressed by the product of β of the synchronous particle and the phase length of the separatrix Ψ being constant.

$$\beta_s \cdot \Psi = \text{constant} \tag{2.1}$$

In the buncher section Φ_S is fully shifted to typically -30 to $-40°$ and the first acceleration occurs which is completed in the last, the *acceleration* section. Here, the phase and the modulation profile do not change much any more and the synchronous energy W_{Syn} grows faster to the output energy of the RFQ.

A short summary of this design which follows the principles set by the Los Alamos Design is given in [31] or [58]. For more detailed information refer to [59] and [8]. Fig. 2.5 pictures the development of W_{syn} and Φ_S in comparison with the geometrical modulation profile after the radial matcher for the FNAL-RFQ. This example follows the design presented in [42] that is optimized for shorter RFQ structures. In comparison to classical accelerator structures like Wideröe the RFQ including adiabatic bunching on a short length are only possible because the RFQ combines focusing and accelerating forces in its electrode's continuous potential without drift tubes that need to have a minimum length for additional focusing magnets.

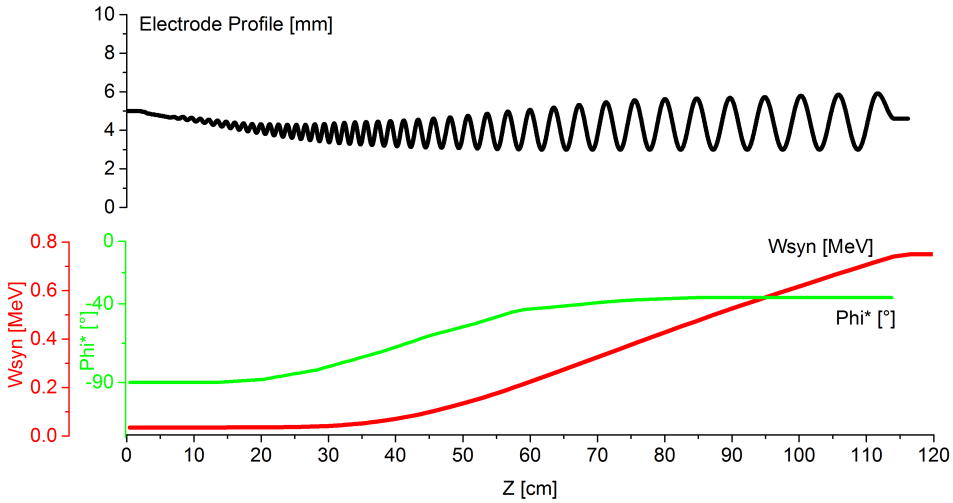

Figure 2.5: Energy and phase evolution for the reference particle for the example of the FNAL RFQ. It is compared with the electrode profile after the radial matcher. This design is a modification of the standard "Los Alamos Design" for short RFQ structures following the principles described in [42].

2.1.3 The Potential Function

To describe the field in the RFQ the Helmholtz equation

$$\nabla^2 \mathbf{E} + k^2 \mathbf{E} = 0 \tag{2.2}$$

needs to be solved. This wave equation is used for a harmonic time-oscillating field $\mathbf{E}$ in a charge-free space where k is the wave number $k = \omega/c = 2\pi/\lambda$. In these geometric scales, the electric field is concentrated around the beam line are small compared to the RF wavelength λ, and thus the geometric term $\nabla^2 \mathbf{E}$ dominates the RF term $k^2 \mathbf{E}$. The magnetic field in this area can be neglected and with it the perturbation of the electric field by inducted ones (Faraday's law). This situation allows the use of the *quasistatic approximation* so that instead of the Helmholtz equation, only the Laplace equation needs to be solved for a scalar potential U.

$$\nabla^2 \mathbf{E} = 0 \tag{2.3}$$

This potential U can be written in polar coordinates, generally as a constant potential V with a sinus oscillation in time.

$$U(r,\theta,z,t) = V(r,\theta,z)\sin(\omega t + \Phi) \tag{2.4}$$

Separating transverse and longitudinal components the general potential function leads to

$$V(r,\theta,z) = \sum_{s=0}^{\infty} A_s r^{2(2s+1)} \cos(2(2s+1)\theta) + \sum_{n=1}^{\infty}\sum_{s=0}^{\infty} A_{ns} I_{2s}(knr)\cos(2s\theta)\sin(knz) \tag{2.5}$$

For RFQ design codes like *Parmteq*, there are several ways to find a potential function to use in the calculation of particle dynamics of the field. One way is to simplify the general potential with a multipole approximation. The typical two-term potential function is

$$V(r,\theta,z) = A_0 r^2 \cos(2\theta) + A_{10} I_0(kr)\cos(kz) \tag{2.6}$$

In this case k is defined as $k = {}^{2\pi}/_{L}$ with the modulation period $L = \beta_s \lambda$. I_0 is the modified Bessel function $I_0(\nu) \cong 1 + {}^{\nu^2}/_{4}$ while A_0 and A_{10} are geometrical factors including parameters like the aperture a and the modulation factor m. Because of the separation of the transverse and longitudinal part of the potential, the first term with A_0 is often referred to as the focusing term and the second, with A_{10} is labeled as the acceleration term.

$$\begin{aligned} A_0 &= \frac{V_0}{2a^2}\frac{I_0(ka) + I_0(kma)}{m^2 I_0(ka) + I_0(kma)} \\ A_{10} &= \frac{V_0}{2}\frac{m^2 - 1}{m^2 I_0(ka) + I_0(kma)} \end{aligned} \tag{2.7}$$

This two-term potential is the simplest way to deal with the problem. Modern RFQ codes use higher order terms up to the order of eight [59]. Another possibility is, for example, to perform a numerical calculation on a grid as it is described in [32]. This approach is especially reasonable for high power structures where high currents have to be transported through the electrodes and the fields at the boundaries of the quadrupole channel have a higher influence on the beam than for low currents.

From this point, after the potential function is defined, the field can be calculated with the derivative of the potential $U(r, \theta, z, t) = V(r, \theta, z) \sin(\omega t + \Phi)$.

$$E = -\nabla U \tag{2.8}$$

2.2 Resonant Structure and RF Simulation of the 4-rod RFQ

The resonant structure of the RFQ to generate the electrode voltage can be realized in different ways. In general they can be divided into two groups of RFQs, the cavity and the transmission line resonators. The cavity resonators are based on transverse electric (TE) modes with currents flowing all over the structure and the cavity walls. The most important one of these structures is the 4-vane RFQ. In contrast, the second one of these two most common RFQs, the 4-rod RFQ, is a transmission line resonators, formed by a chain of $\lambda/4$-resonators. Its fields are concentrated around the acceleration structure while the vessel walls are almost current free. Fig. 2.6 shows the 4-vane and 4-rod structure with its characteristic field distributions.

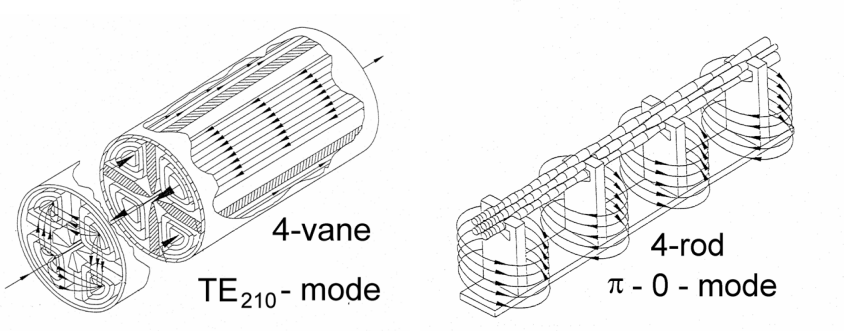

Figure 2.6: 4-vane and 4-rod RFQ. The 4-vane type is a cavity resonator with the operating mode TE_{210}, typically used for operating frequencies above 250 MHz. The 4-rod type is the standard choice for lower frequencies. It is a transmission line resonator working in the π-0 mode (see section 2.2.1).

There are other designs like IH-RFQs, Spiral-RFQs and many more. A few examples are given in Fig. 2.7. The decision of which type of RFQ to use is defined by many different parameters, especially the operating frequency and the implemented power.

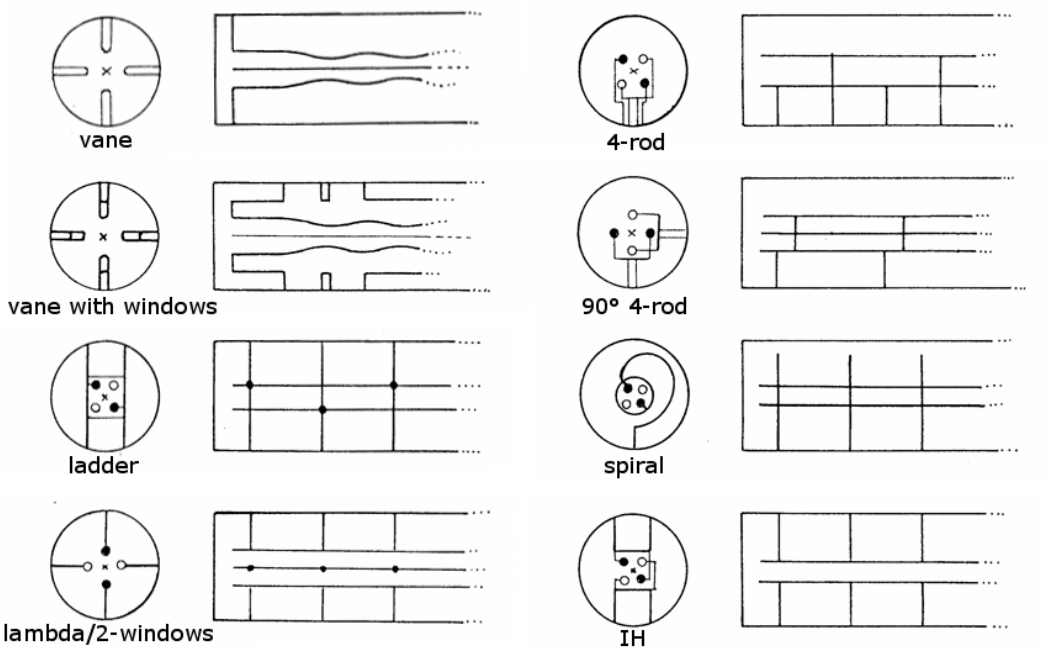

Figure 2.7: Examples of the various RFQ resonators types [45]. Each of them has a special characteristics optimized for a range of applications.

2.2.1 The Resonator Modes

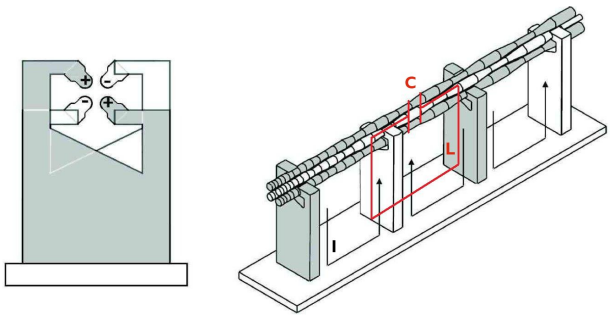

Figure 2.8: The 4-rod RFQ as a chain of LC resonators. The capacitance is concentrated on the quadrupole electrodes where the electric field is located. The inductance is associated with the currents on the stems and base plate.

A 4-rod RFQ consists of a chain of $\lambda/4$-resonators. A simplified model of the resonator is a chain of LC oscillators with the electrodes corresponding to the capacitance, while the inductance is given by the current path along the stems and the ground plate or tuning plate (compare Fig. 2.8). And thus, a pair of two neighboring stems with the electrodes and ground plate in between forms one RF cell of the resonator chain.

The spectrum of an RFQ is important for the evaluation of possible perturbations of the operating mode by higher order modes that are close in frequency and might be excited too. A typical example for that situation is the operating quadrupole mode of the 4-vane RFQ (TE_{210}) and its corresponding dipole mode. In this case, a careful RF design has to make sure that the two modes are separated artificially by special elements. In contrast to the 4-vane RFQ, the operating mode of the 4-rod is the lowest mode in the spectrum and the first higher order mode is typically about 20 – 30 MHz above it.

The labeling of the modes in the spectrum can be based on the phase shift between each RF cell

$$\varphi = \frac{q\pi}{N} \tag{2.9}$$

with $q = 0, 1, ..., N$ for $N+1$ RF cells [57] [34]. The operating mode of the 4-rod RFQ is the $\pi - 0 - mode$. This indication describes the contrary distributions of the electric field E and magnetic field H in this resonant structure. In the operating mode ($q = 0$) the potentials on the electrodes of the RFQ need to be constant, so the electric field shows no phase shift from cell to cell ($0 - mode_E$).

In parallel the direction of the electric currents on the stems are contrary on each stem so that the magnetic field has the opposite sign from RF cell to RF cell ($\pi - mode_H$).

$$mode_E = \frac{q\pi}{N} \qquad mode_H = \frac{(N-q)\pi}{N} \tag{2.10}$$

The normal E-field components on the electrodes and the current distribution on the stems for the first two modes with $q = 0$ and $q = 1$ are presented in Fig.2.9. This distribution lead to the alternating charge of neighboring electrodes to form the quadrupole field.

The full spectrum of the FNAL-RFQ up to 400 MHz calculated with MWS is shown in Fig.2.10. There are two groups of transverse modes distinguished in the spectrum – the quadrupole modes and the dipole or mixed modes. This additional information about the transverse distribution of the electric field is needed for the complete description of the field characterization in the 4-rod RFQ because there are more than one mode for the same q which differ only in the transverse field. Especially for higher modes it is sometimes difficult to determine the transverse mode. The first two modes in the spectrum are quadrupole modes at 152.9 MHz with $q = 0$ and 40 MHz higher at 192.1 MHz

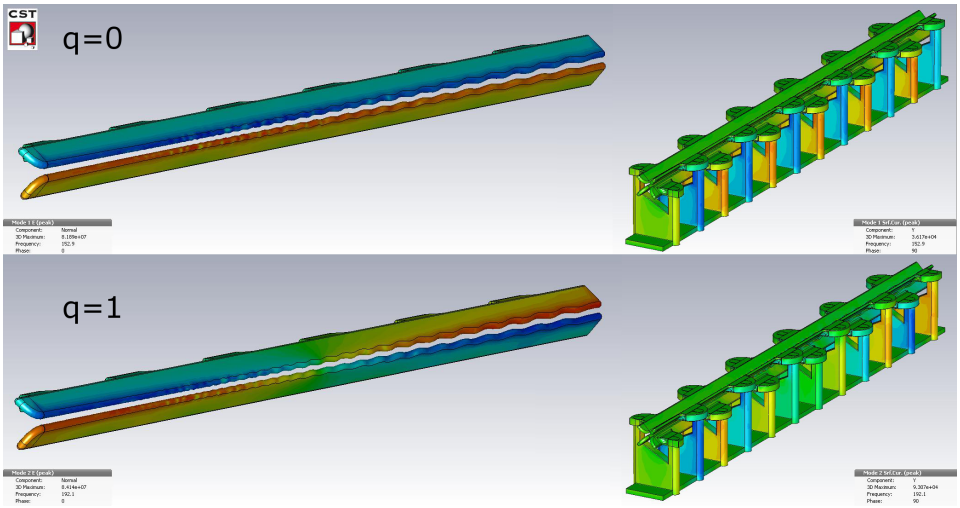

Figure 2.9: The normal electric field (left) and the currents (right) of the 4-rod RFQ's ground mode $\pi - 0$ ($q = 0$) and first higher order mode ($q = 1$).

with $q = 1$. The mode with a dipole potential on the electrodes occurs about 125 MHz above the operating mode without any tuning. This is one of the points separating the 4-rod and 4-vane RFQs. In the 4-vane structure the operating mode TE−210 is close to a dipole mode [59] and artificial modifications are used to increase their distance in frequency.

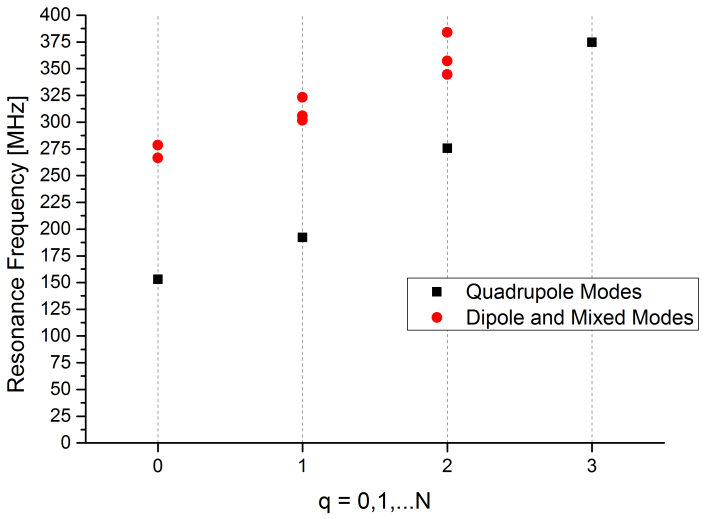

Figure 2.10: The dispersion relation of the FNAL RFQ up to 400 MHz calculated by CST MWS [56]. The first two modes who's fields are shown in Fig. 2.9 are quadrupole modes and the first dipole like mode can be found about 125 MHz above the operating mode.

2.2.2 RF Simulation

The RF design of the 4-rod RFQ structure will be discussed in more detail here. There are a few simulation tools to calculate electromagnetic field distributions in resonators. A classical 2D-simulation code is SUPERFISH [15], but as the 4-rod RFQ does not have any cylindrical symmetry 3D-codes need to be used like the MWS code by CST [35].

The theory which describes the simulation method of CST for calculating the electromagnetic field distributions is the "Finite Integration Technique". The basic idea of this method is to divide the calculation domain into two orthogonal grids where the electric and magnetic fields on the edges are determined by solving Maxwell's equations. More detailed information about the numerical methods can be found in [60] and [61].

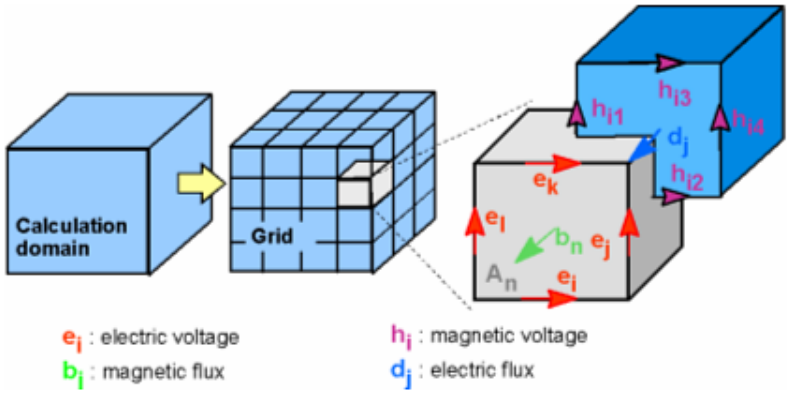

Figure 2.11: Finite Integration Technique for the simulation of the field distributions in CST studio. The calculation domain is divided into grids which are used to solve Maxwell's equations. [35]

Fig. 2.12 shows a modern 4-rod RFQ simulation model together with an example of a possible mesh setup and the fixpoints of the mesh. Fixpoints are certain points which define the edges and details of the resonant structure where the calculation mesh needs to be concentrated in order to have optimal simulation results. These example pictures show the standard meshing of such a structure without further optimization of the meshing. Depending on the simulation purpose, the mesh needs to be refined locally.

For a simulation of the resonance spectrum a standard meshing with fixpoints all over the structure would be suitable, but for a simulation of detailed field distributions in a certain region like the beam axis the mesh needs to be more dense and uniform there. In the recent versions this can be realized in the required details with additional mesh refining components and different choice of fixpoints.

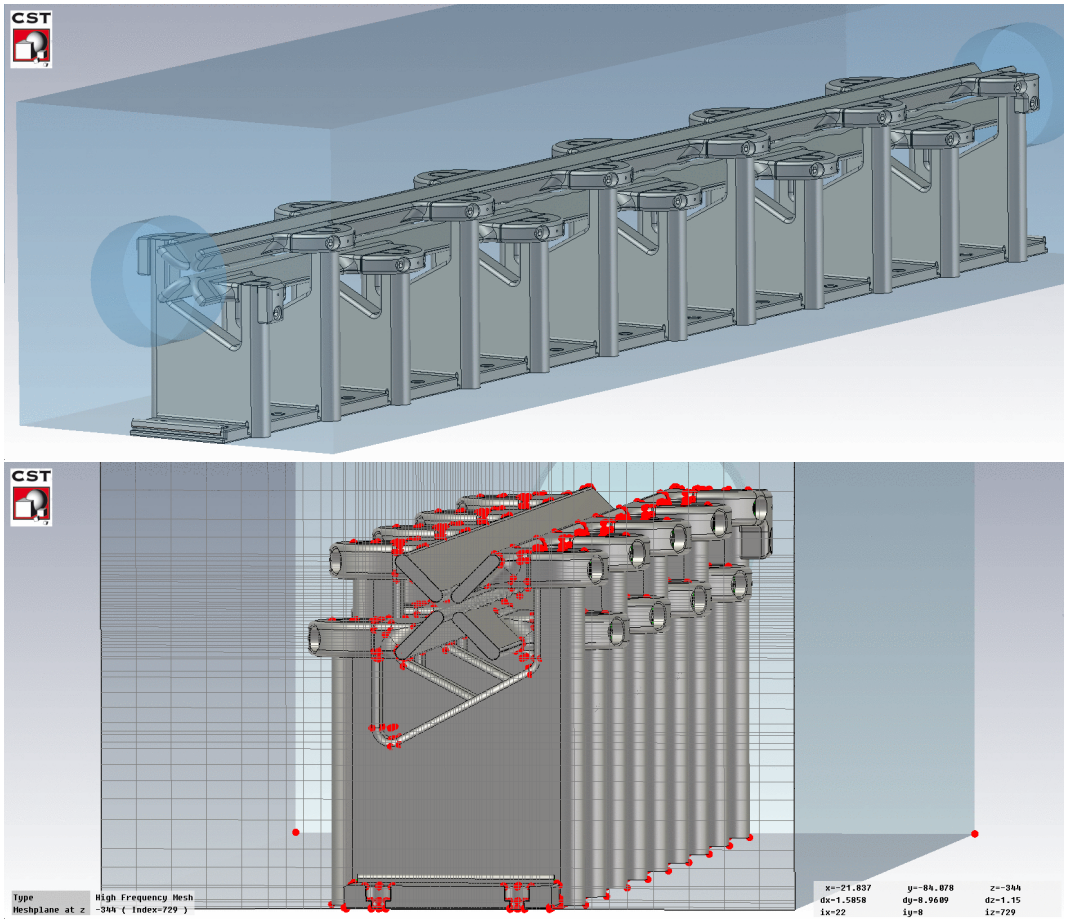

Figure 2.12: Imported CAD models for full 3D analysis of the RFQ with simulation of field and power distributions and particle dynamic studies. The meshing of the structure is important for the accuracy of simulation results and needs to be adapted to the desired observable.

2.3 Lumped Circuit Model of the 4-rod RFQ

The modeling of an accelerator by a lumped circuit model of coupled resonators is a standard technique in the tuning of accelerators. Examples for the application of this theory for 4-vane RFQs can be found in [44], [37] and [17]. The lumped circuit of 4-rod RFQs has been introduced for example by J. X. Fang and A. Schempp in [9]. This model has been refined and further developments have been done for the application in tuning of the 4-rod RFQ in a collaboration with C. Y. Tan from FNAL. The results of these studies are presented in detail in [56].

The model is formed as a chain of inductively coupled LC resonators like it was introduced in section 2.2.1. From the sketch that is shown in Fig. 2.8 the 4-rod RFQ can be translated into a model of LC circuits as shown in Fig. 2.13. In this model each RF cell is characterized by a capacitance C_k and an inductance L_k. Here, the alternating direction of the inductor's "winding" that is marked as dots in Fig. 2.13 needs to be taken into account. The RF cells are numbered with $k = 0...N$, where cell $k = 0$ or N are half cells at the begin and end of the RFQ and $k = 1...(N-1)$ are the full RF cells. The neighboring cells are coupled with the coupling constant $2a_1$, while $2a_2$ is the constant for the second neighbor coupling.

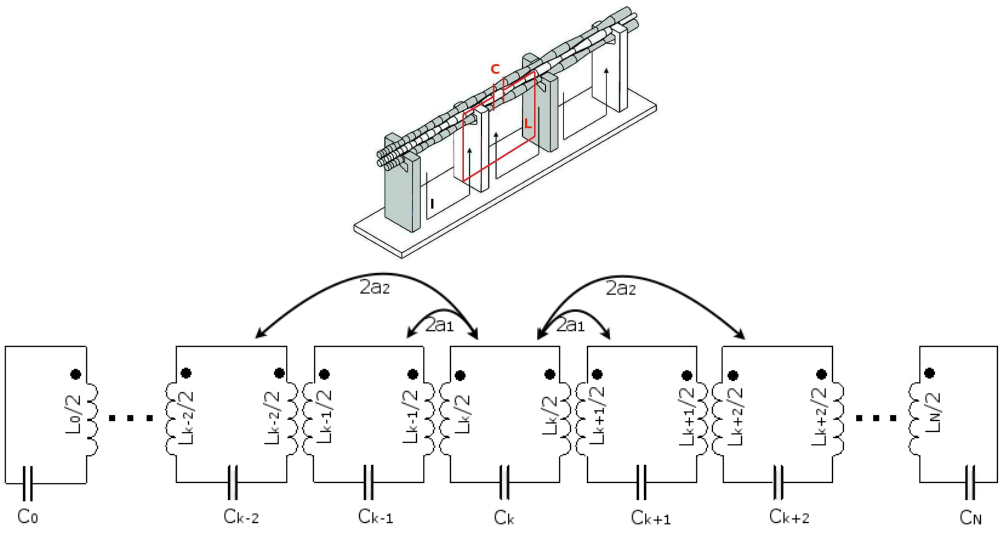

Figure 2.13: Lumped Circuit Model of the 4-rod RFQ. The RFQ as a chain of LC-resonators translated into a lumped circuit model of inductively coupled cells. In this model coupling between neighboring and next neighboring cells is included.

At resonance $\omega_0 = 2\pi f_0$, in each cell a current J_k is induced. For the operating $\pi-0-mode$ of the 4-rod RFQ the induced currents from a $\pi-mode$, as it is given by equation 2.10 from section 2.2.1.

For the analysis of the model, Kirchhoff's law of the voltage in closed circuits can be adapted.

$$\sum U_i = 0 \tag{2.11}$$

Here the two cases of the boundary cells and the middle cells can be distinguished. For the first cell $k = 0$ and the last cell $k = N$, Kirchhoff's equation can be written as

$$\begin{aligned} 0 =& \frac{1}{i\omega C_{0/N}} J_{0/N} + \frac{1}{2} i\omega L_{0/N} J_{0/N} \\ & - i a_1 \omega \sqrt{L_{0/N} L_1} J_{1/(N-1)} \\ & - i a_2 \omega \sqrt{L_{0/N} L_{2/(N-2)}} J_{2/(N-2)} \end{aligned} \tag{2.12}$$

From here, the two equations for the boundary cells are

$$0 = -(1 - \frac{1}{2}\omega^2 C_0 L_0) J_0 - a_1 \omega^2 \sqrt{L_0 L_1} C_0 J_1 - a_2 \omega^2 \sqrt{L_0 L_1} C_0 J_2 \tag{2.13}$$

and

$$0 = -(1 - \frac{1}{2}\omega^2 C_N L_N) J_N - a_1 \omega^2 \sqrt{L_N L_{N-1}} C_N J_{N-1} - a_2 \omega^2 \sqrt{L_N L_{N-2}} C_N J_{N-2} \tag{2.14}$$

In general, Kirchhoff's equation for one cell k of this model is defined by

$$\begin{aligned} 0 =& - a_2 \omega \sqrt{L_{k-2} L_k} C_k J_{k-2} - a_1 \omega \sqrt{L_{k-1} L_k} C_k J_{k-1} \\ & - (1 - \omega^2 L_k C_k) J_k \\ & - a_1 \omega \sqrt{L_{k+1} L_k} C_k J_{k+1} - a_2 \omega \sqrt{L_{k+2} L_k} C_k J_{k+2} \end{aligned} \tag{2.15}$$

Where in this notation for every index $(k-i) < 0$ or $(k+i) > N$ with $i = 1$ or 2, the element is equal 0.

In the next step, the equations for each cell can be transformed into a matrix system to form an eigenvalue problem.

$$0 = (\mathbf{U} - \lambda^2 \mathbf{I})\mathbf{J} \tag{2.16}$$

Here, the currents in the cells correspond to the eigenvector $\mathbf{J}$ and the eigenmode is defined by the eigenvalue λ^2.

$$\mathbf{J} = \begin{pmatrix} J_0 \\ J_1 \\ J_2 \\ . \\ . \\ J_{N-1} \\ J_N \end{pmatrix}, \qquad \lambda^2 = \frac{1}{\omega^2} \tag{2.17}$$

While the matrix $\mathbf{I}$ is the identity matrix with the entries 1 on the main diagonal and 0 in all other elements, the matrix $\mathbf{U}$ contains the information of the circuit model.

$$\boldsymbol{U} = \begin{pmatrix} m_{0,0}C_0 & m_{0,1}C_0 & m_{0,2}C_0 & 0 & ... & ... & 0 \\ m_{0,1}C_1 & m_{1,1}C_1 & m_{1,2}C_1 & m_{1,3}C_1 & \ddots & & \vdots \\ m_{0,2}C_2 & m_{1,2}C_2 & \ddots & \ddots & \ddots & \ddots & \vdots \\ 0 & m_{1,3}C_3 & \ddots & \ddots & \ddots & m_{N-3,N-1}C_{N-3} & 0 \\ \vdots & \ddots & \ddots & \ddots & \ddots & m_{N-2,N-1}C_{N-2} & m_{N-2,N}C_{N-2} \\ \vdots & & \ddots & m_{N-3,N-1}C_{N-1} & m_{N-2,N-1}C_{N-1} & m_{N-1,N-1}C_{N-1} & m_{N-1,N}C_{N-1} \\ 0 & ... & ... & 0 & m_{N-2,N}C_N & m_{N-1,N}C_N & m_{N,N}C_N \end{pmatrix} \tag{2.18}$$

with

$$\left.\begin{array}{lll} m_{0,0} & = & \frac{1}{2}L_0, \qquad m_{N,N} = \frac{1}{2}L_N \qquad m_{k,k} = L_k \\ m_{k-1,k} & = & -a_1\sqrt{L_{k-1}L_k} \qquad m_{k-2,k} = -a_2\sqrt{L_{k-2}L_k} \end{array}\right\} \quad k = 1, \ldots, N-1 \tag{2.19}$$

2.3.1 Analysis of the Simplified Model

For the analysis of the oscillating behavior of the structure, the model is simplified so that each RF cell has the same resonance frequency $\omega_c = {}^1/\sqrt{LC} = \lambda_c$. This postulation can be met when all inductances L_k are set to be the same value and the capacitance C_k is the same for all full RF cells and doubled in the boundary cells.

$$\begin{aligned} L_k &= L \;\forall\; k \\ C_k &= \begin{cases} C & for\ k = 1...(N-1) \\ 2C & for\ k = 0\ or\ N \end{cases} \end{aligned} \tag{2.20}$$

When these postulations are included in equation 2.19, the matrix $\mathbf{U}$ can be transferred to

$$\begin{aligned} \boldsymbol{U}(a_1, a_2) &= \lambda_c^2 \cdot \boldsymbol{U}_0(a_1, a_2) \\ &= \lambda_c^2 \begin{pmatrix} 1 & -2a_1 & -2a_2 & 0 & \dots & \dots & \dots & \dots & 0 \\ -a_1 & 1 & -a_1 & -a_2 & \ddots & & & & \vdots \\ -a_2 & -a_1 & 1 & -a_1 & -a_2 & \ddots & & & \vdots \\ 0 & -a_2 & -a_1 & 1 & -a_1 & -a_2 & \ddots & & \vdots \\ \vdots & \ddots & \ddots & \ddots & \ddots & \ddots & \ddots & \ddots & \vdots \\ \vdots & & \ddots & \ddots & \ddots & \ddots & -a_1 & -a_2 & 0 \\ \vdots & & & \ddots & \ddots & \ddots & 1 & -a_1 & -a_2 \\ \vdots & & & & \ddots & \ddots & -a_1 & 1 & -a_1 \\ 0 & \dots & \dots & \dots & \dots & 0 & -2a_2 & -2a_1 & 1 \end{pmatrix} \end{aligned} \tag{2.21}$$

The approach that was used for the analysis of this system follows the perturbation theory known from quantum mechanical problems. In the first step, the second neighbor coupling is neglected with $a_2 = 0$ so that the system can be characterized. Based on this solution, the influence of a_2 can be added again as a perturbation of the system.

A numerical calculation of the eigenvectors of the system is presented as the blue line in Fig. 2.14 for different modes.

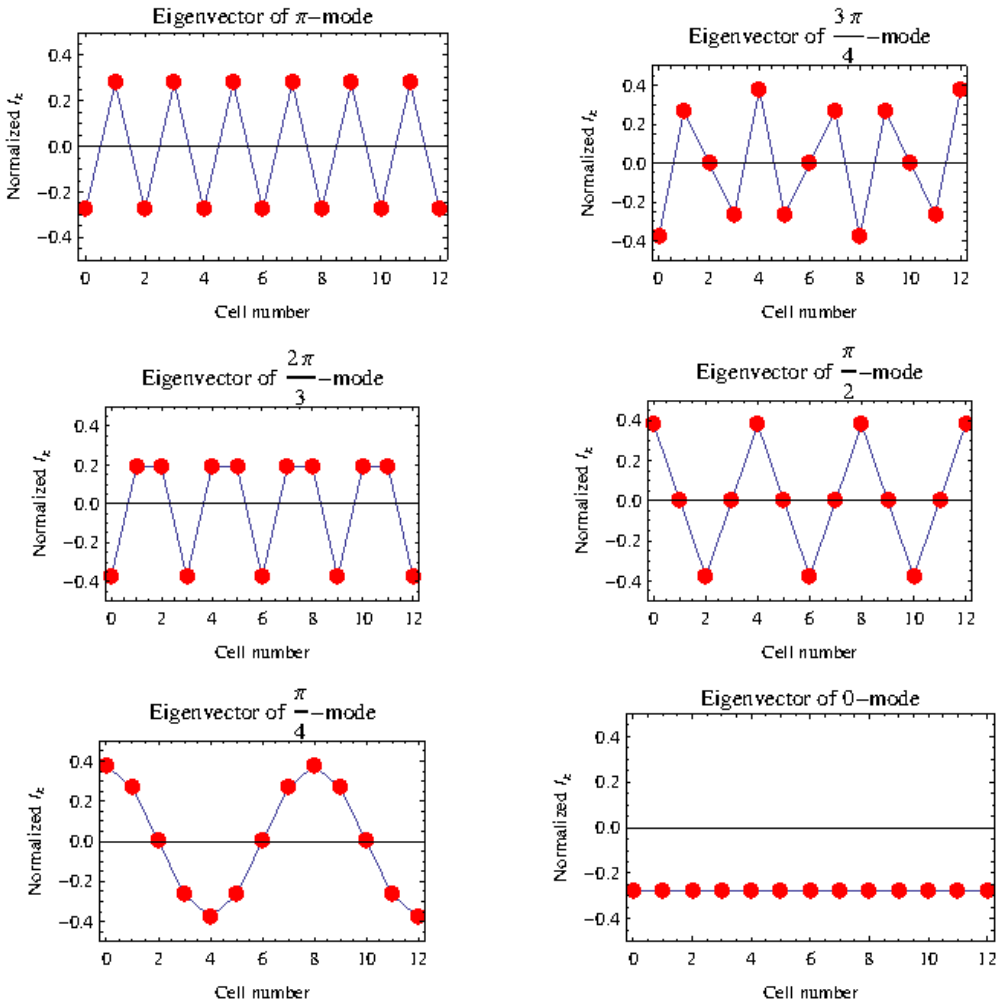

Figure 2.14: The numerically calculated eigenvectors (blue line) which correspond to the current in the system compared to the results of the ansatz in equation 2.21 (red dots). For all these modes they match exactly. [56]

Following this method an ansatz for the eigenvectors of $\mathbf{U}_0(a_1, 0)$ can be chosen as

$$\boldsymbol{J}_n = A_n \begin{pmatrix} \cos\frac{0\times n\pi}{N} \\ \cos\frac{1\times n\pi}{N} \\ \cos\frac{2\times n\pi}{N} \\ \vdots \\ \cos\frac{(N-1)\times n\pi}{N} \\ \cos\frac{N\times n\pi}{N} \end{pmatrix} \qquad \text{for } n = 0, \ldots, N \tag{2.22}$$

In this ansatz, n is the index of the mode where $n = 0$ is the $0 - mode$ when the currents in the RF cells all have the same phase and $n = N$ the $\pi - mode$ when the phase is contrary from cell to cell. A_n is the inverse of the eigenvector's norm $\| \boldsymbol{J}_n \|$.

$$A_n = \begin{cases} \frac{1}{\sqrt{\frac{N}{2}+1}} & for\ n = 1...(N-1) \\ \frac{1}{\sqrt{N+1}} & for\ n = 0\ or\ N \end{cases} \tag{2.23}$$

Using the matrix $\boldsymbol{J}$ formed by the eigenvectors $\boldsymbol{J}_n$ it can be shown (see [56])that the ansatz is valid and $\boldsymbol{J}_n$ are the eigenvectors of $\mathbf{U}_0(a_1, 0)$ because

$$\boldsymbol{J}^{-1}\boldsymbol{U}_0(a_1, 0)\boldsymbol{J} = \begin{pmatrix} \Lambda_0 & 0 & \ldots & \ldots & 0 \\ 0 & \Lambda_1 & \ddots & & \vdots \\ \vdots & \ddots & \ddots & \ddots & \vdots \\ \vdots & & \ddots & \ddots & 0 \\ 0 & \ldots & \ldots & 0 & \Lambda_N \end{pmatrix} = \boldsymbol{\Lambda} \tag{2.24}$$

with the eigenvalues of $\mathbf{U}_0(a_1, 0)$ given by

$$\Lambda_n = 1 - 2a_1 \cos\frac{n\pi}{N} \text{ for } n = 1...(N-1) \tag{2.25}$$

When the eigenvectors and eigenvalues of the unperturbed system $\boldsymbol{J}_n$ and Λ_n are known, the second neighbor coupling for $a_2 \ll a_1$ can be introduced with an extension $\delta\mathbf{U}_0(a_2)$. In this case

$$\begin{aligned}\boldsymbol{U}(a_1,a_2) &= \boldsymbol{U}_0(a_1,0) + \delta\boldsymbol{U}_0(a_2) \\ &= \boldsymbol{U}_0(a_1,0) + \begin{pmatrix} 0 & 0 & -2a_2 & 0 & \dots & \dots & \dots & \dots & 0 \\ 0 & 0 & 0 & -a_2 & \ddots & & & & \vdots \\ -a_2 & 0 & 0 & 0 & -a_2 & \ddots & & & \vdots \\ 0 & -a_2 & 0 & 0 & 0 & -a_2 & \ddots & & \vdots \\ \vdots & \ddots & \ddots & \ddots & \ddots & \ddots & \ddots & \ddots & \vdots \\ \vdots & & \ddots & \ddots & \ddots & \ddots & 0 & -a_2 & 0 \\ \vdots & & & \ddots & \ddots & \ddots & 0 & 0 & -a_2 \\ \vdots & & & & \ddots & -a_2 & 0 & 0 & 0 \\ 0 & \dots & \dots & \dots & \dots & 0 & -2a_2 & 0 & 0 \end{pmatrix}\end{aligned} \tag{2.26}$$

As the perturbation approach is based on quantum mechanical methods the corresponding nomenclature of "kets" and "bras" will be used. So the eigenvector $\boldsymbol{J}_n$ for the eigenvalue Λ_n will be written as $|\Lambda_n\rangle$. But the matrix $\mathbf{U}_0(a_1,0)$ is not symmetric because of its first and last line and so it has to be proved that the analysis is based on an orthonormal set of eigenvectors. It can be shown ([56]) with $(\boldsymbol{J}^{-1})_n$ as the (n+1)'th row of the inverse matrix of $\boldsymbol{J}$ that the orthonormality condition is satisfied.

$$\langle\Lambda_n| = (\boldsymbol{J}^{-1})_n \quad \text{so that} \quad \langle\Lambda_n|\Lambda_l\rangle = \delta_{nl} \quad \text{and} \quad \langle\Lambda_n|\mathbf{U}(a_1,0)|\Lambda_l\rangle = \Lambda_k \tag{2.27}$$

This allows the expression of the eigenvector $|\Lambda'_n\rangle$ of $\mathbf{U}_0(a_1,a_2)$ by

$$\begin{aligned} |\Lambda'_n\rangle &= |\Lambda_n\rangle + |\delta\Lambda_n\rangle \\ \text{where} \quad |\delta\Lambda_n\rangle &= \sum_{l=0}^{N} c_{nl}|\Lambda_l\rangle \end{aligned} \tag{2.28}$$

These definitions can be used to write

$$\begin{aligned} \boldsymbol{U}(a_1, a_2)|\Lambda_n'\rangle &= (\boldsymbol{U}_0(a_1, 0) + \delta\boldsymbol{U}_0(a_2))(|\Lambda_n\rangle + |\delta\Lambda_n\rangle) \\ &= (\Lambda_n + \delta\Lambda_n)(|\Lambda_n\rangle + |\delta\Lambda_n\rangle) \end{aligned} \tag{2.29}$$

When the pure second neighbor coupling terms are neglected it follows that

$$\boldsymbol{U}_0(a_1, 0)|\delta\Lambda_n\rangle = \Lambda_n|\delta\Lambda_n\rangle + \delta\Lambda_n|\Lambda_n\rangle \tag{2.30}$$

and when equation 2.28 is included

$$\sum_{l=0}^{N} c_{nl}\Lambda_l|\Lambda_l\rangle + \delta\boldsymbol{U}_0(a_2)|\Lambda_n\rangle = \Lambda_n \sum_{l=0}^{N} c_{nl}\Lambda_l|\Lambda_l\rangle + \delta\Lambda_n|\Lambda_n\rangle \tag{2.31}$$

the orthonormality condition $\langle\Lambda_n|\Lambda_l\rangle = \delta_{nl}$ leads to

$$c_{nm}\Lambda_m + \langle\Lambda_m|\delta\boldsymbol{U}_0(a_2)|\Lambda_n\rangle = c_{nm}\Lambda_n + \delta\Lambda_n\delta_{mn} \tag{2.32}$$

From here the shift in the eigenvalue $\delta\Lambda_n$ and eigenvector $|\delta\Lambda_n\rangle$ of the system can be determined when the two cases of $m = n$ or $m \neq n$ are studied.

$$\begin{aligned} &m = n \\ &\quad \delta\Lambda_n = \langle\Lambda_n|\delta\boldsymbol{U}_0(a_2)|\Lambda_n\rangle \end{aligned} \tag{2.33}$$

$$\begin{aligned} &m \neq n \\ &\quad c_{nm} = \frac{\langle\Lambda_m|\delta\boldsymbol{U}_0(a_2)|\Lambda_n\rangle}{\Lambda_n - \Lambda_m} \\ &c_{nn} = 0 \Rightarrow |\delta\Lambda_n\rangle = \sum_{l\neq n}^{N} \frac{\langle\Lambda_l|\delta\boldsymbol{U}_0(a_2)|\Lambda_n\rangle}{\Lambda_n - \Lambda_l} \end{aligned} \tag{2.34}$$

2.3.2 π-Mode

The operating mode of the 4-rod RFQ corresponds to the $\pi - mode$ of this model with $n = N$. In this case the eigenvector $\boldsymbol{J}_N$ of the unperturbed system $\boldsymbol{U}_0(a_1, 0)$ given in equation 2.22 becomes

$$\boldsymbol{J}_N = \frac{1}{\sqrt{N+1}} \begin{pmatrix} +1 \\ -1 \\ +1 \\ \vdots \\ (-1)^N \end{pmatrix} \tag{2.35}$$

The resonance frequency of the RFQ in this mode Ω_{0N} including the second neighbor coupling correction can be expressed by

$$\Omega_N = \frac{\omega_c}{\sqrt{\Lambda_N + \delta\Lambda_N}} \tag{2.36}$$

From equation 2.33 the correction of the eigenvalue is known

$$\delta\Lambda_n = \langle\Lambda_n|\delta\boldsymbol{U}_0(a_2)|\Lambda_n\rangle = (\boldsymbol{J}^{-1})_n \delta\boldsymbol{U}_0(a_2)\boldsymbol{J} \tag{2.37}$$

Now Λ_N and $\delta\Lambda_N$ can be put into equation 2.36 to give

$$\begin{aligned} \Lambda_N &= 1 + 2a_1 \\ \delta\Lambda_N &= -\frac{2a_2(N-1)}{N} \\ \Omega_N &= \frac{\omega_c}{\sqrt{(1+2a_1) - \frac{2a_2(N-1)}{N}}} \end{aligned} \tag{2.38}$$

The same discussion can be done about the shift in the eigenvectors $|\delta\Lambda_n\rangle$ due to the second neighbor coupling. From equation 2.34 it can be found that

$$\begin{aligned} |\delta\Lambda_n\rangle &= \sum_{l\neq n}^{N} \frac{\langle\Lambda_l|\delta\boldsymbol{U}_0(a_2)|\Lambda_n\rangle}{\Lambda_n - \Lambda_l} \\ &= \sum_{l\neq n}^{N} \frac{(\boldsymbol{J}^{-1})_l \delta\boldsymbol{U}_0(a_2)\boldsymbol{J}_n}{\Lambda_n - \Lambda_l} \boldsymbol{J}_l \end{aligned} \tag{2.39}$$

when $(\boldsymbol{J}^{-1})_l \delta \boldsymbol{U}_0(a_2) \boldsymbol{J}_n$ is proportional to a_2 and

$$\Lambda_N - \Lambda_l = \begin{cases} 2a_1(1 + \cos\frac{l\pi}{N} & for\ l \neq 0 \\ 4a1 & for\ l = 0 \end{cases} \tag{2.40}$$

and it can be shown that

$$|\delta\Lambda_N\rangle \propto \frac{a_2}{a_1} \equiv \mu \tag{2.41}$$

With this model the 4-rod RFQ is described in general. The current and voltage distributions can be calculated for an ideal model when all parameters are known. In chapter 5 the model is applied to tuning theory for the prediction of the influence of tuning plates on the longitudinal voltage distribution with the implementation of variations of the parameters in the real structure.

3 RFQ Projects

Based on the work on four recent RFQ projects, all the studies in this thesis were performed. Typically these projects are upgrades of injector lines or the construction of new accelerator complexes either for fundamental research institutes or applied facilities like for example for cancer therapy. An overview of the variety of RFQ projects in the last years is given in [43].

In this chapter the projects to which this thesis has contributed will be introduced. An overview of their basic parameters can be found in table 3.1.

3.1 ReA3 - Reaccelerator for Rare Isotopes at MSU

A new reaccelerator facility ReA3 has been constructed for National Superconducting Cyclotron Laboratory (NSCL) at Michigan State University (MSU) [18]. Experiments with reaccelerated beams are of high interest for example in astrophysics. Highly charged rare isotops can be produced with energies from 0.3 MeV/u up to 3 MeV/u for ions with Q/A=0.25 or 6 MeV/u for a Q/A of 0.5. The combination of a gas stopper, charge breeding and the reaccelerator provides a very high beam quality, compared to conventional electron stripping, with a broad energy range to be used for nuclear science experiments. A scheme of the ReA3 beamline is shown in Fig. 3.1. The ions from the gas stopper are transferred into an electron beam ion trap (EBIT) as the charge state breeder, are separated due to their charge to mass ratio and then reaccelerated in a line of a multi harmonic buncher (MHB), a room temperature RFQ and two superconducting quarter wave resonators from where they are distributed to the experiments. In a fist step the gas stopper will be filled with ions provided by NSCL's Coupled Cyclotron Facility (CCF) and later by the accelerator of the Facility for Rare Isotope Beams (FRIB).

As part of that project, a 3.5 m long 4-rod RFQ has been designed, developed and built working at 80.5 MHz. The 4-rod structure is shown in Fig. 3.2. This RFQ accelerates ions with a Q/A ratio of 0.2 up to 0.5 from an input energy of 12 keV/u to the final energy of 600 keV/u and it is special in various aspects. It

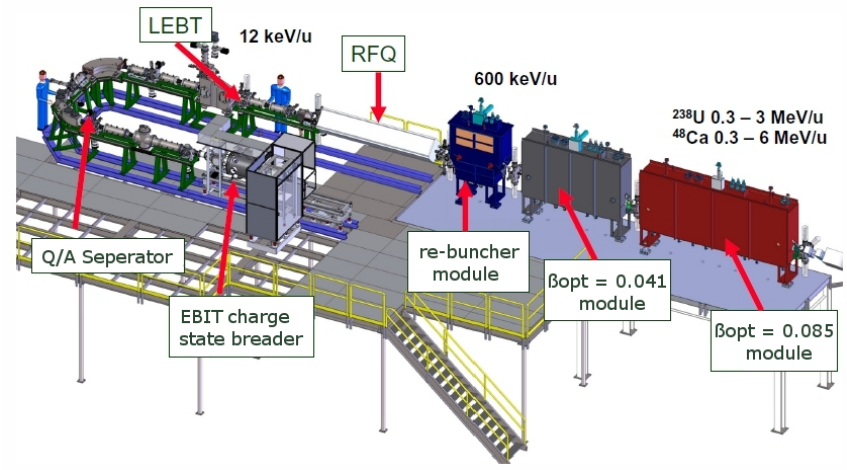

Figure 3.1: Scheme of the ReA3 accelerator. The reaccelerator with multi harmonic buncher, room temperature RFQ and two superconducting quarter wave resonators follows an EBIT charge breeder [52].

is designed to work up to cw-operation so there is an enhanced cooling system of all parts of the structure including electrodes and tuning plates. This is necessarily as a typical duty cycle for RFQ operation in in the order of 0.1%. It is one of the first 4-rod RFQs with a square cross section and with a vessel made of aluminum. Another project which used this kind of RFQ vessel is the Frankfurt Funneling Experiment [33]. To preserve a small longitudinal emittance and a relatively short RFQ, an external MHB was chosen to sit in front of the RFQ. Fig. 3.3 shows the results of the field tuning of the ReA3-RFQ which was done at IAP Frankfurt. The original voltage deviation of 6% was tuned to $\pm 1\%$.

After the RF set up, the RFQ was delivered in 2010 [52] and came into operation one year later [29]. In tests with helium and hydrogen the output energy of the RFQ has been confirmed and a transmission of 82% was measured which fits the design value. Now the RFQ is operated routinely with 20% duty cycle.

On this RFQ, a lot of data for the basic tuning studies were collected. Comparisons of different perturbations have been done and the tuning theory based on effect fuctions was tested. The results of this study are presented in section 5.2.

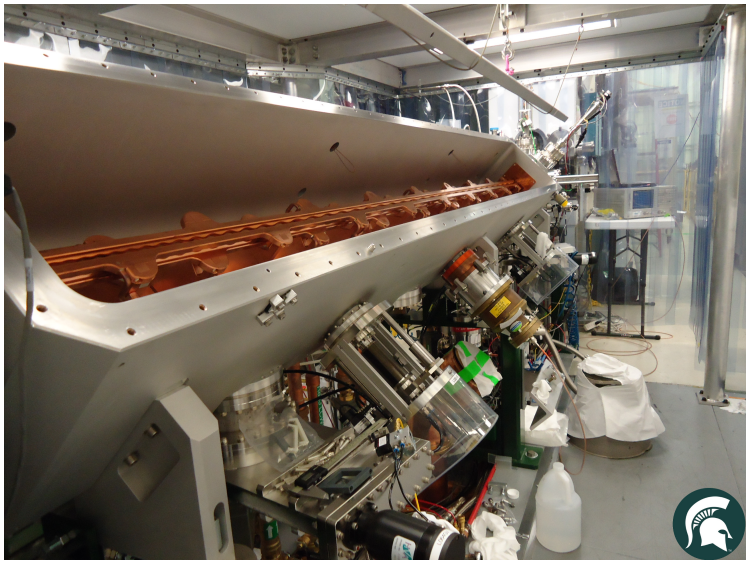

Figure 3.2: The ReA3 RFQ in the beam line at MSU [52]. A clean room has been installed due to the superconducting resonators following the RFQ.

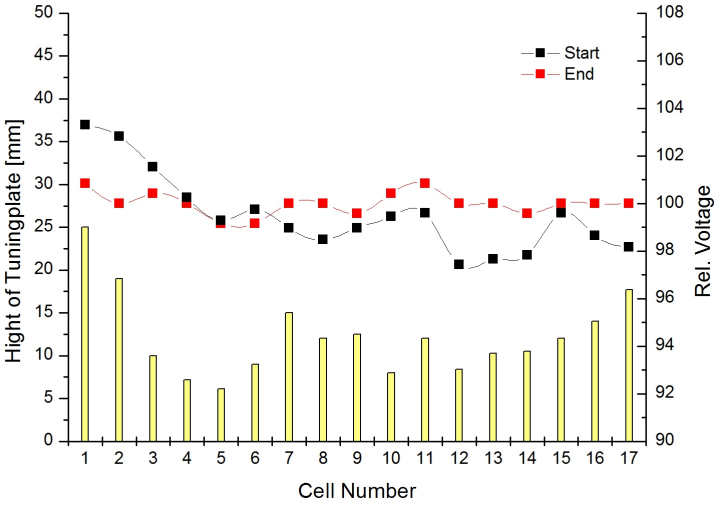

Figure 3.3: Results of the field flatness tuning of the ReA3 RFQ. The field has been tuned to have a maximum deviation of ±1% [48].

3.2 MedAustron - Cancer Therapy Center

The MedAustron RFQ is part of the accelerator for an ion beam cancer therapy center in Wiener Neustadt, Austria. For this kind of radiation therapy the characteristic energy deposition of ions in tissue which is described by the Bragg-Peak (as shown in Fig. 3.4 left) is taken advantage of. In contrast to photons, ions show a sharp peak in the energy deposition for a certain depth which depends on the energy of the ions. Positioning this peak in the overlap with the tumor enables the ions to kill tumor cells in a very defined region while the radiation of healthy tissue around the tumor is minimized. Typically this type of radiation therapy is chosen for patients with tumors in very sensitive organs like the brain, for example. It was significantly developed at GSI, Darmstadt and therapy centers like HIT, Heidelberg are already in operation. The MedAustron facility will treat patients using this method with protons and carbon. The test phase has started in 2013 and the first treatments are planed in 2015.

This 4-rod RFQ works at 216 MHz and accelerates ions from 8 to 400 keV/u with an electrode voltage of 70 kV [23]. Fig. 3.4 shows the therapy accelerator and a picture of the RFQ.

For this thesis, a full set of effect functions was measured on this RFQ in order to compare measurements to simulations. The measurements are discussed in section 4.2.

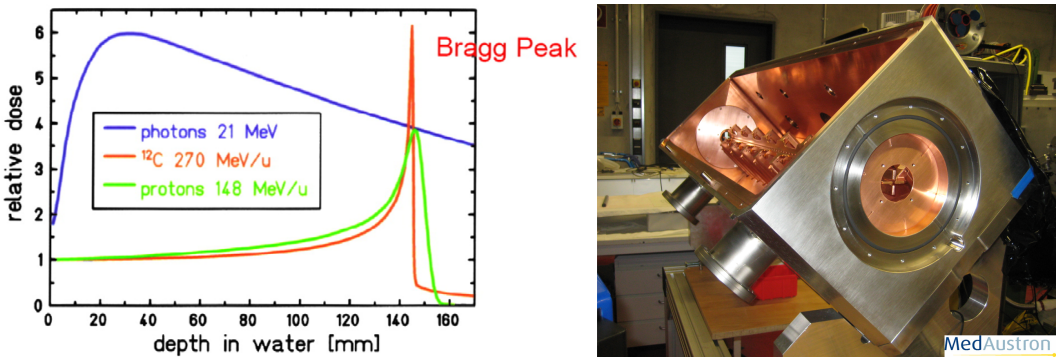

Figure 3.4: The MedAustron RFQ is part of a cancer treatment facility which radiated tumors with ions taking advantage of the Bragg peak in the energy deposition of ions in tissue [11].

3.3 H^- Injector for FNAL

The main project of this thesis was the 4-rod RFQ for the new injector at Fermilab (FNAL) that replaced the old Cockcroft-Walton Accelerator (C-W) which is shown in Fig. 3.5 left. The C-W has been in operation for 30 years and issues about its maintenance started to come up. So the modernization of the complex was meant to lead to a high reliability of the injector to serve the increasing demand for protons. As part of this project the 4-rod RFQ acceler-

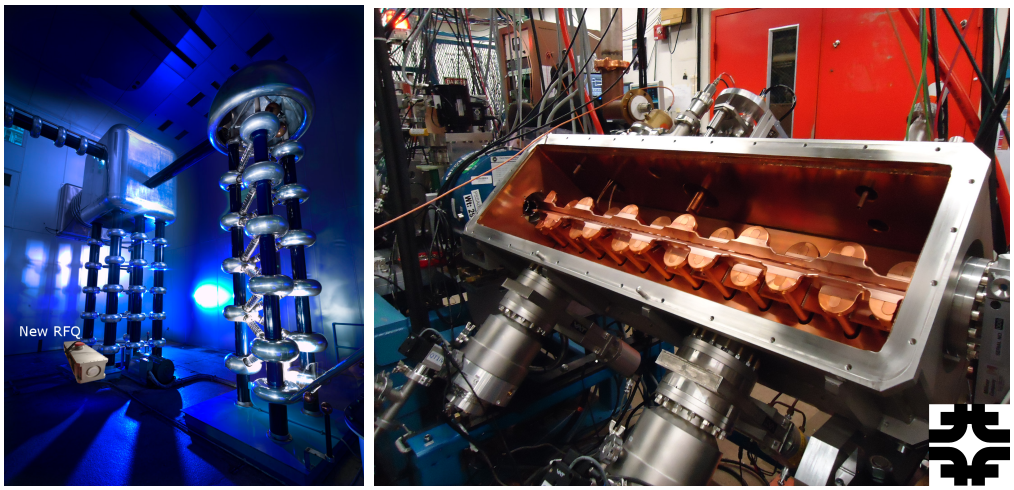

Figure 3.5: The Cockcroft-Walton (left [38]) is replaced by a 1.2 m long 4-rod RFQ (right) in the H^- injector upgrade at FNAL.

ates H^- ions from a 35 keV magnetron source to 750 keV, operating at 201.25 MHz with a duty factor of 0.1%. A very compact RFQ was designed with a length of only 1.3 m and an intervane voltage of 72 kV. Its Parmteq$_M$ simulations predict a transmission of 98% with a transverse output rms emittance of 0.37π mm mrad for x and 0.3π mm mrad for y. For this performance an input emittance of 0.37π mm mrad in x and y with an input energy of 35 keV is required. The particle dynamic design results are summarized in Fig. 3.6.

The results of the field tuning for this RFQ are shown in Fig. 3.7. The voltage distribution was improved from $\pm$10% to $\pm$3% with the shown tuning plate distribution and the use of additional tuning half cylinders. For more details of the setup values with all information about the RF installation see [47].

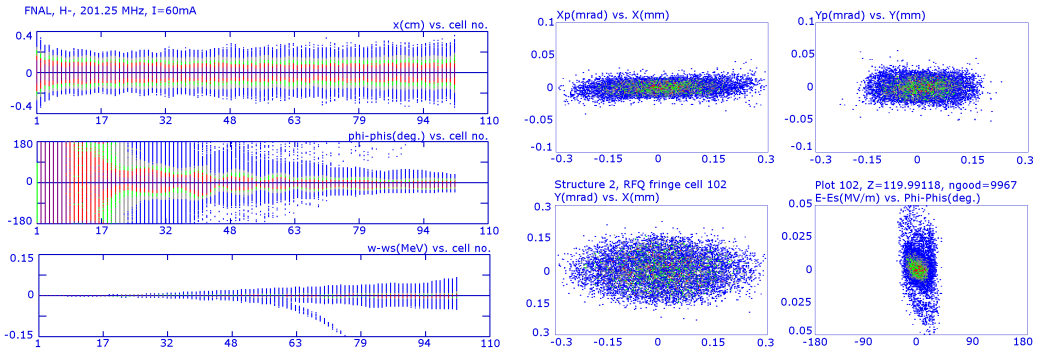

Figure 3.6: Results of the Parmteq particle dynamic simulations of the FNAL RFQ [50]. The design predicts a transmission of 98% with a transverse output rms emittance of 0.37π mm mrad for x and 0.35π mm mrad for y.

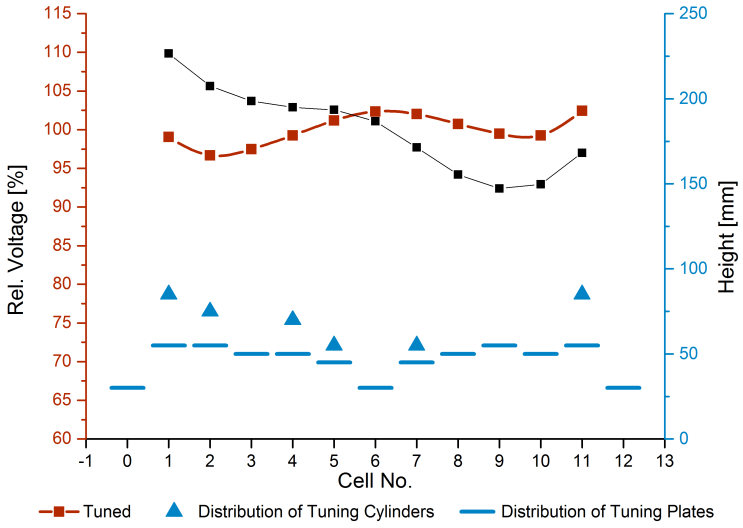

Figure 3.7: Tuning configuration of the FNAL RFQ after the RF set up at IAP, Frankfurt. A maximal deviation in the field flatness of ±3% with tuning plates and additional tuning half cylinders. [47].

Fig. 3.5 on the right shows the RFQ in the test stand at FNAL during the first beam test phase. The whole set up of the injector test stand at FNAL is pictured schematically in Fig. 3.8.

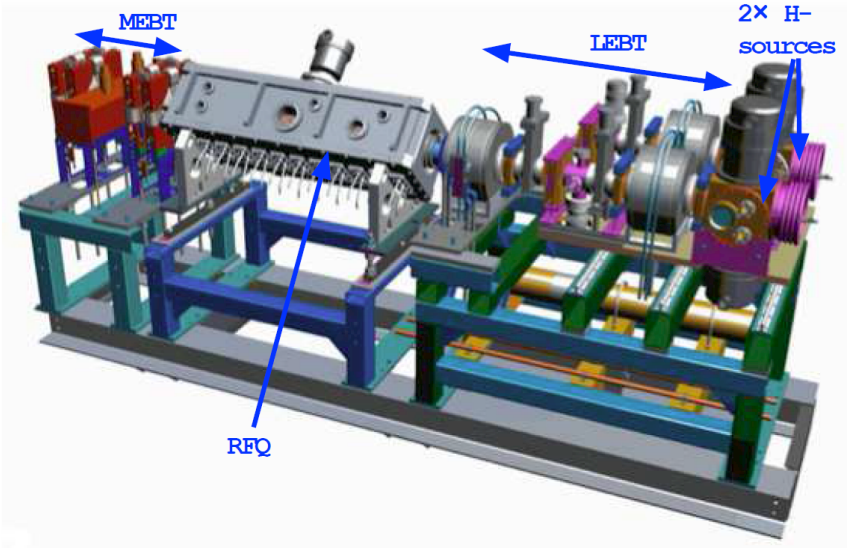

Figure 3.8: Test Stand of the H^- injector at FNAL including the magnetron source, LEBT, RFQ and MEBT [50].

Connected to the commissioning of this RFQ, the main studies on the boundary field of the 4-rod structure that are presented in chapter 6 have been done together with other accompanying studies [27][19]. In the first beam test, the output energy was measured to be more than 2.5% too low compared to the particle dynamic design. This has been found to be caused mainly by special irregularities in the boundary fields of this RFQ. Here, the advantage of the modular construction of the 4-rod RFQ was used. Following the studies that have been done, the RFQ structure has been modified. The aperture of the RF shielding at the low energy end has been opened and the RF shielding has been removed completely at the high energy end of the RFQ. In addition, new electrodes with a reduced capacitance had been installed so that the tuning could be reduced and an enhanced shunt impedance of 51.6 kΩm could be achieved. With these modifications, the nominal output energy of 750 keV could be confirmed and the power consumption of the RFQ could be reduced by about 23%. The details of the commissioning of this RFQ with an overview of the measurements and simulation studies can be found in [50]. Since December 2012 the RFQ has replaced the old Cockcroft-Walton. Fig. 3.9 shows

an oscilloscope picture of the beam pulse of 40 mA at the entrance of the DTL that follows the RFQ in the final configuration. For the whole MEBT and the RFQ, including every part between the source and the drift tube linac, a transmission of 67% is achieved recently.

Figure 3.9: 40 mA beam pulse from the RFQ in the first DTL at FNAL in December 2012.[50]

In parallel to the commissioning of the RFQ, the tuning theory based on the lumped circuit model of the 4-rod RFQ that is discussed in section 5.3 was completed at this time. The results of this collaboration with C. Y. Tan is published in [56].

3.4 LANSCE Proton Injector at LANL

The Los Alamos Neutron Science Center (LANSCE) provides protons and H^- ions for a variety of experimental programs with neutrons. In the current LINAC there are two Cockcroft-Walton (C-W) injectors, one for protons and one for H^-ions. The two beams can be injected into a shared Drift Tube Linac (DTL). In the long term it is planned to substitute the two C-Ws with a new front end which will consist of three separate RFQ lines. Each of them having a different pulse scheme depending on the experimental requirements. The proton injector will be operated un-chopped while the H^-ions are operated in a micro or long pulse mode. In the first stage of the upgrade, only the proton line will be replaced with a 4-rod RFQ and the C-W for H^-ions will stay in operation. The merging point of these two beam lines in front of the DTL is shown in Fig. 3.10.

For this project, design studies for the RFQ working at 201.25 MHz have been performed. The RFQ will be able to accelerate a beam of up to 60 mA from 35 keV to an output energy of 750 keV. It has been optimized in two major points: the RF design for an optimized field distribution and an advanced cooling system. The cooling system is necessary because of the high duty factor of 15% that is planned for its operation. This design has been proved and the RFQ is about to be built. Further details about this project are given in [13], [28], [12] or [41].

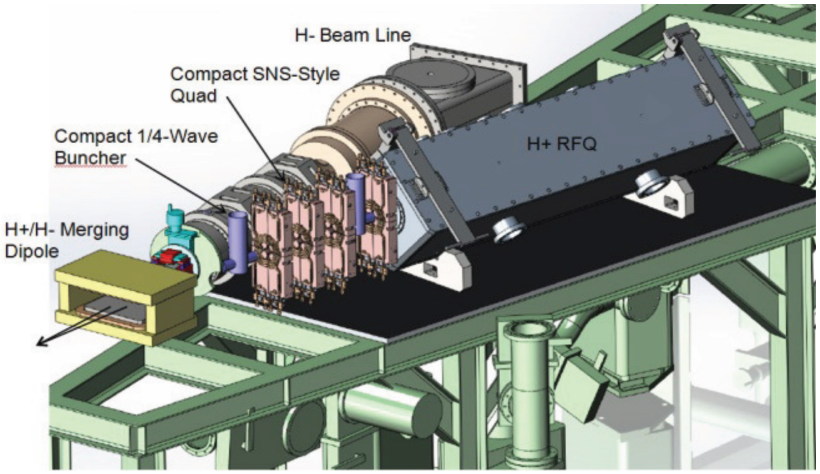

Figure 3.10: Merging point of the proton and H^--line in the LANSCE injector at LANL with the planned 4-rod RFQ.[13]

Table 3.1: Parameters of the 4-rod RFQs.

Parameter	Unit	ReA3 @ MSU	FNAL	LANL	Med-Austron
Design					
op. frequency	MHz	80.5	201.25	201.25	216.612
injection energy	keV/u	12 (β =0.005)	35	35	8
final energy	keV/u	600	753	750	400
Q/A		from 0.2 to 0.5			
A/Q		max. 5	1	1	
duty cycle		cw	max.1%	max.20%	
norm. acceptance	mm·mrad	0.6	0.3(rms)	0.2(norm.)	
modulation factor		1.15 to 2.6	1 to 2.1		2 (max)
intervane voltage	kV	86.2 (Q/A=0.2)	66.87	50	70
transmission	%	82 (MHB+RFQ)	98	96	
beam current	mA		50	60	4 (max)
Mechanics					
aperture (mid cell)	mm	7.3	4.17	3.8	2
tip radius electrode	mm	6	3.2	2.85	
rf cells		17	11	23	15
stem distance	mm	190	100	75/70	78
beam hight in tank	mm	200	130	150	155
electrode length	m	3.3	1.1817	1.75	1250
tank length	m	3.5	1.2		1233
tank diameter	mm	390 (inside)	300		
tuner diameter	mm	80			50
RF Meas.					
res. frequency	MHz	80.28 (no tuner)	201.06 (no tuner)		216.612
average Q_0		4238	2200		3600
total tuner range	kHz	300	ca. 700		500
flatness	%	$\leq \pm 1$	$\leq \pm 3$		± 1.7
shunt impedance	kΩm	200	63		74.05
coupling	dB	-35	-25		-27.4
Specials		External Buncher (MHB)		Var.Stem Distance	
in operation since		2011	2012	not yet	test phase 2013
transmission (meas.)	%	82 (MHB+RFQ)	67 (LEBT+RFQ)		98 (pencil beam)

4 Characterization of the Longitudinal Voltage Distribution

The transverse quadrupole field defines the focusing strength of the RFQ. This can be expressed by the focusing parameter B which is proportional to the ratio of the electrode voltage V to the square of the aperture a. It is defined by

$$B = \chi \frac{qe\lambda^2}{mc^2} \frac{V}{a^2} \tag{4.1}$$

where χ is a geometric parameter and λ the RF wavelength [1]. This is why the aperture is kept as small as possible with a voltage as high as possible to achieve an optimal focusing in the RFQ design. This is limited by electric breakdowns. There are two main designs of the longitudinal voltage distribution, the *field flatness*, of the RFQ: (a) a constant voltage along the electrodes and (b) a raising voltage in the acceleration part of the structure.

a) The design with a constant longitudinal voltage distribution, or a uniform power distribution, is the most common approach for RFQs. Especially all RFQs that have been studied for this thesis follow this design. It provides a smooth change of the beam characteristics in order to avoid emittance growth and to have a homogeneous particle distribution in the output beam. [42] [43]

b) The alternative design with a raised voltage towards the high energy end of the electrodes was presented in [2][3]. The idea of this concept is to enhance the accelerating component of the electric field which can be written as

$$E_z = kAV \sin(kz) \sin(\omega t + \phi) \tag{4.2}$$

The straight forward way to do this is to apply a higher voltage V on the electrodes. A limiting factor for this method is the peak electric field because of sparking in the RFQ. In order to prevent this, the bore radius r_0 needs to grow with the voltage so that the ratio V/r_0 is kept constant. But with this also the focusing strength is lowered and minor emittance

growth can occur. Another limit are thermal effects in the electrodes. With this design a higher acceleration gradient can be obtained compared to the constant voltage and there are actual projects like presented in [5] which use this method, too.

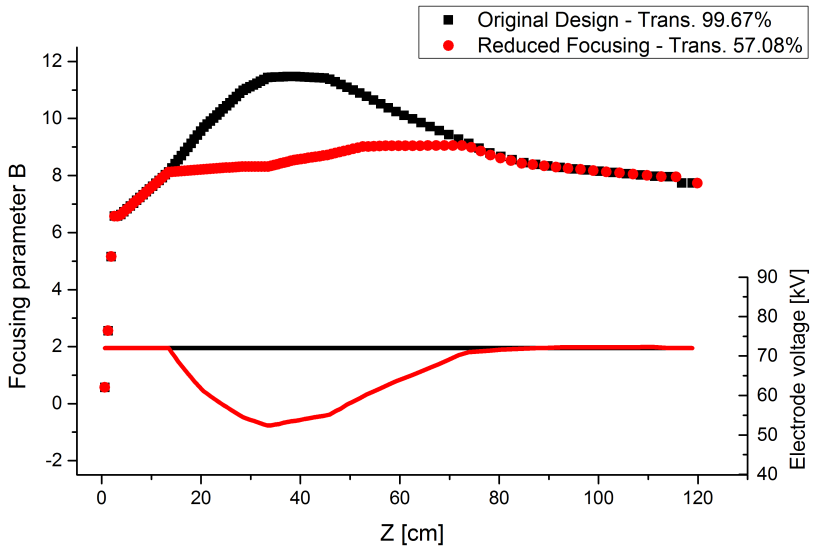

Figure 4.1: The longitudinal distribution of the focusing parameter B and the corresponding voltage V in the original design of the FNAL RFQ (black) and a modified design with locally reduced focusing in the bunching section of the RFQ (red).

Whatever design is chosen, for the performance of the RFQ it is important to match the measured flatness of the structure to the designed voltage profile from the particle dynamics. Otherwise there is a difference in the focusing strength profile of the RFQ. Fig. 4.1 shows a comparison of the original FNAL-RFQ design and a modification of it where the tip of the focusing parameter B is canceled out by changing the values manually in the Parmteq$_M$ input file which corresponds to a lower voltage in the middle of the RFQ as $B \propto V$. The modification leads to a drop in the simulated transmission of the RFQ from 99.67% to 57.08%. Comparable studies with a reduced focusing at both ends of the RFQ had a much smaller effect on the transmission of a few percent. Such defects in the focusing strength can be balanced by applying a higher total voltage on the electrodes as shown in [50], but again that leads to a higher power consumption of the RFQ and is limited by the maximum output of the power supply.

4.1 Influences of RF Design Elements on the Field Flatness

The influence of tuning methods and RF design elements of 4-rod RFQs on the voltage distribution have been studied. Every change in the field geometry or the voltage distribution could, for example, lead to particle losses or a increased surface current with thermal effects on single parts of the RFQ. That is why further research has to be done about the behavior of the 4-rod RFQ. The results of this analysis which is concentrated on simulations using CST MicrowaveStudio to evaluate the effects of the overlap of electrodes, spacing of the stems, RF shielding insert, the modulation and additional tuning elements on the fields in the RFQ are presented in this section.

4.1.1 Overlap of Electrodes

The overlap of the electrodes is the dominating factor for the non-constant voltage along the RFQ. It is the part on both ends of the electrodes reaching out of the last stem as marked in Fig. 4.2. The idea of it is to improve the field symmetry at the end of the 4-rod structure [10]. Due to the additional capacitance of the electrodes which influences the boundary RF cells, their frequency is lowered compared to the middle cells of the RFQ. This leads to a higher voltage in the end RF cells, what is reflected in the typical tub like shape of the field flatness. In section 5.3.1 is is shown that, in the lumped circuit model of the 4-rod resonator, this effect is described by the strength of the second neighbor coupling between the RF cells. The model shows that only with this coupling the forming of the tub shape occurs.

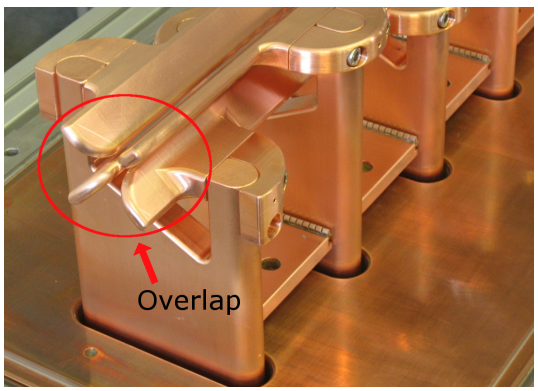

Figure 4.2: The overlap is the part of the electrodes reaching out of the last stem.[14]

Fig. 4.3 shows the changes in the field flatness caused by a growing overlap in an RFQ model which is a high frequency RFQ at about 200 MHz with a length of 1.2 m. The structures shows the building of the typical tub form with a maximal difference of 10% between the highest and the lowest voltage. Comparative studies with a 3 m long 80 MHz RFQ show that the structure reacts less sensitively to changes of the overlap. For this long 4-rod RFQ, the geometric influence of the overlap is much smaller because its size is negligible compared to the length of the electrodes and small compared to one RF cell. So the frequency shift of the outer RF cell compared to the inner ones is small.

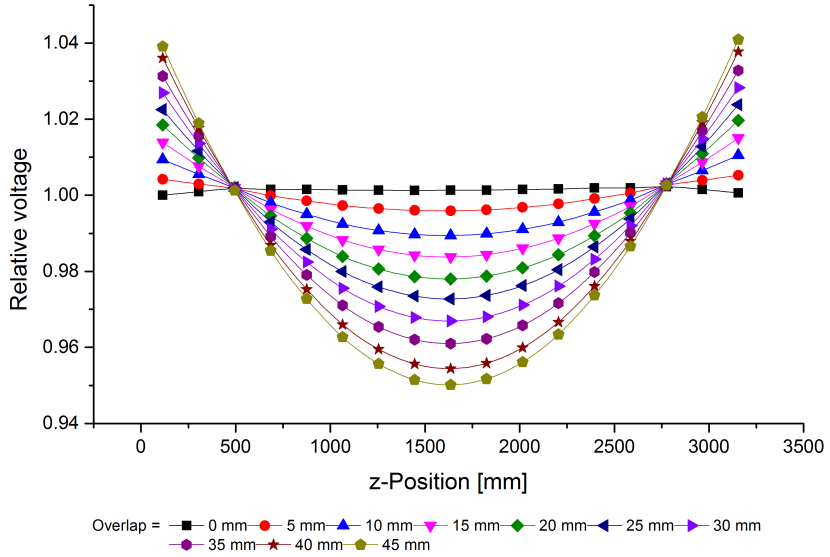

Figure 4.3: Field flatness with variation of the electrode's overlap from 0 mm to 45 mm. Without an overlap the field flatness is constant while with its growth the typical tub form appears. [49]

4.1.2 Spacing of the Stems

The second parameter that defines the resonant frequency is the inductance of the RF cell. It is defined by the current path over the stems, the tuning plates and the electrodes. Concentrating on that influence on the field flatness, the distance of the stems (SA) was swept from a value of SA =100 mm down to half of the width with a constant overlap, meaning a resonance shift of nearly 110 MHz from 150 MHz to 258 MHz. Taking the SA = 50 mm stem width as a reference of 100% voltage, it is especially clear that the low frequency

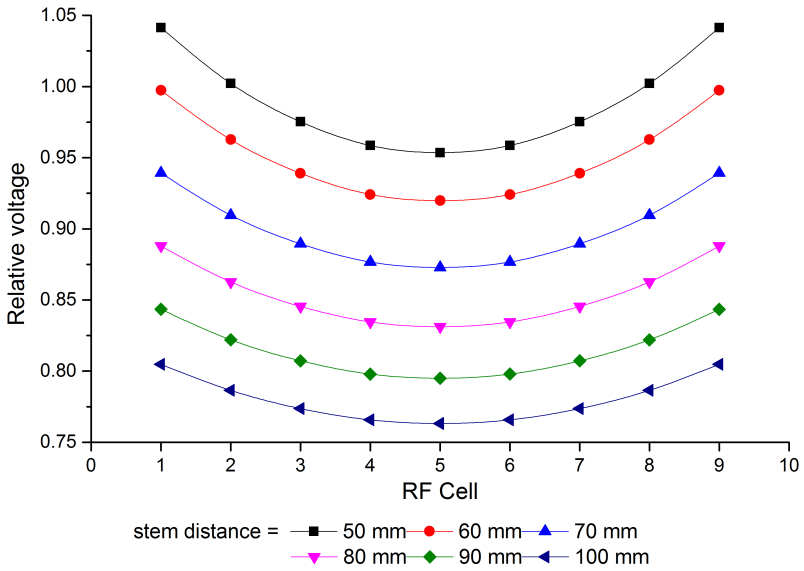

Figure 4.4: Field flatness with variation of stem distance SA [49]. SA is changed from 100 mm to 50 mm covering a frequency shift of about 100 MHz.

structure reacts less sensitive, as the deviation in field flatness is much smaller while its magnitude is reduced, like shown in Fig. 4.4.

In the following study, the stem to stem distance has been varied. Equally positioned stems have mechanical advantages in fabrication, so the stem distance was varied block wise with two different values along the structure instead of a gradual increase. The original design is a 4-rod RFQ for 200 MHz with a length of 1.75 m, a stem distance of SA =73 mm and an overlap (OVL) of 25.5 mm at both ends of the electrodes. Starting with this set up, different positions of the stems have been studied where the inner RF cells were kept constant at SA = 75 mm and one, two or three stems at both ends of the RFQ were moved closer into the RFQ by changing the parameter SV. With these variations, the field flatness was studied. A similar study of an RFQ with a reduced SA in the last RF cells can be found in [40].

As was discussed before, the overlap dominates the formation of an non-constant field flatness, but has other advantages in case of field symmetries at the end of the RFQ. The idea that was followed in this simulations was to distribute the stems equally so that there is nearly no overlap (1 stem, SV =0) and then move the outer stems into the structure to form an artificial overlap again. The results of this simulations are shown in Fig. 4.5. By the reduction of SA in the outer cells, the extra capacitance due to the overlap

can be compensated and even overcompensated. In the original design (black) there is a difference between the maximum and minimum voltage of 26.9% with the typical tub like shape. With a growing shift of the outer stems this shape can be flattened and can even switch around when the capacitance is over compensated (violet). In this case the profile is changed to a hill like shape with minima at the outer RF cells and a maximum in the middle of the RFQ. A minimal difference between maximum and minimum voltage of 4.1% could be achieved in this simulations. This study shows the possibility that by a fitting spacing profile of the stems, every desired field flatness could be produced. The requirement for an RF design on an 4-rod RFQ that includes these optimization is that the possibility for an exact simulation of the field flatness needs to be at hand.

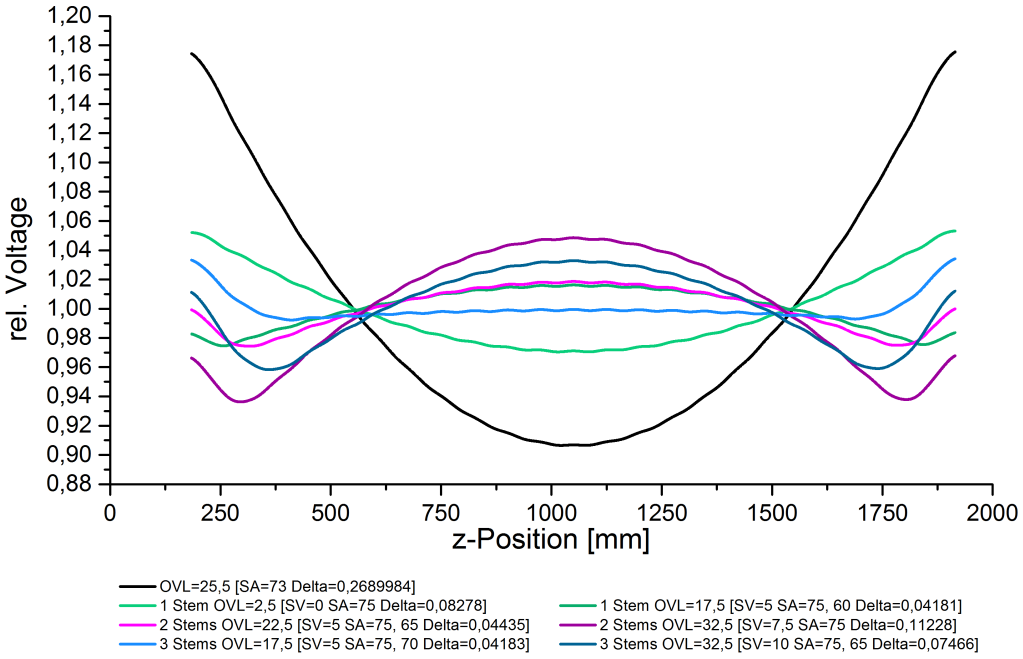

Figure 4.5: The field flatness with shifts of the stem positions [51]. The stems have been positioned on the electrodes equally without an overlap. Then one, two or three stems have been shifted into the RFQ so that shorter RF cells were created at the ends of the RFQ.

4.1.3 RF Shielding Insert

Another component, which is interesting because of its influence on the voltage of the electrodes with respect to the tank wall, are inserts at the RFQs entrance and exit. Their effect on the beam can be compared with a drift tube, which has been analyzed with varying diameters of the drift tube are shown in Fig. 4.6. The drift tube is connected to an insert in the end wall of the RFQ at its high energy end. It causes a reduction of the electrode ends voltage compared to the open boundaries on the low energy end, so that it has a positive a effect on the field flatness. This effect is similar for different diameters of the drift tube, because all curves lie close to each other.

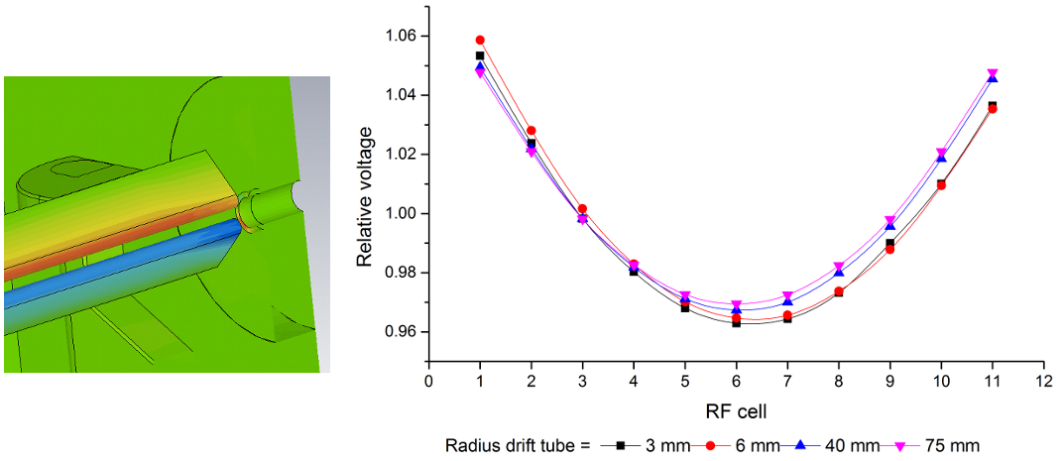

Figure 4.6: An insert with an aperture similar to a drift tube (left) shielding RF leaking out of the RFQ and its influence on the field flatness at the high energy end of an RFQ (right) [49].

4.1.4 Modulation

In most 4-rod RFQs the only parameter that is changing along the electrodes that distinguishes one RF cell from the others is the modulation profile of the vanes. In the low energy section of the RFQ the modulation factor m is close to one, so that there is only a small sinusoidal profile visible on the vanes. Moving on to the high energy end and the acceleration part, that profile becomes more significant. Here m grows so that the accelerating component of the electric field gets higher.

Looking at the untuned field flatness, the simulation results of electrodes without modulation are presented in Fig. 4.7 compared with the correspond-

ing measurements. The simulation without modulation reflects the degree of the deviation from a constant voltage, but does not include the capacitance distribution along the electrodes due to the changing modulation profile. The measured curve shows a different behavior with a shift symmetry point in the voltage distribution towards the high energy end of the RFQ, where the electrode voltage is a bit lower compared to the low energy end.

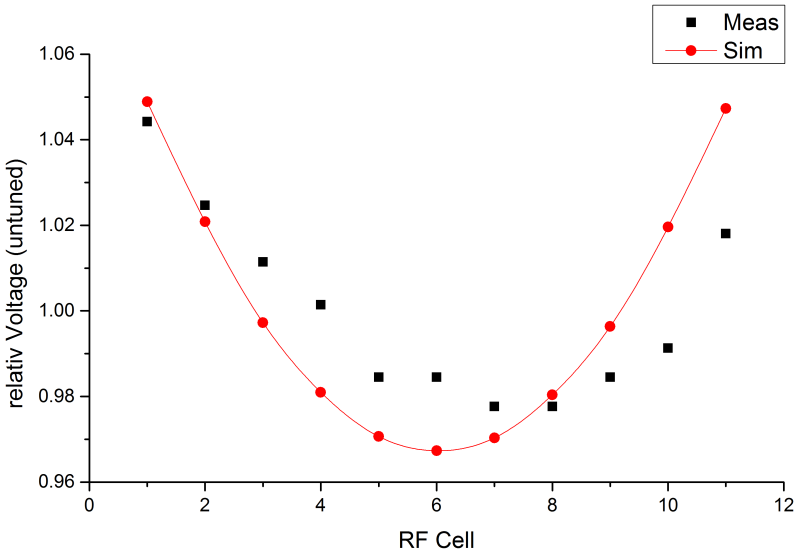

Figure 4.7: Simulation with unmodulated electrodes (red) compared with a corresponding measurement of an untuned modulated RFQ [49]. The minimum of the measured field flatness is shifted towards the high energy end compared to the unmodulated simulation model.

4.1.5 Tuning Plates

To manipulate the deviations from cell to cell in the longitudinal voltage distribution of the electrodes, tuning plates are used between the stems to change to current path of the RF cell. An example is pictured in Fig. 4.8.

These so called tuning plates shorten the current path in an RF cell, so that the inductance of this cell is changed. In principal they do nothing else than to detune the oscillator similar to what happens in a trombone. The detuning follows the Thomson formula

$$f_0 = \frac{1}{\sqrt{L \cdot C}} \rightarrow f_0' = \frac{1}{\sqrt{(L + \Delta L) \cdot C}} \tag{4.3}$$

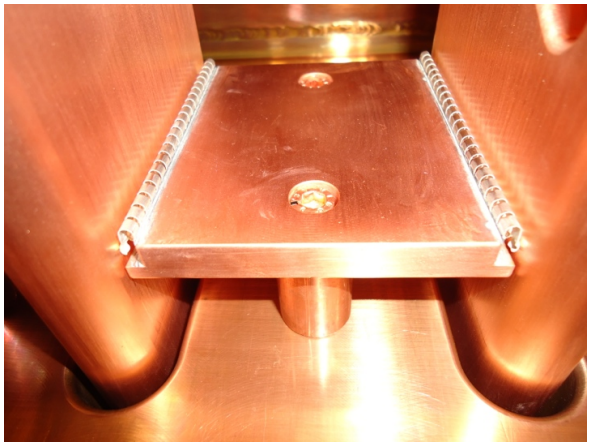

Figure 4.8: Tuning plates shorten the current path between the stems in 4-rod RFQs. They are used to tune the field flatness by changing the RF cell's inductance.

When the resonance of that cell is changed, what results in a lowering of the voltage in that and the neighboring cells. This effect is plotted in Fig. 4.9 where a simulation of the untuned field flatness which means the longitudinal voltage distribution without any tuning plates (blue) is shown together with the field flatness when the tuning plate in cell three is set to a height of 30 mm (red). In the comparison, the tilting of the field flatness that is induced by the tuning plate is visible. While the voltage drops around cell three it raises at the other end of the RFQ. This effect with its dependence on the tuning plates height, position in the RFQ and on the whole length of the RFQ are discussed in this section.

Effect Functions

For the quantification of the effect of the tuning plates so called "effect functions" EC have been introduced in [10]. These are basically the ratio of the tuned field flatness U_T to the untuned field flatness U_U.

$$EC = \frac{U_T}{U_U} \tag{4.4}$$

Looking at this function it is clear that $EC = 1$ corresponds to no change in the voltage, $0 \leq EC < 1$ means a decrease and $EC > 1$ to an increase of the tuned voltage compared to the untuned one. The effect of a tuning plate is dependent on three parameters.

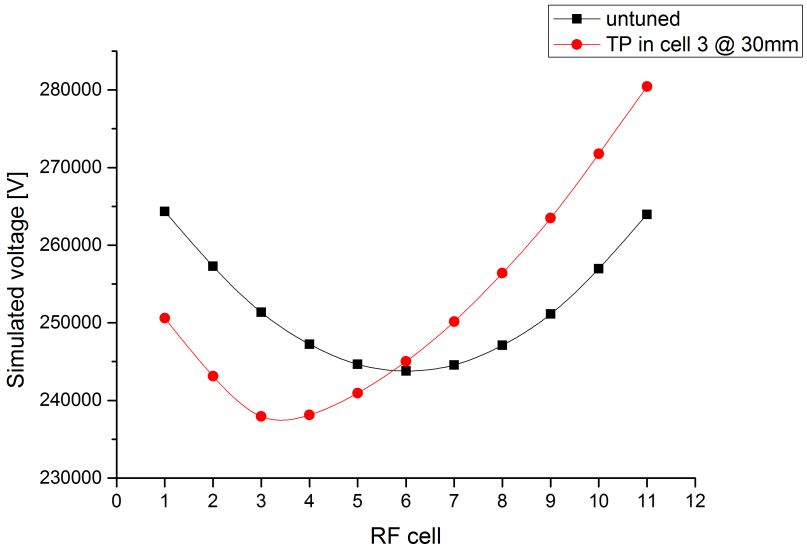

Figure 4.9: Simulation of field flatness without and tuning (black) and one tuning plate in RF cell 3 (red) [46]. The voltage in the RF cell of the tuning plate is lowered while it is raised in RF cells that are more distant.

1. k - which tuning plate is moved, respectively which RF cell is tuned
2. z - the longitudinal position of the voltage value
3. h_k - the height of the tuning plate in RF cell k

The most obvious of these parameters is the height of tuning plate h_k as this is the parameter which defines the current path in the RF cell. Fig. 4.10 shows $EC_{k=3}(z)$ for three different h_k of 0 mm, 31 mm and 55 mm. For $h_k = 0$, EC is one as was discussed above, but for a growing h_k effect of the tuning plate gets stronger.

This dependence is studied further in Fig. 4.11 where $EC_{k,z=k}(h_k)$ is plotted for all possible ks of a 11-cell RFQ. In this case the change in the simulated voltage is observed at the longitudinal position z in the RFQ where the tuning plate is moved at $z = k$. So what can be extracted from this graph is that the maximum effect of a tuning plate is strongly dependent on the position where it is located. The tuning plates in the middle of a 4-rod RFQ have only a small effect on the voltage compared to the ones in the outer RF cells. The different influence of the RF cells can be explained by the capacitance distribution.

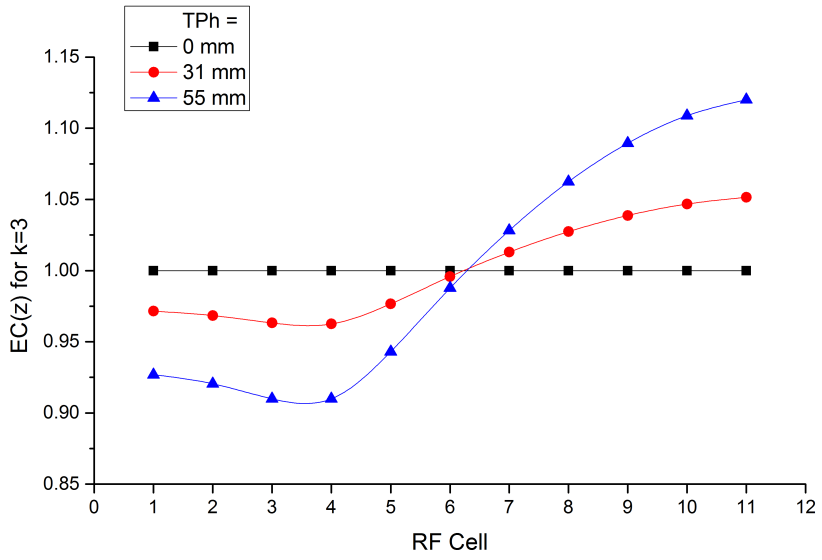

Figure 4.10: The effect of a tuning plate EC with the height of the plate. The higher the tuning plate the stronger is the suppression of the RF cell's voltage. [46]

As it was described in chapter 2.3 the end RF cells carry a higher capacitance than the rest of the cells. Because of second neighbor coupling these cells are coupled with the outer RF cells what leads to a higher sensitivity to their tuning plate's position.

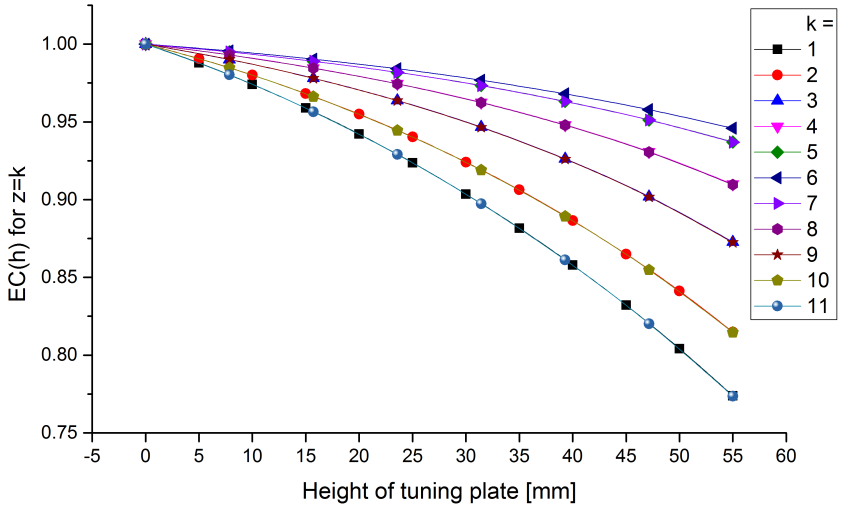

Figure 4.11: $EC(h)$ plottet at the position of the tuning plate ($z = k$) [46]. Each tuning plate in RF cell k is raised separately. The boundary cells have a stronger effect than the inner cells.

In comparison to $EC_{z=k}(h_k)$ in Fig. 4.12 $EC_{k=4,z}(h_k)$ is shown where only the tuning plate in RF cell four $k = 4$ is moved and the voltage is observed in different RF cells at $z = 1$, 4, 7 and 11. Here the tilt effect of one tuning plate is visible: the voltage drops in the cells closest to the tuning plate while it increases on the other side of the RFQ.

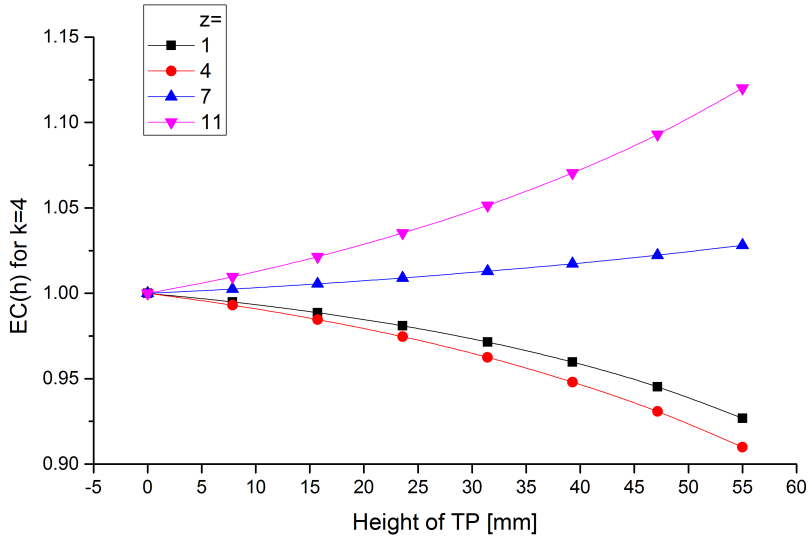

Figure 4.12: *EC* is observed at different positions z in the RFQ when tuning plate $k = 4$ is raised [46]. *EC* shows a contrary gradient depending on the position where the voltage is observed.

4.1.6 Additional Tuning Elements

Piston Tuner

There are several tuning methods used in the RFQ aside of tuning plates. The most common ones are piston tuners, which are used to tune the resonance frequency during operation. Effects like vacuum pumping, heating, beam loading or others are compensated that way. These tuners are moved into the resonant structure where they are placed middle of an RF cell between the stems. The maximum position in the 4-rod RFQ is pictured in Fig. 4.13 where the tuner is inserted from the left side into the area of the stems.

The piston tuner suppresses the magnetic field between the stems so that the inductance of the RF cell is changed and an increase of the resonant frequency in the order of hundreds of kHz is observed. Fig. 4.14 shows the frequency

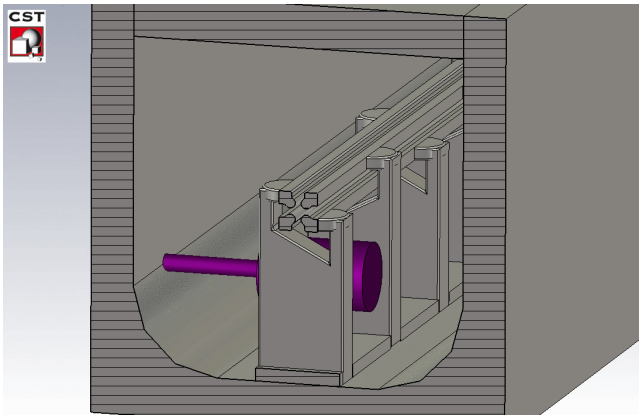

Figure 4.13: Piston tuner in the 4-rod RFQ. The tuner (violet) in an RF cell suppresses the magnetic field for dynamic tuning of the RFQs resonant frequency in operation.

shift when two tuners are moved into a 100 MHz-RFQ simultaneously for three different piston diameters. The beam axis is at 0 mm in this case, at 100 mm the tuners are completely out of the resonator and at -45 mm the edge of the piston is at the same position as the opposite edge of the stem (as shown in Fig. 4.13). The highest change in the frequency relating to a certain step in the position of the tuner occurs when the piston enters the space between the stems until it reaches the beam axis depth. From this point on, saturation starts. As soon as the piston leaves the space between the stems, the tuning effect vanishes, because the overlap with the magnetic fields gets smaller again. There is also a strong correlation with the maximum frequency shift that can be obtained with the diameter of the piston, because a higher ratio of the magnetic field can be suppressed with a bigger piston.

The piston is a resonator itself, so in the design, it is important to check its eigenmodes in comparison to the operation frequency of the RFQ in a separate model and when the tuner is inserted into the RFQ. Inducing a resonance in the tuner by either the operating frequency or a higher harmonic, can lead to heating and in worst case, to melting of components of the tuner. This effect was observed for example in the high power RFQ for SARAF [10]. A resonance simulation of a piston tuner that has an inner diameter of 76 mm is shown in Fig. 4.15. Its first mode occurs at 693 MHz, which is high compared to the typical 4-rod operating frequencies of about 80–300 MHz. But for greater piston diameters, the modes of the tuner and the RFQ can be much closer.

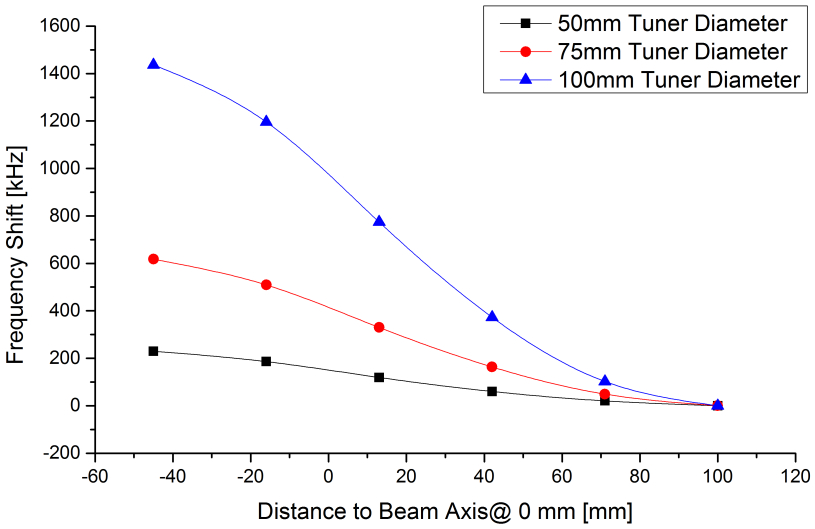

Figure 4.14: Resonance Shift with Piston Tuner. The increase of the resonance frequency depends on the size of the piston.

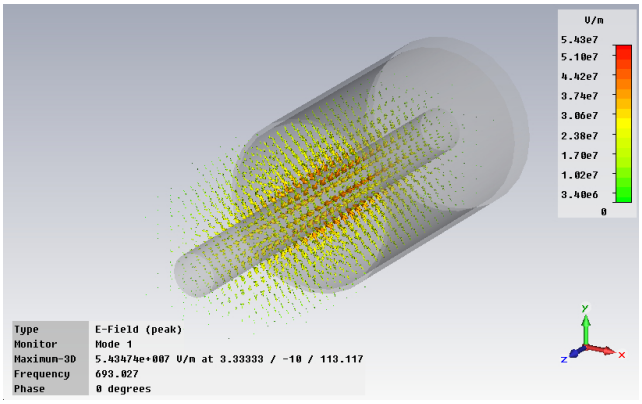

Figure 4.15: The piston tuner is a resonator itself [49]. If a resonance is exited by the operating frequency or higher harmonics, the tuner can heat up or perturb the resonance of the RFQ itself.

Depending on the length of the structure, there are typically one or two piston tuners in use. This number is pointed out especially in the comparison to 4-vane RFQs which need to have typically in the order of 30 static and dynamic pistons for a similar structure. In Fig. 4.16, the offset of the field flatness on the upper and lower electrodes with one tuner in the middle of the RFQ is illustrated. Because of the tuners geometric position between the stems, the effect on the voltage of the lower electrodes is slightly higher than on the upper pair. It is important to mention that the insertion of the tuner can

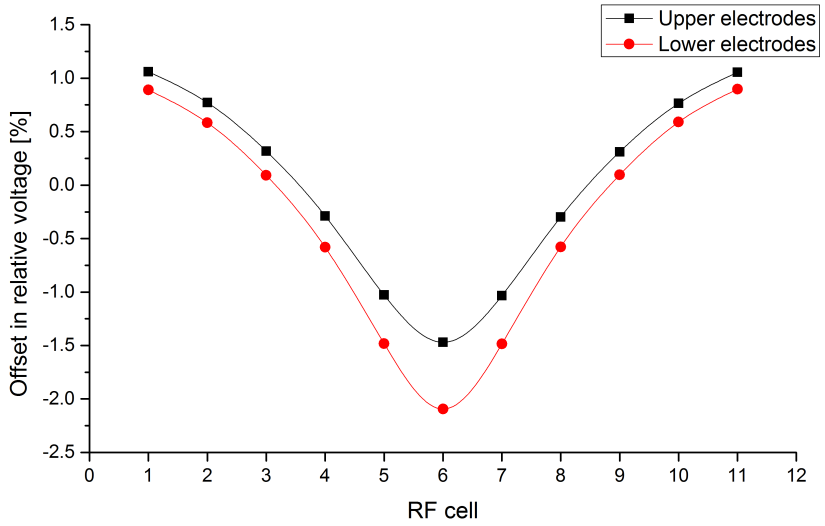

Figure 4.16: Influence of the Piston Tuner on the Field Flatness of Upper and Lower Electrodes. Because of its position in the RF cell the tuner has a stronger influence on the lower electrodes than on the upper ones. [49]

effect the electrodes' voltage in both ways: either increasing or decreasing it. The reaction of the RFQ structure to the suppression of the magnetic field in an RF cell depends on the individual characteristic. In one case the capacitive in the other case the inductive influence of the tuner seems to be dominating.

Half Cylinders

In some special cases, half cylinders like they are pictured for example in Fig 4.17 are used in combination with tuning plates. They offer the possibility for expanding the regular tuning range of the tuning plates so that greater flexibility can be gained. This can be helpful, for example, if there are other elements limiting the tuning plate height, like the coupling loop. The half cylinders are screwed onto a tuning plate and can have different sizes depending on the desired tuning effect. The way they influence the field is the perturbation of the magnetic field between the stems, similar to the piston tuner.

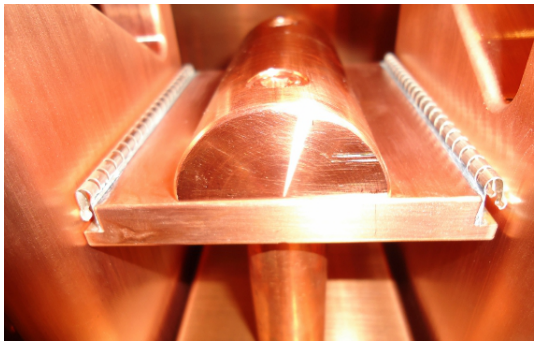

Figure 4.17: Tuning Half Cylinders. In addition to tuning plates half cylinders can be used for tuning the field flatness [47].

4.2 Measurement of the Longitudinal Voltage Distribution

All the graphs that have been presented up to now are results from MWS simulations. But when an RFQ is built, the field flatness has to be matched to the one used in the particle dynamic design, so it has to be measured. This is done by a perturbation measurement of the resonant structure. In a cavity resonator with homogeneous fields the measurement is done with a small bead while in the 4-rod RFQ an additional capacitance ΔC that is put onto the electrodes is used. The total energy that is stored in the resonator W with the electrode voltage amplitude U and the total capacitance C is

$$W = \frac{1}{2} C U^2 \tag{4.5}$$

Adding a small perturbation capacitance ΔC changes the field locally so that the new energy W' with the perturbed voltage amplitude U_S can be written as

$$W' = \frac{1}{2}(C + \Delta C) U_s^2 \tag{4.6}$$

The perturbation here is just a capacitive one so that the magnetic field is not changed in this case. The perturbation is chosen to be small so that $\Delta C \ll C$ and thus the approximation $U \approx U_s$ can be followed. In the measurement, only the effective values can be measured so $U \to {}^{U}/\sqrt{2}$. When these steps are included, the change in the resonator energy can be defined by

$$\Delta W = \frac{1}{4} \Delta C U^2 \tag{4.7}$$

Using the Slater Theorem [54] for an energy change, the frequency shift Δf compared to the unperturbed resonance frequency f_0 can by written as

$$\frac{\Delta f}{f_0} = \frac{\Delta W}{W} = \frac{\frac{1}{4}\Delta C U^2}{W} \tag{4.8}$$

At this point two other resonator parameters need to be introduced namely the quality factor Q and the shunt impedance R_P.
The quality factor describes the oscillation capability of a resonator. It connects the stored energy W with the dissipated power in an oscillation period $\bar{N}$ by

$$Q = 2\pi f_0 \frac{W}{\bar{N}} \tag{4.9}$$

The shunt impedance helps to define the power that is needed to obtain the electrode voltage. Similar to Q it shows the capability of an accelerator to transfer the driving power to the field. It is defined as

$$R_P = \frac{U^2}{\bar{N}} \tag{4.10}$$

Putting all this together results in

$$U^2 = R_P \bar{N} = \frac{2Q_0}{\pi f_0^2} \frac{\Delta f}{\Delta C} \cdot \bar{N} \tag{4.11}$$

For an absolute measurement of the electrode voltage, a well defined perturbation capacitance is needed. But for the measurement of the longitudinal voltage distribution this is not necessary because only the relative voltage is considered. In this case equation 4.11 can be simplified to

$$U \propto \sqrt{\Delta f} \tag{4.12}$$

In order to measure a longitudinal voltage distribution, the frequency shift from the perturbation is measured for each RF cell. Examples of perturbation devices are pictured in Fig. 4.18. Different ones can be used, that range from simple capacitors or ceramic blocks to perturbations with tight contacts and because of that better defined connection to electrodes and, of course also calibrated ones.

Figure 4.18: Different kind of perturbation capacitors and a ceramic perturbation for the measurement of the field flatness.

The choice of the perturbation capacitor is important as it can affect the results of the field flatness measurement. This is shown in Fig. 4.19 where one RFQ is measured with different capacitors in comparison. It is important to design a fitting perturbation capacitor for each RFQ so that changes in the contact to the electrodes during a measurement cycle can be neglected.

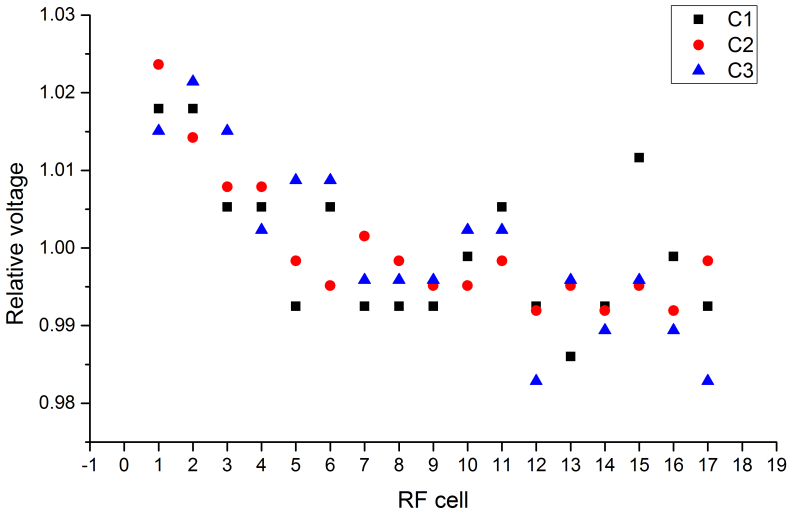

Figure 4.19: The results from the field flatness measurement with three different perturbation capacitors C1, C2 and C3. The choise of the perturbation capacitor influences the results especially in the boundary RF cells.

4.3 Results of Field Flatness Measurements

The following Fig. 4.20 shows in principal the measurement of the same data that is simulated in Fig. 4.9 but for all possible tuning plates TP_k with $k = 1...15$ of a 15-cell RFQ. For each curve$_k$ one tuning plate in cell k is shifted to 40 mm and the field flatness on the length of the RFQ is plotted. The difference in the effect of each cell that was mentioned before is also visible in this measurement. The outer RF cells have a greater influence on the field flatness than the middle cells. In addition an asymmetry between the low and high energy end of the RFQ occurs in these measurements. This is typical as the high energy part of the electrodes carries a higher capacitance than the low energy part due to the changing modulation along the electrodes. This causes a small shift of the symmetry point towards the low energy end.

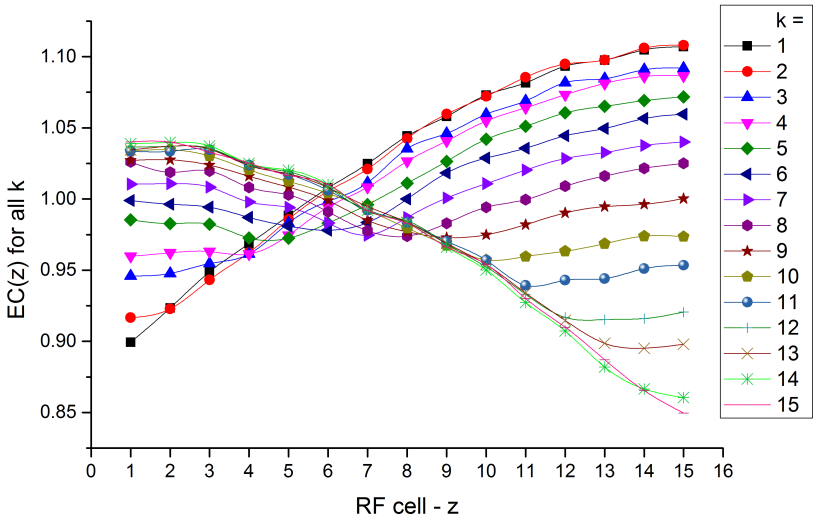

Figure 4.20: A full set of measured effect curves $EC(z)$ for all tuning plates in RF cell k for a 200 MHz RFQ. The symmetry point is shifted towards the low energy end of the RF.

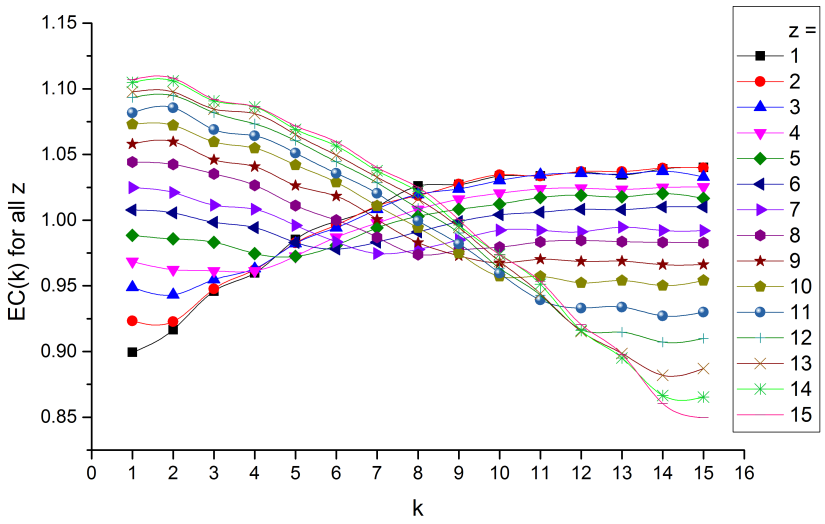

Figure 4.21: Measurement of effect curves in the dependence $EC(k)$ for all positions z in the RF cells showing the change of the voltage at one z-position when one after the other tuning plate in RF cell k is raised.

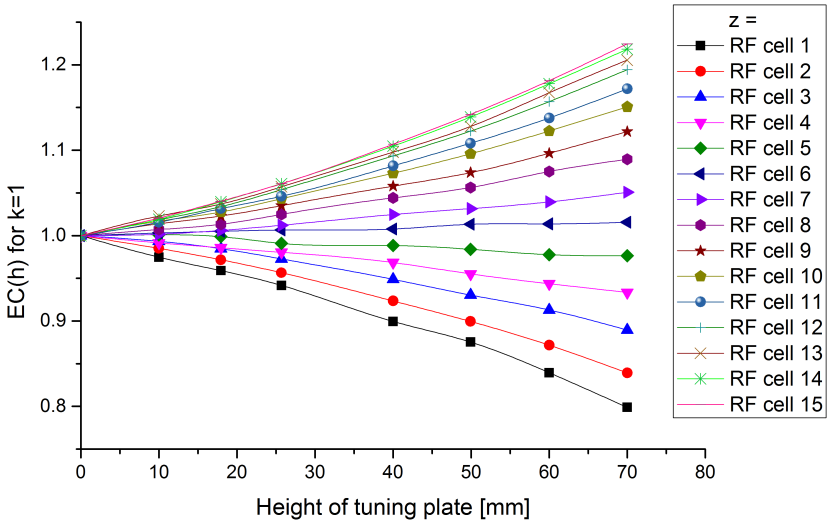

Figure 4.22: The full measurement set of the height dependence of effect functions $EC(h)$ for the example of the first tuning plate $k = 1$ for all z.

A similar picture is generated in Fig. 4.21 instead, when for each curve$_z$ here, it is referring to EC of one RF cell is plotted over the number of the RF cell in which the tuning plate is moved to 40 mm. So one curve shows the dependence of one RF cell's voltage on each tuning plate.

For a full set of measurements the height dependence is still missing in these pictures. Fig. 4.22 shows this set of measurements for only one, the first, RF cell as an example. Each curve$_z$ presents the dependence of EC in the RF cell z on the height of the first tuning plate. This measurement was done for each RF cell to complete this series of measurements.

From these data sets, it is obvious that a full measurement of the effect of all the tuning plates in this way is not useful for the RF setup of a 4-rod RFQ. Up to now, the positioning of the tuning plates has been done by an iterative process of shifting the plates. In [10] first attempts to structure this process was done with the implementation of the effect functions.

5 Simulation Methods of the Longitudinal Voltage Distribution

There are various attempts used to predict the flatness of 4-rod RFQs that have been around for a while. In general, the simulation technique with MWS as it is used in the design of 4-rod RFQs has been introduced in section 2.2.2. Another strategy that was followed in this thesis is based on the effect functions that are discussed in section 4.1.5. The experience of these studies in combination with early attempts like in [9] and techniques that are used in the 4-vane RFQ community [37] led to the development of the lumped circuit model that has been introduced in section 2.3. These methods with their application to 4-rod RFQs have been compared and analyzed in the following section. A different approach is to describe the 4-rod RFQ completely analytically by calculating the inductance and capacitance for each part of the RFQ based on its geometry. A model for that has been described for example in [53].

5.1 MWS Simulations

As presented in section 2.2.2, MWS is a powerful tool for RF simulations of accelerator cavities. One aspect of the simulations is the flatness prediction. The voltage between the electrodes is defined by the integral over the electric field component which is tangential to curves between the electrodes. Conventionally, the position of the integration path is chosen so that it is placed in the field maximum at the closest point between the electrodes. An example of such a curve (blue) is shown in Fig. 5.1.

For a proper simulation an enhanced meshing is needed compared to the standard eigenmode simulation leading to an enhanced solver time in the order of a hours. The volume around the electrodes tips needs to be modeled in detail with high resolution. In order to achieve this, a mesh refinement with a regular distribution of mesh cells is used like it is pictured in Fig. 5.2.

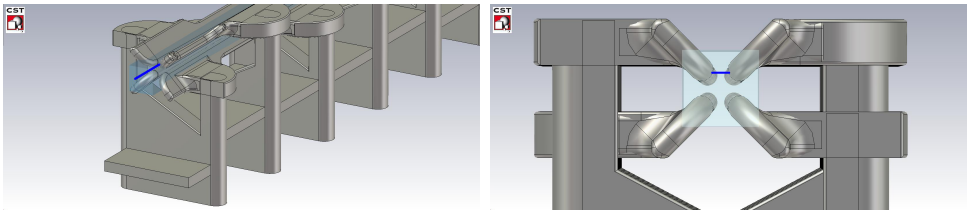

Figure 5.1: The curves for the simulation of the field flatness in CST. The electrode voltage in a simulation model can be calculated by the integral of the tangential electric field on curves between the electrodes.

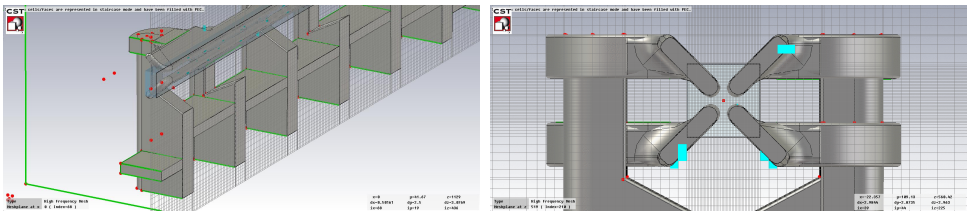

Figure 5.2: For field flatness simulations the mesh needs to be refined in the area of the electrodes and it has to be distributed equally.

In a first step, the flatness simulations concentrated on unmodulated RFQ models in order to analyze the influence of the tuning plates along the structure. A comparison of the simulation results for such a model and the corresponding measurement with no tuning and tuning plate 4 raised is shown in Fig. 5.3. In the simulation the untuned field flatness shows the typical tub form with a deviation of 9.2%. For comparison, the measurement is much flatter, with a deviation of 2.6%. The tuned field flatness when tuning plate 4 is raised shows the expected drop in the voltage, but the resolved distributions do not fit each other.

But when the effect function for tuning plate 4 is extracted from the simulation and the measurement, they nearly completely overlap as it is shown in Fig. 5.4. This is an example of a typical observation in 4-rod RFQs. The measured field flatness distribution is not reflected in the simulations, but the change that is induced in the distribution, the effect function, can be simulated with a good precision. But as it is visible in the graph in Fig. 5.4, the error in the simulation is more significant at the boundaries of the RFQ. The simulated effect in cells one to three is smaller than in reality.

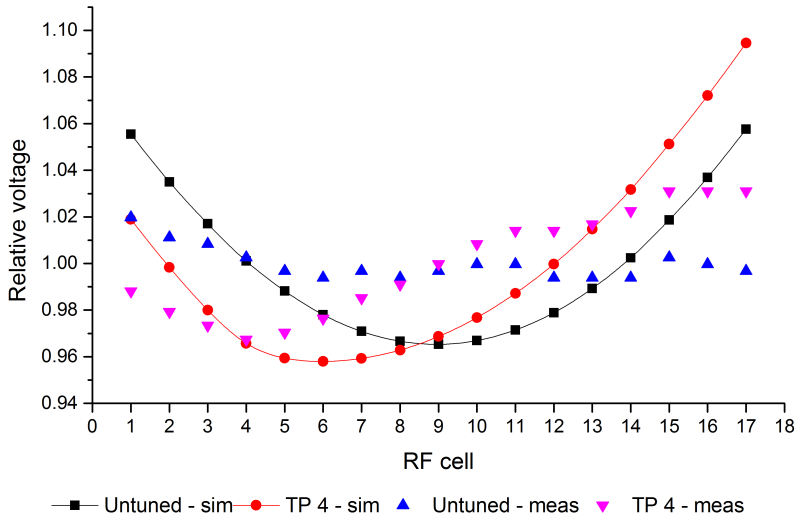

Figure 5.3: Comparison of MWS simulated field flatness to measurement for an untuned RFQ and the case with a tuning plate in RF cell $k = 4$. [48]

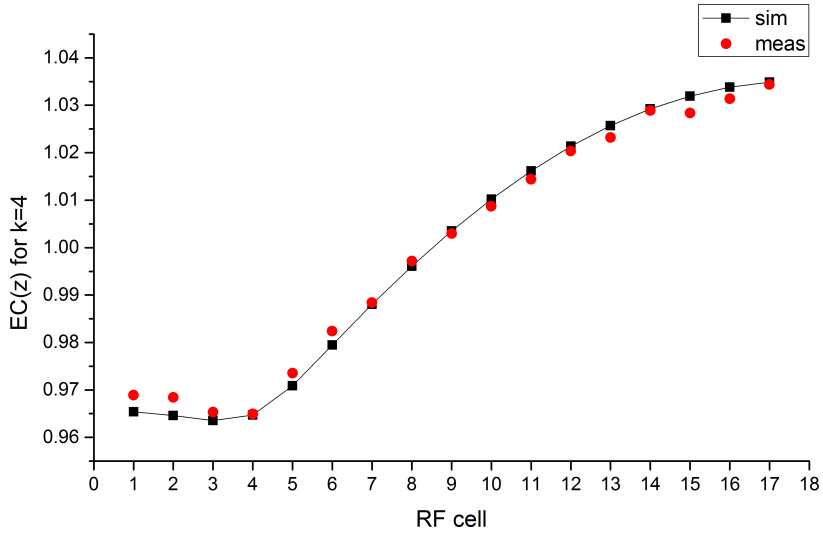

Figure 5.4: Comparison of a simulated and measured effect function $EC(z)$ for a tuning plate in RF cell $k = 4$.

To study the simulation of a model that is as close to reality as possible, complete CAD models of RFQs were imported into CST studio suite. Here all details of the modulation of the electrodes are included. Fig. 5.5 presents the results of such a simulated field flatness together with it's measurement for a certain tuning plate distribution in case of the FNAL RFQ. In this study, the meshing of the simulation volume has been analyzed in order to optimize the simulation accuracy. Five models with several million mesh cells have been developed. All of them have mesh distributions which differ slightly as they were refined step by step. The most obvious difference between the simulation and the measurement is a slope that all of the models show from the low to the high energy end of the RFQ. This slope is not present in the measurement. Except of that, the shape of the field flatness is similar, but still the comparison between the measurement and the simulation shows a deviation of up to 14%. Also other accompanying studies have shown similar results [27].

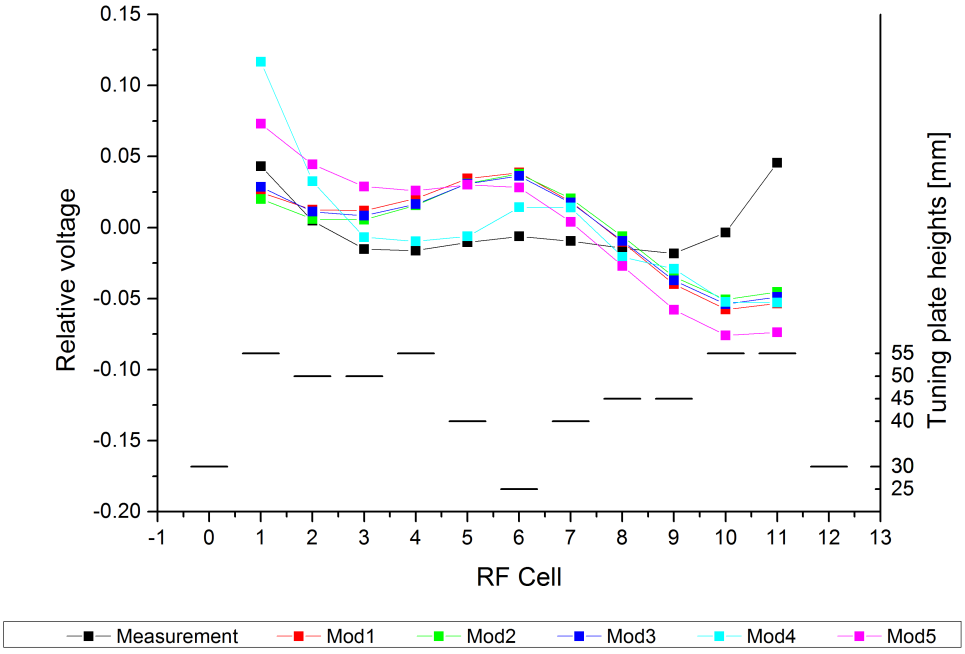

Figure 5.5: MWS simulation of the field flatness simulation of a full 3D CAD model, including modulated electrodes, for five different meshings, refined step by step. The simulation is compared to its measurement. All models give the shape of the measured field flatness, but they show a slope towards the high energy end that does not occur in the measurement.[56]

In summary, the MWS simulations of 4-rod RFQ's field flatness do not give results that can be used in the tuning design directly at the moment. But the change in the field flatness that is induced by a change of the structure or tuning plates can be predicted with reasonable accuracy. For particle tracking simulations there is a work around that can be used: the measured field flatness can be reproduced with a fictive tuning set up in the simulation. This method is used for example in [26]. Here, it is shown that advanced particle dynamic studies can be performed based on this approach.

5.2 Simulations based on Effect Functions of RF Cells

Based on the work of P. Fischer, who introduced the effect functions EC in [10], a NI LabVIEW program has been developed and tested for RFQs in the frequency range from 80 MHz to 200 MHz.

In section 4.1.5 the effect functions have been defined by

$$EC = \frac{U_T}{U_U} \tag{5.1}$$

to be the fraction of the tuned U_T to the untuned U_U voltage distribution. Each RF cell has a different influence on the RFQ depending on its longitudinal position and modulation profile as well as on the height of the tuning plate. So a single effect function $EC_k(z, h)$ for each tuning plate respectively each RF cell k can be defined.

If this function is known, the tuned flatness that corresponds to the positioning of a tuning plate in cell k with the height h_k can be calculated by

$$U_T(z, h_k) = U_U(z) + EC(z, h_k) \times U_U(z) \tag{5.2}$$

Measurements on the dependence of EC on h in 100 MHz RFQs show a linear growth for small heights that gets a minor quadratic part large hs.In order to simplify the calculations, the following approximation is made

$$EC_k(z, h) \to h_k \cdot EC_k(z) \tag{5.3}$$

The 4-rod RFQ can be described as a chain of coupled oscillators so the behavior of the complete system can be described by the superposition of the

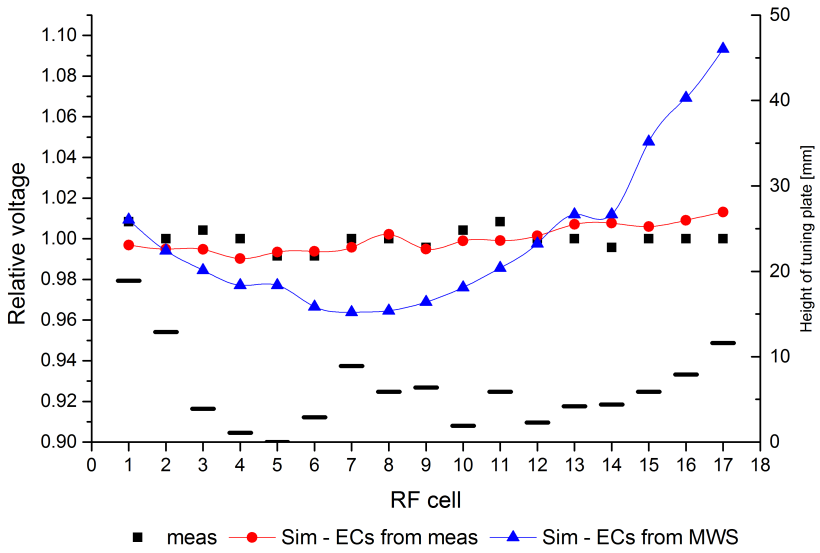

Figure 5.6: Field flatness simulation with effect functions generated by MWS simulation or measurement compared to a measured field flatness of a final tuning plate set up of a 80 MHz RFQ [48]. This study supports the approach to use measurements as the basis of a simulation model.

single oscillators [30]. So the field flatness that is created with a tuning plate distribution of N tuning plates can be calculated by

$$U_T(z,h) = U_U(z) \times \prod_{k=1}^{N} [h_k \cdot EC_k(z) + 1] \tag{5.4}$$

This opens up a strategic work flow for the field flatness tuning of 4-rod RFQs. The splitting of the z and h dependence of EC allows to define one set of EC for all k for one tuning plate's height. This set can be integrated into the program to predict the tuned field flatness so that different set ups of tuning plates can be tested before installation. The generation of the set of EC can be done either by measurement or simulation. In Fig. 5.6 these two methods are compared with the measured distribution. Here the dots are the measured values, the bars correspond to the final tuning plate distribution (TPV 12) of an 80 MHz RFQ. The measured ECs predict the red curve while the simulated ones result in the blue curve. The predictions based on simulated ECs are more exact than a pure MWS simulation of the system, but still the measured ECs bring the best result with the smallest deviation from the measured field flatness.

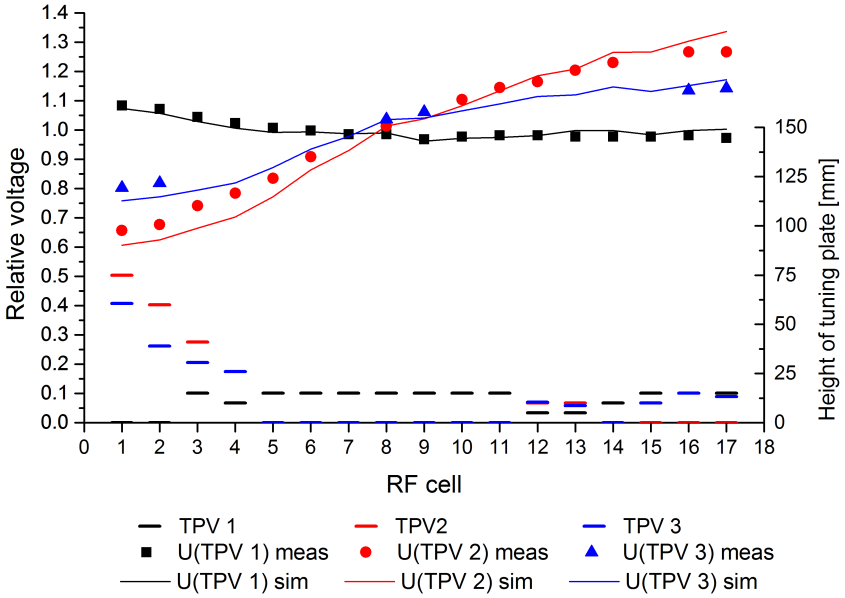

Figure 5.7: Results of field flatness simulations based on measured *ECs* for three arbitrary tuning plate configurations (TPV 1, 2 and 3) of a 80 MHz RFQ [48]. The accuracy of the simulation is good enough to be used in the tuning process.

In Fig. 5.7, three more tuning plate distributions (TPV 1-3) with their measured (dots) and predicted (curves) field flatnesses are shown. These are three setups that were tested in the tuning process of the RFQ and the trend of the flatness optimization is reproduced very well in the predictions.

The same theory was tested on RFQs with an operating frequency of 200 MHz. Compared to a 100 MHz RFQ this system, is much more sensitive to all perturbations in general [49]. This character reflects also the sensitivity on tuning implementations. The higher order dependency of the effect function $EC(z,h)$ on the tuning plate height becomes stronger (see Fig. 4.11) so that its linear approximation does not work anymore. Full sets of effect functions have been measured for this kind of RFQs as they have been presented in the previous sections. These measurements were analyzed and used to fit a higher order polynomial function for $EC(h)$ so that the height dependence as well as the longitudinal dependence were fully defined and imported into the program.

$$h_k \cdot EC_k(z) \rightarrow EC_k(h) \cdot EC_k(z) \tag{5.5}$$

The results of these simulations are shown in Fig. 5.8, where the measured field flatness (blue) is compared to the predicted distribution either with the linear approximation (green) or a polynomial fit (red). The results of the polynomial approach is overall smoother than the strongly varying distribution of the linear one. It reflects the total deviation between the maximal and minimal voltage, but the field flatness shape is not predicted to the desired accuracy. This model includes simplifications that are not working reasonable in the tuning of high frequency 4-rod RFQs.

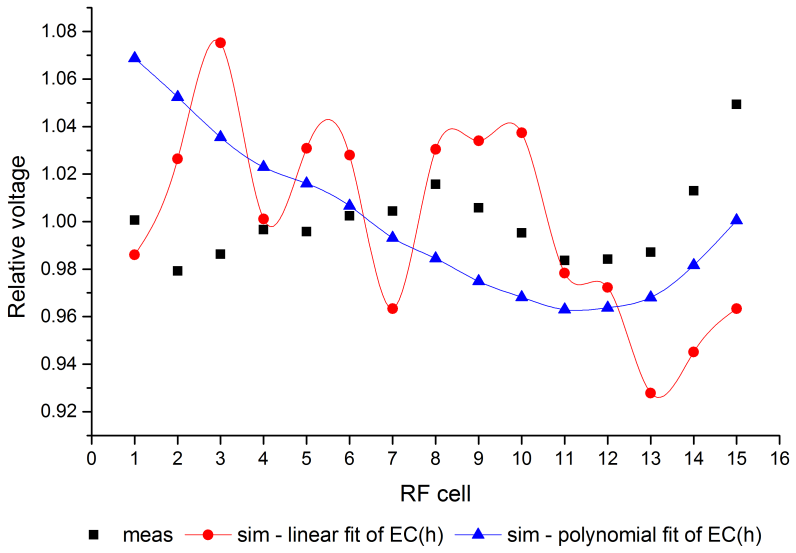

Figure 5.8: Results of field flatness simulations for a 200 MHz RFQ with linear or polynomial height dependence of EC [46]. Even with a polynomial ansatz in $EC(h)$ the effect funtions are not able to predict the field flatness with the desired accuracy.

5.3 Results of Lumped Circuit Simulations

In section 2.3 the lumped circuit model of the 4-rod RFQ has been introduced. In this system, the field flatness is defined by the voltage V_k in each tuning cell k. With the current J_k and the capacitance C_k of the cell k, V_k can be defined by the resonant frequency of the RFQ Ω by

$$V_k = \frac{J_k}{\Omega C_k} \quad \forall k = 0...N \tag{5.6}$$

The deviation in the relative field flatness in cell k compared to the mean absolute voltage of the full RF cells $k = 1...(N-1)$ is

$$\epsilon_k = \frac{|V_k| - \langle |V| \rangle}{\langle |V| \rangle} \tag{5.7}$$

The half cells of the RFQ with $k = 0$ and N are left out of the mean voltage because they are dominated by boundary effects and it is not possible to measure their voltage with an acceptable error as a perturbation capacitance has to much interaction with the boundaries here. Indeed, the tuning plates in these cells are not used for tuning, but are there to provide an optimal current flow between the vessel wall and the last stems. So, the normalized voltage of cell k is defined as

$$\text{normalized } V_k = \frac{|V_k|}{\sqrt{\sum_{m=1}^{N-1} |V_m|^2}} \tag{5.8}$$

An example of this normalized voltage distribution for the $\pi - mode$ in the currents is given in Fig. 5.9 together with the corresponding current profile.

The discussion on the eigenvectors and eigenvalues together with an analysis of the model in the operating mode of the 4-rod RFQ was given in section 2.3. Based on that theory the influence of the tuning plates can be treated similarly like second neighbor coupling, as a perturbation of the system. Compared to the RFQ model, when all tuning plates are at the bottom $h_k = 0 \ \forall \ k$ the inductance of cell k is changed from its original value $L \ \forall \ k$ to L_k.

$$L_k = L + \delta L_k \tag{5.9}$$

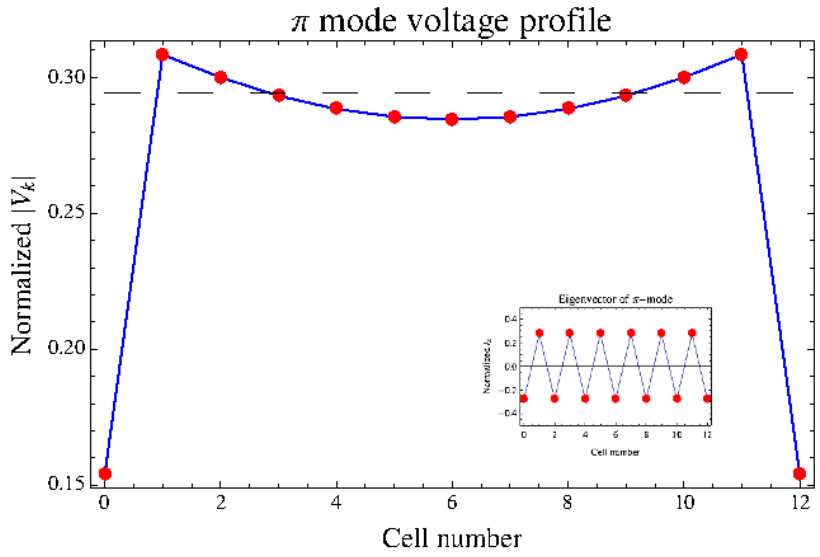

Figure 5.9: The normalized voltage in the π mode of the lumped circuit model compared to its currents. [56]

The cell frequency is shifted as well. In terms of the unperturbed cell frequency $\omega_c = \frac{1}{\sqrt{LC}}$ the shifted cell resonance frequency ω_k' can be written as

$$\begin{aligned} \omega_k' = \frac{\omega_c}{\sqrt{(1-\frac{\delta L_k}{L})}} \approx \omega_c(1-\frac{1}{2}\frac{\delta L_k}{L}) \text{ for } \delta L_k \ll L \\ \Rightarrow \frac{\delta L_k}{L} = \frac{-2(\omega_k' - \omega_c}{\omega_c} \equiv -\delta_k \end{aligned} \tag{5.10}$$

In the original matrix for the untuned system $\boldsymbol{U}(a_1, a_2)$ there are two terms which include the inductance: one on the main diagonal $L_k C$ and $\sqrt{L_k L_m} C$ for all other entries.

$$\begin{aligned} L_k C &\rightarrow (L + \delta L_k)C \\ &= LC(1 + \frac{\delta L}{L}) \\ \text{in terms of } \omega_c \ : \quad &= \frac{1}{\omega_c}(1 - \delta_k) \end{aligned} \tag{5.11}$$

$$\begin{aligned}
\sqrt{L_k L_m}C &= \sqrt{(L+\delta L_k)(L+\delta L_m)}C \\
&\approx LC\sqrt{(1+\frac{\delta L_k}{L})(1+\frac{\delta L_m}{L})} \\
\text{in terms of } \omega_c \ : \quad &= \frac{1}{\omega_c^2}(1-\frac{1}{2}(\delta_k+\delta_m)) \\
\text{with } \delta_k+\delta_m \equiv \Delta_{km} & \\
\text{and } \delta L_k \cdot \delta L_m \text{ neglected} \quad &= \frac{1}{\omega_c^2}(1-\frac{1}{2}\Delta_{km})
\end{aligned} \tag{5.12}$$

With the above as background the whole system can be summarized as the matrix $\boldsymbol{U}(a_1, a_2)$ that includes the unperturbed system described by $\boldsymbol{U}_0(a_1, 0)$, the second neighbor coupling perturbation $\delta\boldsymbol{U}_0(a_2)$ and the tuning perturbation $\delta\boldsymbol{W}_0(a_1, a_2)$.

$$\boldsymbol{U}(a_1, a_2) = \lambda_c^2\boldsymbol{U}_0(a_1, 0) + \delta\boldsymbol{U}_0(a_2) + \delta\boldsymbol{W}_0(a_1, a_2) \tag{5.13}$$

with

$$\delta\boldsymbol{W}_0 = \begin{pmatrix}
-\delta_0 & a_1\Delta_{0,1} & a_2\Delta_{0,2} & 0 & \dots & \dots & \dots & \dots & 0 \\
\frac{a_1}{2}\Delta_{0,1} & -\delta_1 & \frac{a_1}{2}\Delta_{1,2} & \frac{a_2}{2}\Delta_{1,3} & \ddots & & & & \vdots \\
\frac{a_2}{2}\Delta_{0,2} & \frac{a_1}{2}\Delta_{1,2} & -\delta_2 & \frac{a_1}{2}\Delta_{2,3} & \frac{a_2}{2}\Delta_{2,4} & \ddots & & & \vdots \\
0 & \ddots & \ddots & \ddots & \ddots & \ddots & \ddots & & \vdots \\
\vdots & \ddots & \ddots & \ddots & \ddots & \ddots & \ddots & \ddots & \vdots \\
\vdots & & \ddots & \ddots & \ddots & \ddots & \ddots & \frac{a_2}{2}\Delta_{N-3,N-1} & 0 \\
\vdots & & & \ddots & \ddots & \ddots & -\delta_{N-2} & \frac{a_1}{2}\Delta_{N-2,N-1} & \frac{a_2}{2}\Delta_{N-2,N} \\
\vdots & & & & \ddots & \ddots & \ddots & -\delta_{N-1} & \frac{a_1}{2}\Delta_{N-1,N} \\
0 & \dots & \dots & \dots & \dots & 0 & a_2\Delta_{N,N-2} & a_1\Delta_{N,N-1} & -\delta_N
\end{pmatrix} \tag{5.14}$$

Analogous to the analysis in section 2.3.1, the shift in the eigenvalue $\delta\Lambda_n$ and eigenvector $|\delta\Lambda_n\rangle$ are calculated. The results of the tuning influence are

$$\begin{aligned}
&\delta\Lambda_n = (\boldsymbol{J}^{-1})_n\delta\boldsymbol{U}_0(a_2) + \delta\boldsymbol{W}_0(a_1, a_2)\boldsymbol{J}_n \\
&\text{and} \\
&|\delta\Lambda_n\rangle = \sum_{l\neq n}^{N} \frac{(\boldsymbol{J}^{-1})_l\delta\boldsymbol{U}_0(a_2) + \delta\boldsymbol{W}_0(a_1, a_2)\boldsymbol{J}_n}{\Lambda_n - \Lambda_l}\boldsymbol{J}_l
\end{aligned} \tag{5.15}$$

If just one tuning plate in cell k is moved the correction in $|\delta\Lambda_n\rangle$ can be simplified to

$$\sum_{l\neq n}^{N} \frac{(\boldsymbol{J}^{-1})_l \delta \boldsymbol{W}_0(a_1,a_2)\boldsymbol{J}_n}{\Lambda_n - \Lambda_l}\boldsymbol{J}_l = \delta_k \sum_{l\neq n}^{N} w_l(a_1,a_2,k)\boldsymbol{J}_l \tag{5.16}$$

This separation of the inductance change δ_k with the height of the tuning plate and the w_l function is the ansatz that was discussion in section 5.2 for the separation of the effect functions to $EC(h)$ that is a function of h only and a longitudinal component $EC(z)$ that is a function of z only.

5.3.1 Application of the Lumped Circuit Model

The strategy for the application of the lumped circuit model is the following: first the value of L is calculated with EMS simulations. Then a_1, a_2, L and $\frac{\delta L_k}{L}$ are fixed by fitting MWS simulation results. Afterwards a set of capacitance corrections ΔC_k on C is extracted from measurements of the RFQ. Because in this model L and C are mathematically equivalent, so that L can be kept constant. If all these values are known, the system is defined and predictions of arbitrary tuning plate configurations are possible. The results are shown for the case of the FNAL H^- RFQ in table 5.1.

Calculation of C For the calculation of the capacitance C, the original electrodes of the RFQ are imported into CST EM Studio. Here, it is possible to associate a certain potential $V_{1,2,3,4}$ to the electrodes, as shown on the right side in Fig. 5.10, and calculate their capacitance matrix. The entries of this matrix correspond to the separated capacitances between all potentials in the system.

In order to define the real capacitance of the electrodes from this matrix the "quad star" model from transmission line theory that is introduced for example in [25]. The scheme of the quad star is shown on the left side of Fig. 5.10.

According to that model, the capacitance of the quadrupole electrodes can be separated into three parts. The first one is C_A, which is the capacitance of the four parallel capacitors c_{ij} between the neighboring potentials V_i and V_j.

$$C_A = c_{12} + c_{23} + c_{34} + c_{41} \tag{5.17}$$

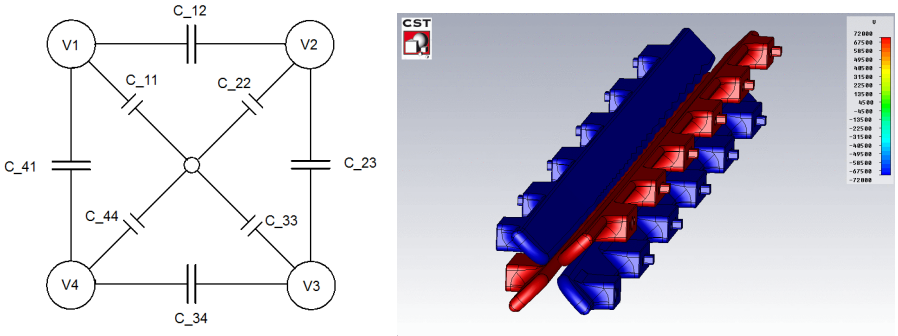

Figure 5.10: The capacitance of the quadrupole electrodes can be described by the "star quad" model from transmission line theory. [56]

The second ones are the capacitances C_B and C_C of two serial capacitors. They represent the capacitance of the electrode pairs at the same potential with respect to the boundaries. It should be remembered that the quadrupole configuration of the electrodes include the condition that $V_1 = V_3 = -V_2 = -V_4$.

$$\begin{aligned} C_B &= c_{11} + c_{33} \\ C_C &= c_{22} + c_{44} \end{aligned} \tag{5.18}$$

This configuration forms a π-network as described in [25]. In such a network the total capacitance C_T is given by

$$\begin{aligned} C_T &= C_A + \frac{C_B C_C}{C_B + C_C} \\ &= (N-1)C + 2 \times 2C \\ \Rightarrow \quad C &= \frac{C_T}{N+3} \end{aligned} \tag{5.19}$$

Fitting the coupling parameters a_1 and a_2 to MWS Data To find the values of the coupling parameters, two simulation results from MWS are fitted. One is the simulated field flatness of unmodulated electrodes[1] when all tuning plates are on the bottom and the other one is the resonance frequency for this set up. Both are necessary as $a_2 = \mu a_1$ and the eigenvector results themselves can not be distinguished as long as μ stays the same. A result of a least squares fit of the eigenvector from the lumped circuit model and MWS with variation

[1] The aperture of unmodulated electrodes in a MWS model is the mean aperture of the real electrodes weighted by the corresponding cell length.

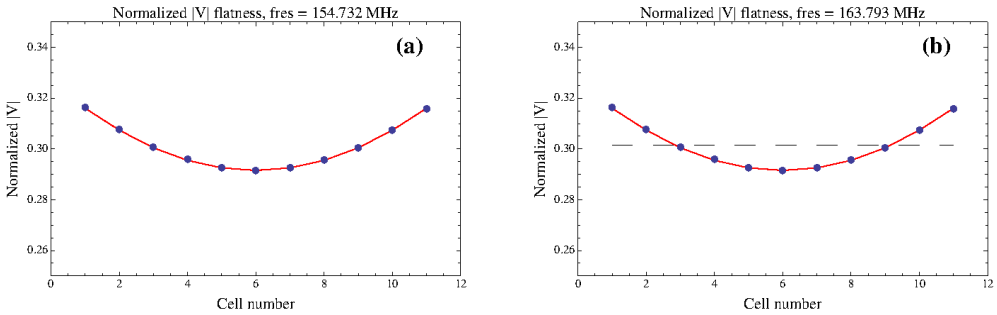

Figure 5.11: When a_1 and a_2 are fitted to MWS data the result for the field flatness stays the same as long as μ is kept constant, but the resonance frequency changes.[56]

of a_1 and μ is shown in Fig. 5.11. In the two graphs μ stays the same while a_1 is changed which leads to a change in the resonant frequency. Here it gets clear that a_1 determines the resonance frequency while a_2 dominates the curvature of the field flatness.

With the values of a_1 and μ fixed, the inductance L can be calculated using the definition of the RFQ's resonant frequency Ω_N in equation 2.36.

Fixing δL_k The studies that are presented in the simulations in Fig. 4.11 or the measurements in Fig. 4.22 show that the inductance due to the tuning plate's height can be represented by a quadratic function that can be found by fitting q and p to MWS data.

$$\delta L(h) = L(qh^2 + ph) \text{ with } \delta L(h) = \delta L_k(h) \; \forall \; k \tag{5.20}$$

Table 5.1

Parameter	Value in Case of the FNAL RFQ
Full RF Cells N	11
Capacitance C	8.3 pF
Inductance L	0.108 μH
first neighbor coupling a_1	0.0936
second neighbor coupling a_2	0.0031
inductance change parameter for h^2 q	$-1 \times 10^{-6}[\text{mm}^2]$
inductance change parameter for h p	$-0.38 \times 10^{-4}[\text{mm}]^{-1}$

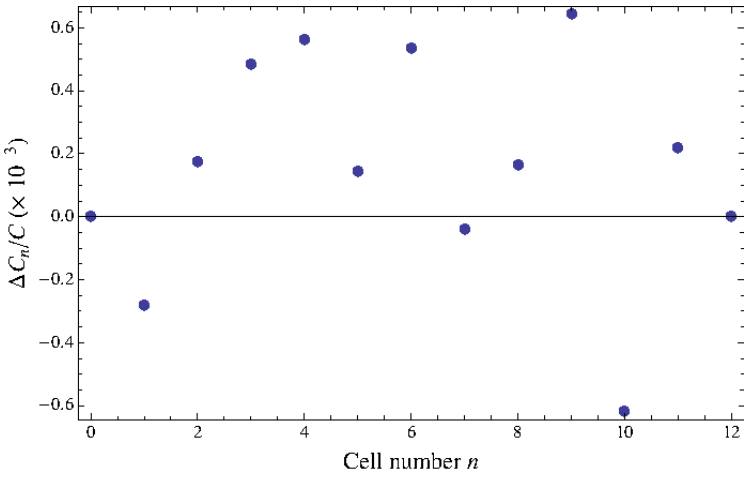

Figure 5.12: Fitted set of ΔCs for the adaption of the model to a measured field flatness. [56]

5.3.2 Adapting to Measured Field Flatness

When all these parameters are fixed, the model needs to be refined to fit to the measured field flatness. For this purpose a capacitance correction ΔC_k is introduced. This correction carries the influence of the varying modulation profile along the electrodes as well as deviations from the ideal case due to manufacturing defects. The full set of ΔC_k is shown in Fig. 5.12, extracted from the measurements of the effect functions EC_k.

Based on a set of ΔC_k from the measurement of two out of all tuning plates of the FNAL RFQ, the effect when each tuning plate in the full RF cells $k = 1...11$ is set to a height of 20 mm separately was simulated with the lumped circuit model described above. The results are presented in Fig. 5.13 (magenta squares) in comparison to the corresponding measurement (blue dots). The predictions fit the measurements quite well with just small deviations for the tuning plates in cells in the acceleration part of the RFQ with bigger modulation.

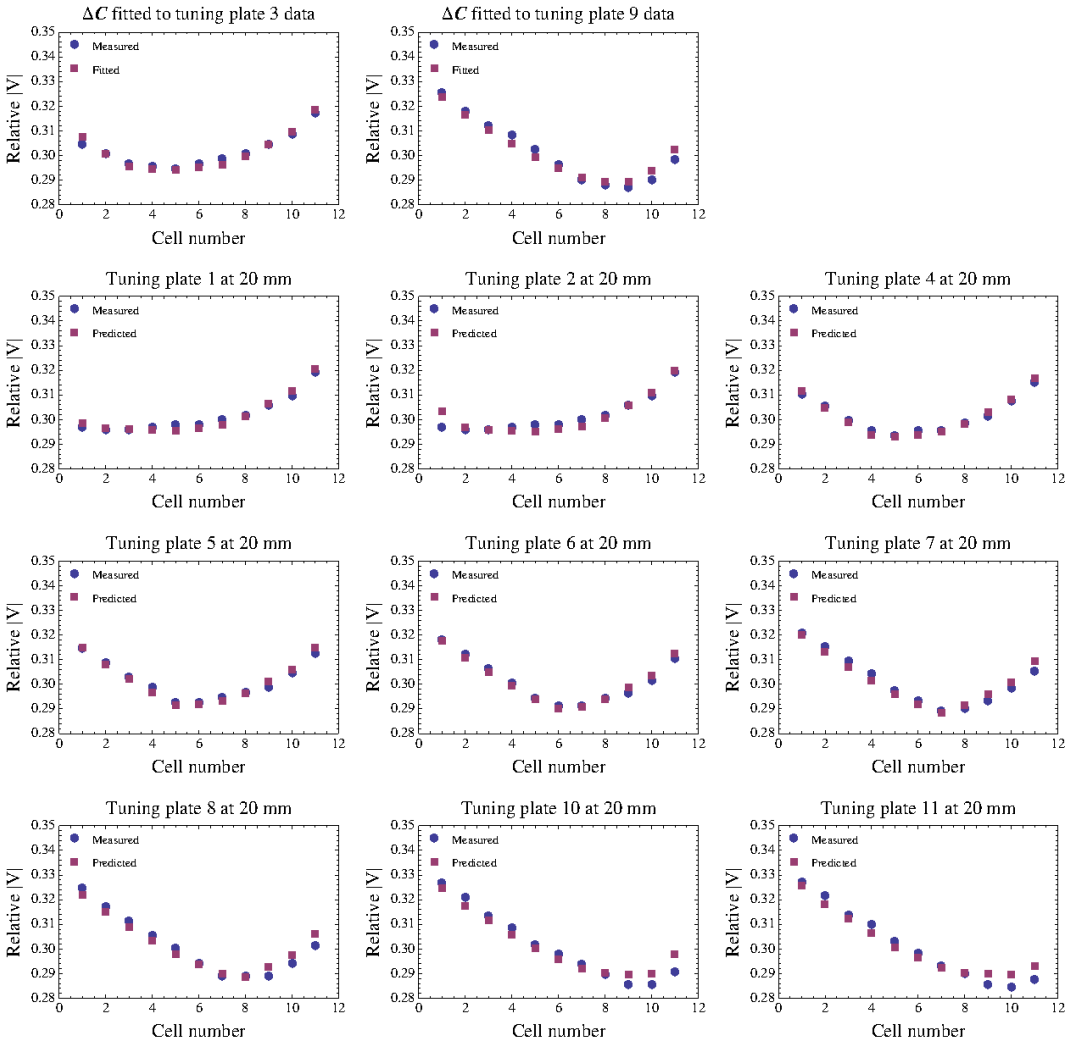

Figure 5.13: Prediction of a single tuning plate's influence with the lumped circuit model. The calculation is based on the set of ΔCs that is extracted from the relative voltage with tuning plate $k = 3$ and 9 at 20 mm. [56]

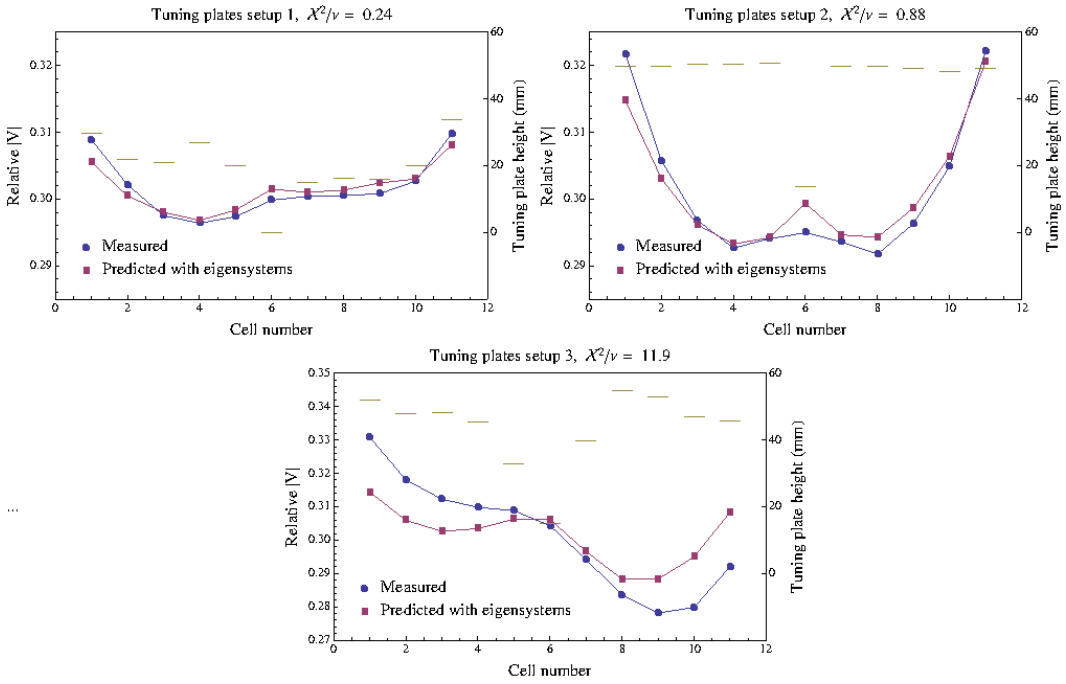

Figure 5.14: Simulation of the field flatness of three arbitrary tuning plate configurations of the FNAL RFQ with the lumped circuit model. The predictions show a good overlap with the measured distributions for setup 1 and 2. The deviation between measurement and prediction in setup 3 is a bit bigger, but still small enough to be used in the tuning process. [56]

To complete these studies, the measured field flatness of three arbitrary tuning plate configurations are compared to the lumped circuit results. For the quantification of the fit of the prediction to the measured data the reduced χ^2 is used.

$$\chi^2/\nu = \frac{1}{\nu}\sum_{k=1}^{N}\frac{(V_{rel.,meas.}(k) - V_{rel.,sim.}(k))^2}{\sigma_k^2} \tag{5.21}$$

where σ_k is the variance of the measurement in cell k, ν is the number of tuning plates in the full RF cells which is the degree of freedom for that system. The data of the relative voltages is plotted in Fig. 5.14. It fits the measurements quite well but χ^2 grows when the tuning plates are at high positions in the RF cell and their height h_k differ greatly from cell to cell.

6 The Longitudinal Electric Field

The accelerating field component in the RFQ is the longitudinal electric field E_z. In each neighboring acceleration cell of the modulated electrode, E_z has the opposite sign, so that particle bunches fill only every second cell, having a distance of $\beta\lambda$. The oscillation of E_z at full amplitude is shown in Fig. 6.1 for the example of a perfectly symmetric RFQ potential which has been extracted from a static simulation with CST EM-Studio® (EMS). The different stages in the RFQ from matching, with a small z-component for a high focusing strength, and bunching, where E_z rises slowly, to the nearly constant E_z of the acceleration part are clearly visible in this field distribution.

In this simulation, the potential on the electrodes has been fixed to a certain value. This is an ideal situation that can change dramatically in reality. Various effects lead to changes in the electrodes' potentials along the structure or differences in the potentials of each electrode. The field that includes all effects in the resonant circuit can be simulated with the Eigenmode Solver in MWS. In this case the simulation of the same RFQ model as it was used for Fig. 6.1 generates the E_z distribution presented in Fig. 6.2. Here the influence of the varying potential on the electrodes on the electric field is visible. The simulations are sensitive to the meshing, for example the sharp peeks in the field like the two between $z = 200$ and 400 mm. These peaks are artifacts of the meshing because they vanish when the meshing is varied. As mentioned above, from the accelerator physics view, the behavior of the field in the boundaries of the structure is the most interesting point here. In the comparison of between Fig. 6.1 and Fig. 6.2, the two broad peaks at the start and exit of the RFQ (markers) are outstanding. They are located just in the gap between the electrodes and the vessel wall. Such fringe fields can have different influences on the beam, for example a shift of the beam axis at the end of the electrodes or a shift of the particle energy. Other studies on this phenomenon of nonzero potential on the beam axis in RFQs are presented in [4] for a split coaxial RFQ and in [39] for a rod-type RFQ with symmetric supports.

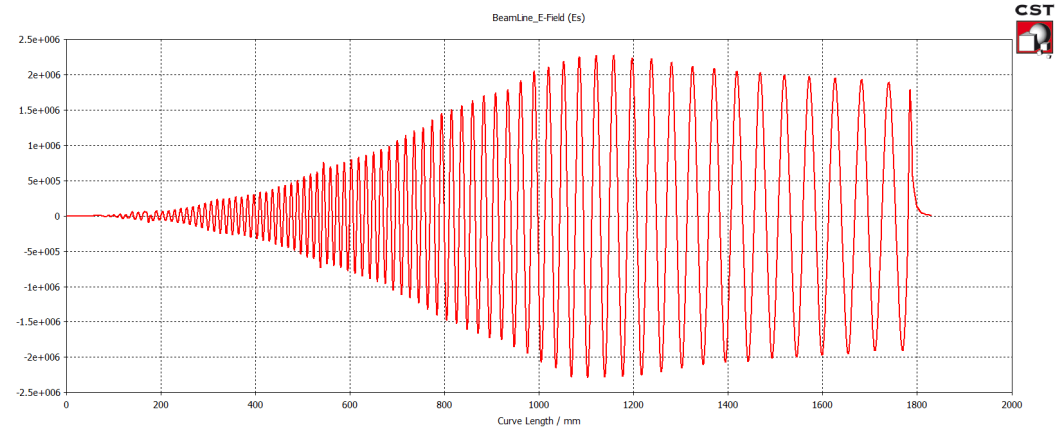

Figure 6.1: E_z in a static simulation with fixed potentials on the electrodes. The different sections of the RFQ can be seen in this distribution.

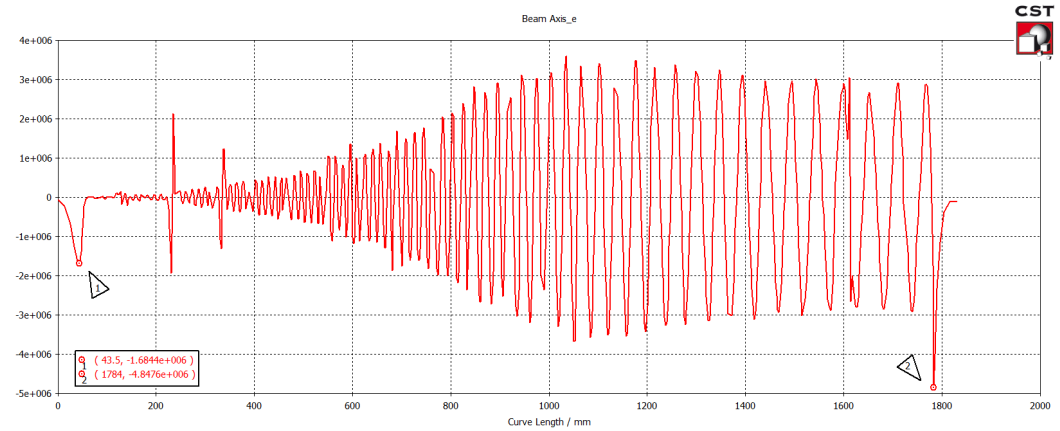

Figure 6.2: The same model as in Fig. 6.1 simulated in a resonant solver. In the comparison of the static and resonant simulation the two additional peaks (marked) at the entrance and exit of the RFQ. Their sources and influence on the beam are studied in this chapter.

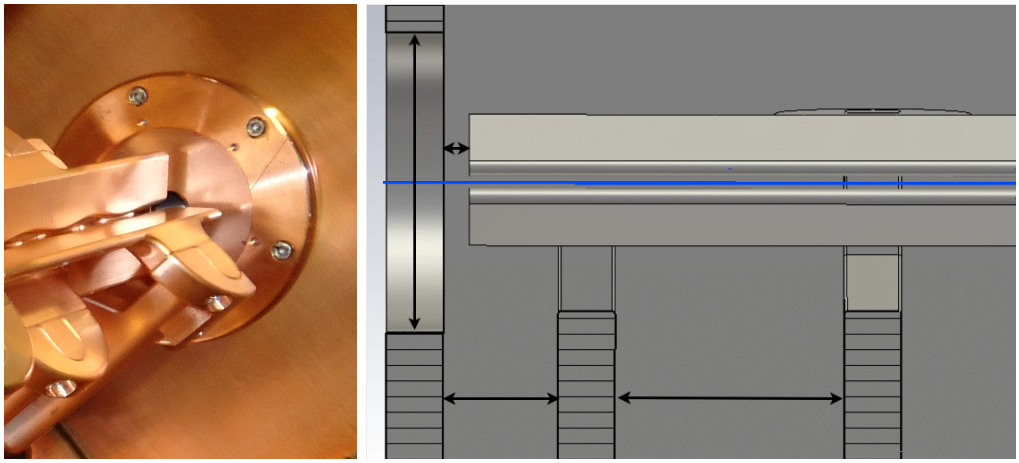

Figure 6.3: Mechanical set up in the boundaries of a 4-rod RFQ [51]. The picture on the right side illustrated the possible geometric parameter that can be used to influence the fringe field of the structure.

A view of the mechanical setup at the boundaries of a 4-rod RFQ and the parameters which can influence the fringe field is given in Fig. 6.3. The boundaries are specified mainly by two parts of the RFQ: first there is the last RF cell with the overlap of the electrodes behind the last stem and its ratio to the RF cell length, the distance to the tank wall and the last tuning plates – second there is the beam pipe that connects the RFQ to previous and following elements of the accelerator, and the RF shielding plate which is attached to the beam pipe that defines the aperture in the tank wall. With respect to the electric field one has to keep in mind that the 4-rod RFQ does not have any symmetry axis at its end, for example a TM-mode accelerator like the Alvarez has.

6.1 Optimization of 4-rod RFQ Boundary Conditions

In order to minimize the fringe fields of the 4-rod structure simulations of variations in the boundary design of the resonator and its influences on the fringe fields have been analyzed. The modulation on the electrodes has been removed in these studies, to exclude side effects. So E_z in the electrodes vanishes everywhere and only the peaks remain in the gaps which are presented in the following figures. As a first step, the geometric parameters of the overlap of the electrodes hanging over the last stem and the distances to the vessel wall are varied. Four different cases of these simulation series are shown in Fig. 6.4 with the geometric setup (left) and E_z at the beginning of the RFQ (right).

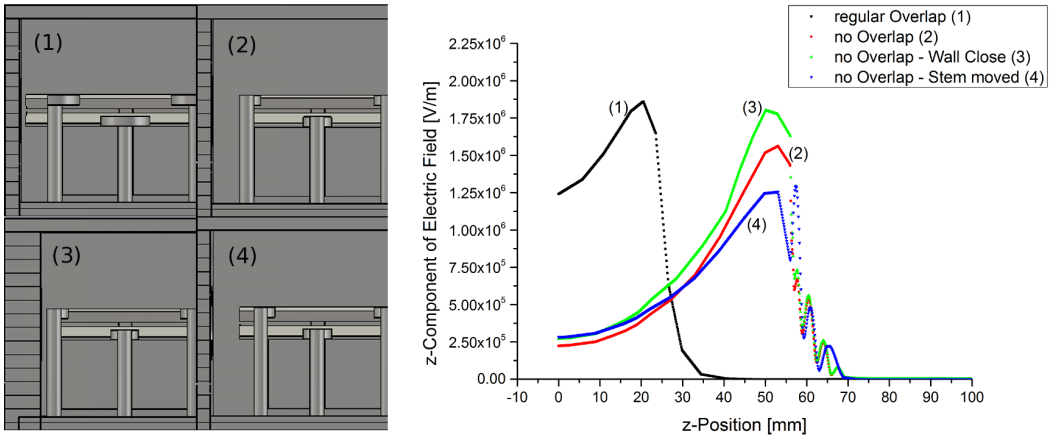

Figure 6.4: Simulation of the influence of the electrode's overlap. Four cases of a regular set (1), a cutted overlap with a huge gap to the wall (2) and a close wall(3) as well as an artificial overlap with a shorter last RF cell have been studied. The artificial overlap with the biggest space between the last stem and vessel wall shows the smallest fringe field of these cases. [51]

Case (1) corresponds to a regular RF design where the electrodes start at $z = 25$ mm. Starting from this geometry, in a first step, the overlap of the electrodes has been cut off, with the outer edge of the last stem at $z = 62$ mm for case (2). This change induces a suppression of the peak by a factor of almost 1.2 and a shift of the peak position due to the new end of the electrodes. Case (3) and case (4) are variations of case (2). In case (3), the distance between the vessel wall and the end of the electrodes of case (2) has been readjusted to the same value like in case (1). This small gap leads to an amplification of the peak back to the original amplitude like in case (1). Following the idea of case (2) applied to case (4), an artificial overlap has been created by moving the last stem closer into the RFQ which leads to a shorter last RF cell compared to the others. Here a reduction of the field peak by a factor of 1.44 can be achieved. This can also be seen in the voltage along the beam axis in a simulation without modulation on the electrodes. The only voltage a particle experiences here is the additional voltage on axis due to the fringe fields in the gap. Comparing the four cases, a suppression of this voltage by about 10% can be observed (see. table 6.1).

Table 6.1: Voltages on the Beam Axis for the Four Cases Presented in Fig. 6.4 with Reference to the Regular Overlap Model.

	Case	Voltage on Beam Axis
(1)	Regular Overlap	100%
(2)	No Overlap	98.56%
(3)	No Overlap - Wall Close	115.3%
(4)	No Overlap - Stem Moved	91.11%

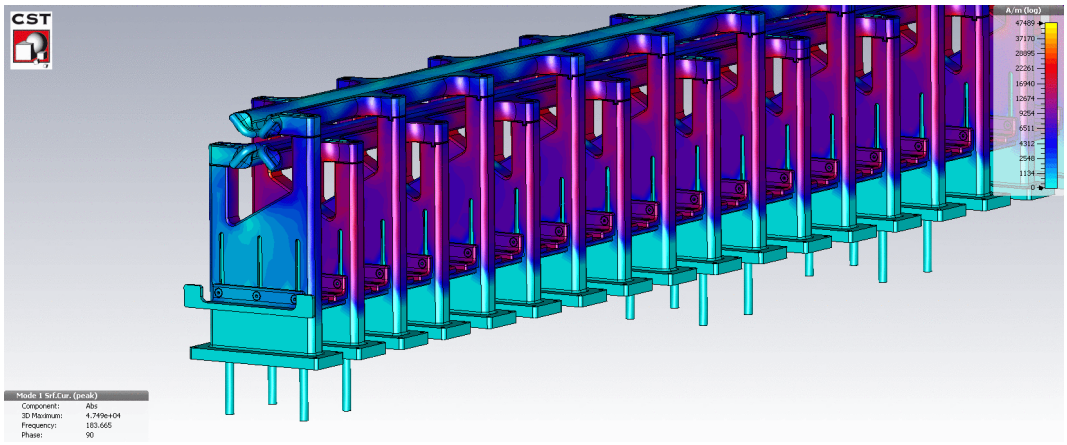

Figure 6.5: Simulation of the absolute currents on the 4-rod resonant structure. The current on the last stem is of less intensity than on the middle stems.

To summarize the results of these simulations, one can follow that the end geometry of the electrodes has a strong influence on the amplitude of the fringe field and that the magnetic field around the last stem needs to have enough space. The magnetic field encloses each stem. If there is only a small distance from the outer edge of the last stem to the vessel wall, the last stem's magnetic field is suppressed strongly compared to the other RF cells. This suppression leads to a lowered potential on the electrodes at their very last section connected to the last stems. This can be described by "cold" and "hot" electrodes, meaning a higher potential on the free electrodes, not connected to the last stem, compared to the fixed ones at the end of an RFQ. This effect becomes clearly visible when the absolute currents on the stems are displayed in Fig. 6.5. Compared to all other stems, the currents on outer side of the last stem has much less intensity.

For a quantification of this phenomenon, the voltage between the stems and the vessel side wall can be compared. This voltage is calculated by the

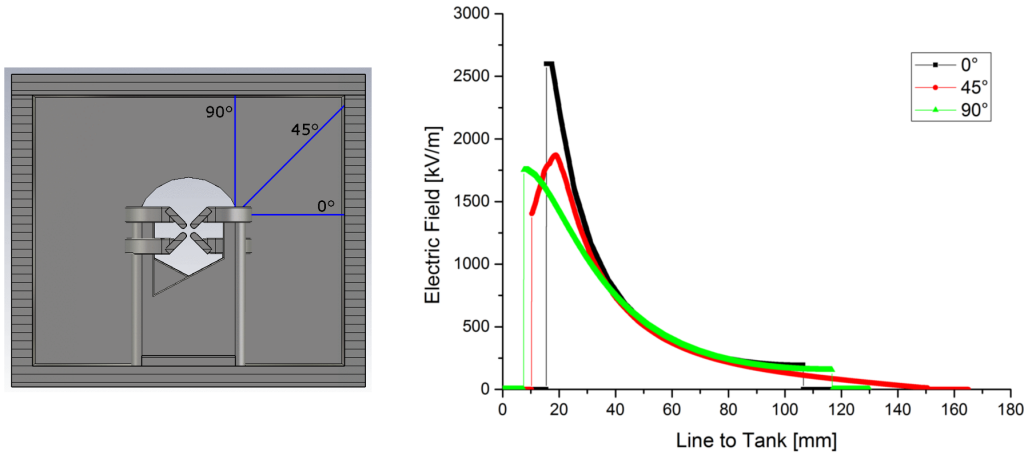

Figure 6.6: To compare the currents on the stems quantitatively the voltage between the stem and the vessel wall was calculated. This figure shows the tangential electric field on curves in different angles. The difference for the stem voltage for these angles is negligible.

integral over the tangential component of the electric field on the curves which are pictured in Fig. 6.6 (left) for different angles. Fig. 6.6(right) shows the influence of the curves' angle on the field along this integration path. The fields have a strong decay with a growing distance from the stem and vanish in the metal of the stem and the vessel. Due to the different field maxima and path lengths at different angles, the voltages vary as well, but the results for the stem voltage on these paths have a difference of up to one percent. This shows that the stem voltage is a robust value to study. Still, for an accurate comparison of different stems, the same position of the integration path is used. In the following discussions, this voltage will be referred to as the "stem voltage" U_{Stem} and if not named, the chosen angle is 0°.

The stem voltage for different stems along an RFQ for all four electrodes is pictured in Fig. 6.7. From this graph, a bunch of information can be extracted: (a) Comparing U_{Stem} between the last U_{StemL} and second last stems U_{StemS} of the RFQ reveals that in this standard RFQ simulation U_{StemL} is 17% of U_{StemS} at the low energy end and 15% at the high energy end of the RFQ, while two neighboring middle stems (11 and 12) show only a difference of about 2%. (b) In addition, this difference in the stem voltages longitudinally reflects the shape of the flatness described in chapter 2.3. (c) As a further point, the difference in U_{Stem} on just one stem has to be explained. For example, on the X

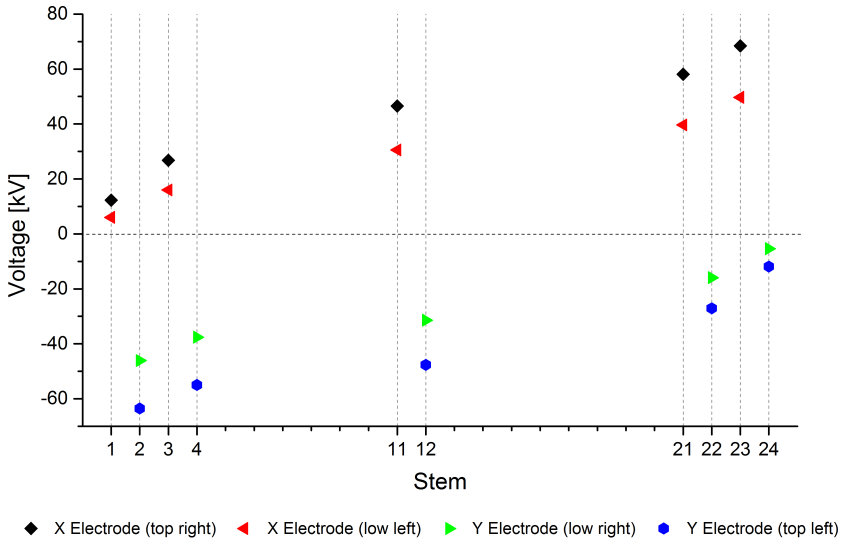

Figure 6.7: Stem voltage along the X and Y electrodes. The comparison shows a raise of the stem voltage from the fixed end of an electrode (for example X electrode at stem 1) to the free end (X electrode at stem 23). This distribution explains the differences between the hot and cold electrodes at the end of the RFQ.

electrodes the two data points on one stem are the stem voltages on both sides of the stem from the upper right arm (top right) or the lower left arm (low left) and vice versa on the Y electrode. Over the length of the electrodes, U_{Stem} on the lower electrode is less than on the upper one,i.e. there is a dipole effect between the lower and upper electrode pair. This dipole and its optimization is studied in detail in the PhD thesis of B. Koubek. Information on this subject can be found in his papers for example in [21], [24], [20] or [22].

In addition to the four cases of the boundary geometries discussed in Fig. 6.4 Fig. 6.8 shows U_{Stem} for the last U_{StemL} and a middle stem U_{StemM} with a growing electrode overlap (OVL) from no overlap to 40 mm when the distance between the vessel wall and the electrode end is kept constant. With a growing overlap, the difference gets sightly smaller, but there is no significant influence of the length of the overlap on a uniform stem voltage.

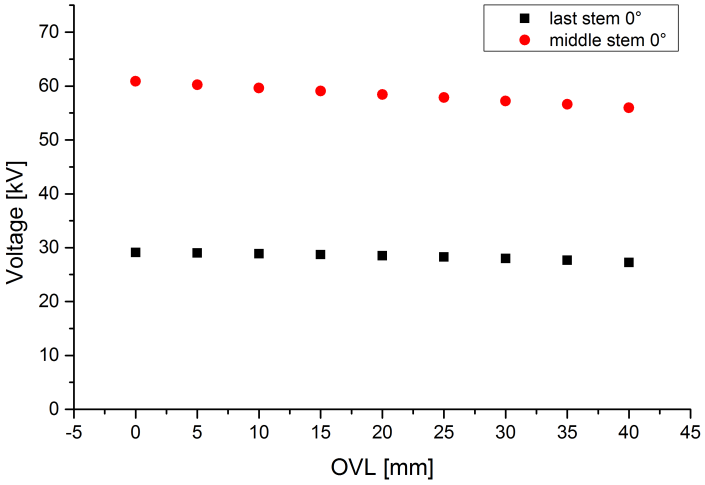

Figure 6.8: The stem voltage with a growing overlap from 0 mm to 40 mm. This variation has a very small influence on the stem voltage.

The idea to give the magnetic field enough space to close around the last stem was followed with another series of simulations for different shapes of the last stem. Fig. 6.9 presents two shapes of stems: one which consists basically of two columns holding the electrodes and another one with waist like cut outs on each side. They have been studied together with a third model where additional capacitances have attached to the vessel wall close to the electrode ends which are fixed at the last stem. The idea here is that these extra capacitances should raise the potential on these "cold" electrodes. In table 6.2 the results of these studies on the last stems are summarized. Compared is U_{Stem} of the last stem to the second last and a middle stem for all three end configurations and the standard RFQ model (case (1) Fig. 6.4). The extra capacitance has no influence on U_{Stem} because the differences between the stems remain the same in this case. But variations in the stem shapes show an effect on U_{Stem}. In the comparison of the last and second last stem ${}^{U_{StemL}}/_{U_{StemS}}$ the column stem raises the ratio by 4%; and in the comparison to a middle stem ${}^{U_{StemL}}/_{U_{StemM}}$ there is an increase of 5%. The stem with the waist shows a similar effect: an increase of 5% for ${}^{U_{StemL}}/_{U_{StemS}}$ and 7% for ${}^{U_{StemL}}/_{U_{StemM}}$ with respect to the reference model, case (1).

Table 6.2: Comparison of U_{Stem} of the last stem with the second last and middle stem.

Case	U_{StemL}/U_{StemS}	U_{StemL}/U_{StemM}
Case (1) Fig. 6.4	17%	24%
Column	21%	29%
Capacitance	17%	24%
Waist	22%	31%

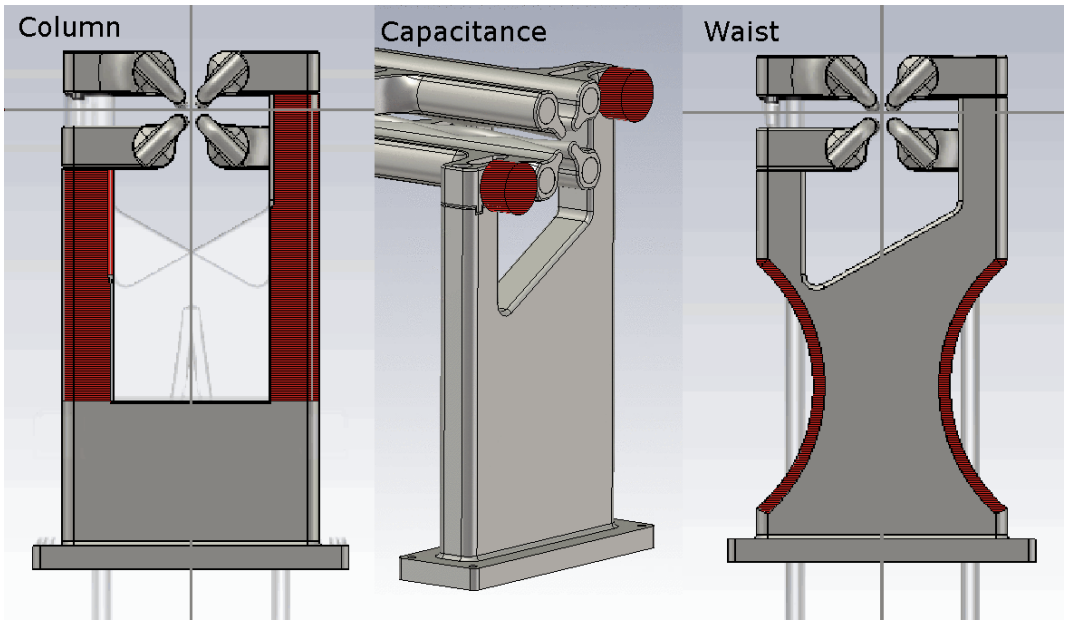

Figure 6.9: Alternative designs for the last stem have been studied to created additional space for the magnetic field to close around the last stem. According to table 6.2 the waisted stem shows the best results of theses study.

To conclude these investigations, two parts of the RFQ which were introduced in Fig. 6.3 remain to be discussed. These are the position of the tuning plate in the last RF cell and the aperture radius of the RF shielding plate. The fringe field with with two different positions of the last tuning plate is presented in Fig. 6.10. In these simulations of the standard RFQ model (case (1) in Fig. 6.4) two extreme cases are compared. The black line represents the peak in E_z when the tuning plate is at the bottom of the RF cell. Raising the tuning plate to its maximum position which has 55 mm free space under the plate increases the fringe field by a factor of 1.2.

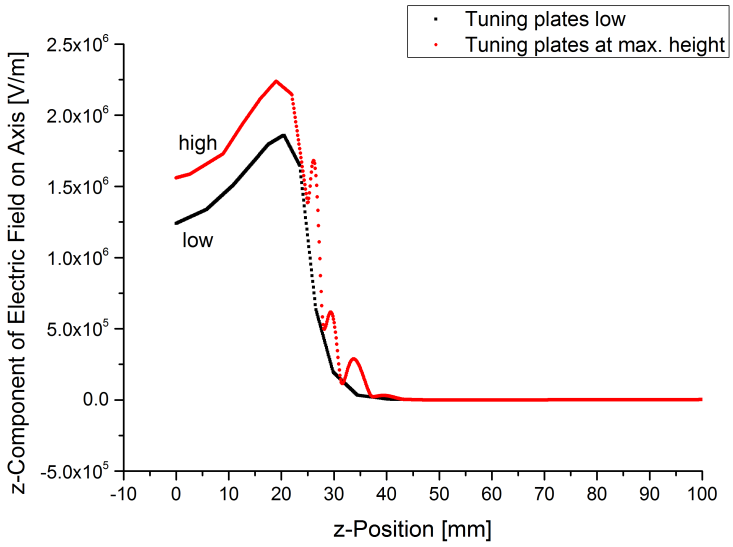

Figure 6.10: Fringe fields simulated with position of the tuning plate in the end RF cell [51][50]. When the last tuning plate is raised to its maximum position in the RF cell the fringe field is increased by a factor of 1.2 compared to the tuning plate on the bottom of the RF cell.

This behavior coupled with the reduction of the fringe field by an artificial overlap of the electrodes like it is discussed in Fig. 6.4 case (4) presents an important interaction. To create this overlap, the last stem of the RFQ is moved closer to the second last stem which leads to a shortening of the last RF cell. This change of the resonant circuit also changes the flatness as well (which was presented in section 4.1.2) so that the tuning implementation takes place mostly in the middle of the RFQ instead of the boundary cells in the standard RFQ model. So, the optimization of the fringe field benefits from this artificial overlap in both ways: the reduction of the fringe field due to better distribution of the magnetic field and the low position of the tuning plate in the outer RF cell.

As a last step in these studies, Fig. 6.11 shows the change of the fringe field due to growing aperture radius of the RF shielding from 3 mm to 75 mm. Following this approach, it is possible to reduce the fringe field in this case by a factor of nearly 5 and even for the bigger aperture of 40 mm a factor of 4.5 smaller peak in the fringe field can be achieved. Comparing the field peaks to the additional voltage a particle experiences due to the fringe field (Fig. 6.12), this opening reduces the voltage by more then 15%.

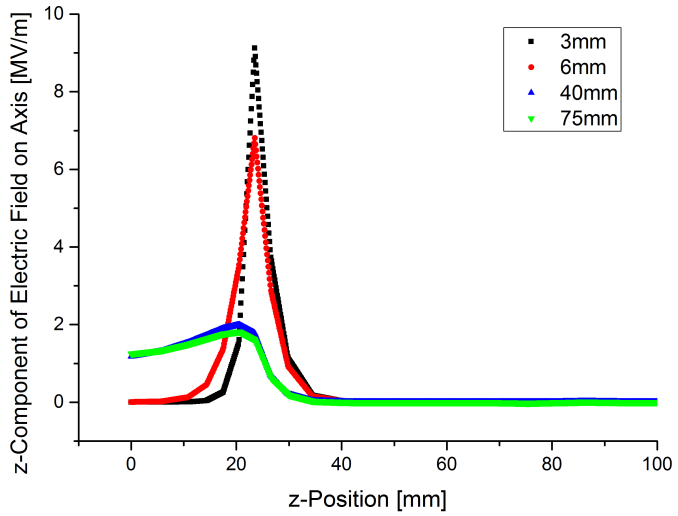

Figure 6.11: Fringe field with varying aperture of the RF shielding insert. The maximum field in the gap is reduced by a factor of 5 when the aperture is opened.[51][50]

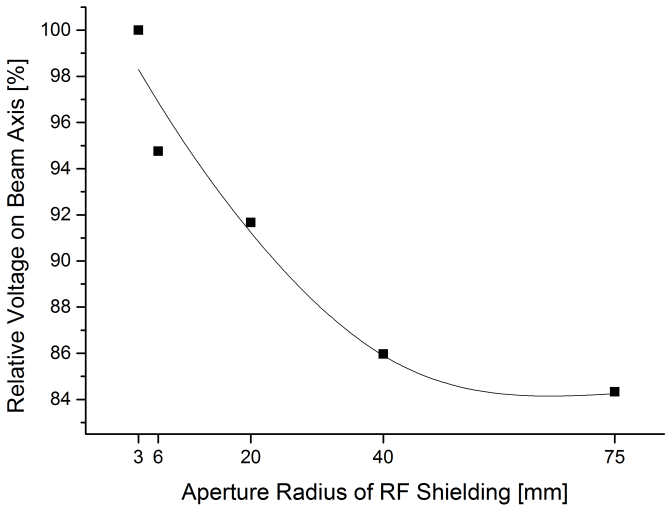

Figure 6.12: The voltage on the beam axis for different RF shielding apertures. It can be reduced by more than 15%.[50]

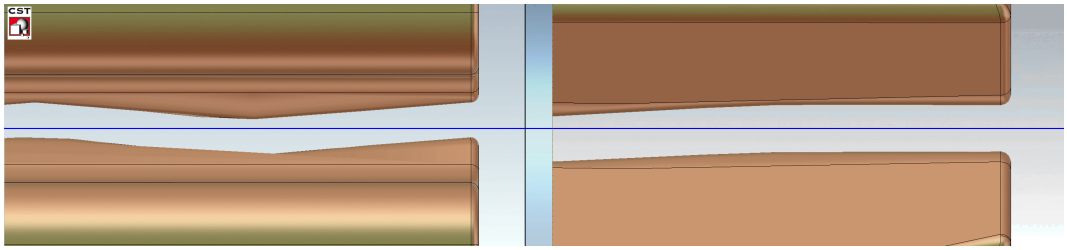

Figure 6.13: Picture of an electrode end with (right) and without (left) a Crandall Cell. The Crandall Cell provides a transition from the full modulation to a symmetric aperture at the end of the electrodes.

6.2 The Influence of 4-rod RFQ Fringe Fields on the Output Energy of the Beam

All these simulations study the fringe fields at the full amplitude of E_z. Their real influence on the ion beam is strongly dependent on the particle dynamic design of the RFQ. In an RFQ design where the electrodes end with a full acceleration cell, the configuration looks like the end of the electrodes in Fig. 6.13 on the left side. The particle are focused in one plane and defocused in the other one at the end of the electrodes. In this classical case, the synchronous phase of the design particle is 60° in the middle of the last RF cell. The phase values here refer to the sinus convention with the maximum electric field amplitude at 90°. At the cell end, the field has shifted to a phase of 150° typically. This corresponds to 50% of the maximum field strength on the falling edge of the RF when the particle enters the gap between the electrodes and the vessel wall in this classical design.

An alternative design that can be used in order to match the output distribution of the beam to the downstream parts of the LINAC includes a Crandall Cell at the end of the electrodes [7]. It consists of two parts: a transition cell [59] to merge the modulated acceleration cell to a symmetric point, that has the same aperture for x and y electrodes, and an unmodulated end part. This unmodulated section focuses the beam on a fitted length to form a symmetric transverse output distribution of the bunch. A picture of this configuration is given in Fig. 6.13 on the right side. Using a Crandall Cell the phase profile of the design particle at the electrode end is strongly changed. Compared to the classical case, the design particle enters the gap typically at a phase of 65°. This 90° phase shift means a change in the amplitude of E_z from 50% on the

falling edge to 90% of its maximum amplitude but on the rising edge of the RF phase in the moment the design particle enters the gap.

The energy gain ΔW of a particle with a charge q in the gap with a length L and a maximum electric field amplitude E_0 can be expressed by

$$\Delta W = qE_0L \cdot T \cos \Phi \tag{6.1}$$

where Φ is the phase shift of the particle arriving at the gaps origin compared to the crest of the RF field and T is the transit-time factor. T needs to be introduced in order to include the time dependence of the RF field while the particle travels through the gap. It corresponds to the ratio of the energy gain in an RF field compared to a non oscillating field.

$$T = \frac{\int_{-L/2}^{L/2} E_{(t=0,z)} \cos(\omega t(z)) dz}{\int_{-L/2}^{L/2} E_{(t=0,z)} dz} \tag{6.2}$$

From these equations it is obvious that the impact of the fringe field depends on the synchronous phase of the particle entering the gap, on the length of the gap and on the operating frequency of the RFQ [7]. The 4-rod RFQ is most sensitive to fringe fields at high frequencies that has a short gap between the electrodes and the vessel wall and when the design includes a Crandall Cell at the end. In general, fringe fields can be take care of in the particle dynamics, but in $Parmteq_M$ they are included only when there is no Crandall Cell in the design. This comes from the fact that the kind of fringe fields discussed here are not introduced by the asymmetry of the electrodes ending with a full acceleration cell (which are included in $Parmteq_M$ [8]), but are induced by intrinsic asymmetries of the RF structure.

To simulate the effect of the fringe fields on the particle's output energy which occur due to boundary conditions and the resonance behavior of the 4-rod RFQ, CST Particle Studio can be used. In this code, the fields of the eigenmodes of the resonator are calculated and then imported for the particle dynamics simulations. A result of the tracking solver is presented in Fig. 6.14. The upper picture shows a tracking result for an enhanced aperture in the RF shielding of 104 mm diameter. This geometry produces an maximum particle output energy of 751 keV, while a smaller aperture of 44 mm diameter leads to an maximal output energy of 740 keV for the same RFQ. This simple particle

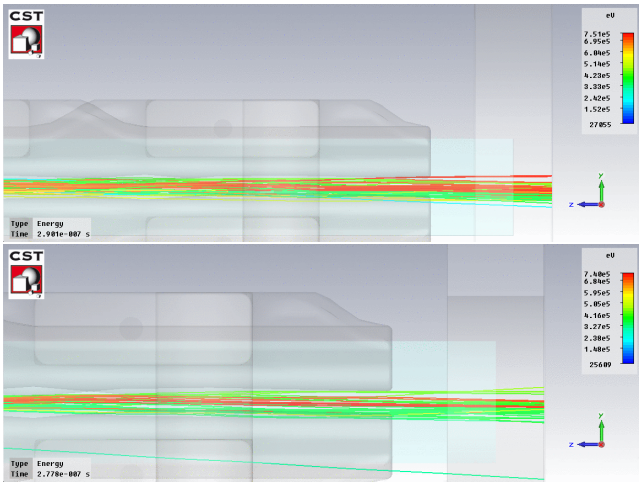

Figure 6.14: CST particle tracking simulations with a closed (upper picture) and open (lower picture) aperture of the RF shielding confirm its influence on the output energy of the RFQ.

tracking simulation shows a strong effect producing an output energy decrease of 11 keV by comparing two sizes of the end flange. Other simulations on this subject using the particle in cell method can also be found in [27] where it is shown the the particles are decelerated in the gap between electrodes and vessel wall.

6.2.1 Energy Measurements

These effects are not only visible in simulations, but also in beam measurements. Fig. 6.15 shows two setups in which the output energy of the beam at the FNAL H^--RFQ has been measured.

The results of these measurements are presented in Fig. 6.16. The data points in the left graph summarize the output energy measured with the time-of-flight method for several beam pickup (BPM) positions with the RF shielding in the RFQ (Fig. 6.15 "Before"). Here the output energy is 700±17 keV/u. Then the shielding was taken out and the output energy for the same RFQ was measured with a dipole magnet to be 756.5±0.5 keV/u (Fig. 6.15 "After"). These measurements confirm that a careful RF design study has to be performed with respect to the fringe fields in order to reassure the RFQ's output energy of the particle dynamic design [50].

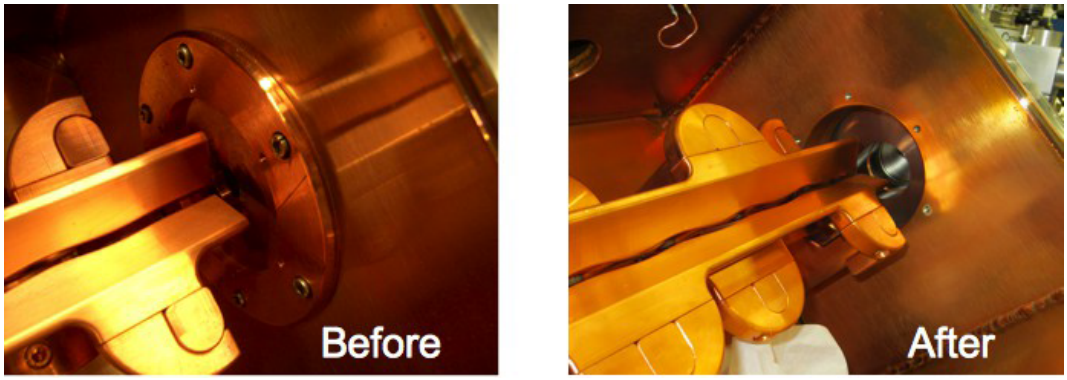

Figure 6.15: The output energy of the RFQ was measured in the two set ups shown in this picture [50]. In the first measurements of the FNAL RFQ the RF shielding was inserted at the low and high energy end of the RFQ. After the modification it was removed at the high energy end and its aperture was increased at the low energy end of the RFQ.

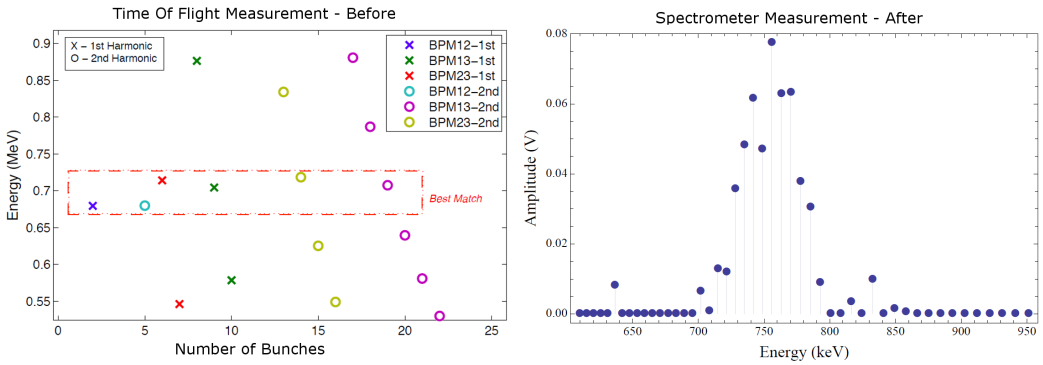

Figure 6.16: Measurement of the output energy of both cases "Before" and "After" the modification of the FNAL RFQ [50]. The measurements show a shift from 700 keV/u with the RF shielding to 750 keV/u without it.

7 Conclusion and Summary

The main subject of this thesis is the optimization of the electric field distribution in the RF design and tuning of 4-rod RFQs. In this work on four RFQ projects, with a range of operating frequencies from 80 MHz to 216 MHz three main research aspects are addressed:

1. Basic studies on the characteristics of the longitudinal voltage distribution, called the *field flatness*, that includes the influence of RF design elements and systematic measurements, for a better understanding of its behavior.

2. The analysis of three different simulation methods for the prediction of the field flatness and especially the development of the lumped circuit model for the simulation of the tuning plate's influence on the field flatness.

3. The optimization of the fringe fields in the 4-rod RFQ structure with studies on the influence of the mechanical design parameters on these field peaks.

7.1 Electric Field Distribution in the 4-rod RFQ

Detailed simulations on the various influences that elements of the mechanical and RF design of 4-rod RFQs have on the electric field distributions are presented in this thesis. Both the studies on the field flatness along the RFQ that are discussed in chapter 4 as well as the fringe fields in the gap between the electrodes and the vessel wall in chapter 6 lead to a better understanding of the resonant behavior and symmetries of the RFQ.

The results of these studies can be used to improve the RF design. Fig. 7.1 shows a possible version of an RFQ model which includes the findings from these chapters. The three main improvements of this model are a reduced stem distance in the end RF cells, an enhanced space for the magnetic field around the last stem and the RF shielding position.

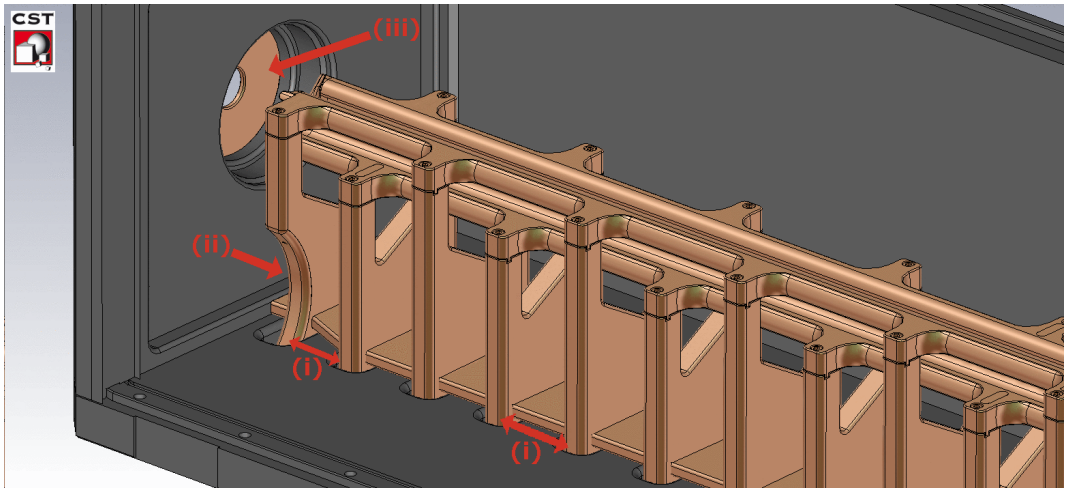

Figure 7.1: Parameters for an improved field distribution of the 4-rod RFQ. The model includes reduced stem distance in the end RF cells (i), an enhanced space for the magnetic field around the last stem (ii) and an optimized RF shielding position (iii).

Reduced Stem Distance in End RF Cells In section 4.1.2 the change in the field flatness caused by a variable stem distance is presented. Fig. 4.5 shows the field flatness with a reduced stem distances in the boundary RF cells. In principle this effect can be used in the RFQ design to generate any desired field flatness by adapting the stem positioning. Since simulation techniques, like CST MWS whose accuracy is discussed in section 5.1, and manufacturing processes have improved fast in the last few years, one can think of RF designs in which the length of each RF cell is fitted to its capacitance so that tuning plates will no longer be needed. Such an 4-rod RFQ could just be tuned just with dynamic tuners used in operation. But even today, the simulation accuracy allows the use this parameter. For example the Los Alamos RFQ design includes three shortened RF cells at the beginning and end of the structure [28]. But this is not only about the field flatness. As it was shown in the analysis of the last tuning plate's influence on the fringe field (see Fig. 6.10) in section 6.1 the last tuning plate contributes to it. With a reduced RF cell length, the shape of the field flatness switches, so that its maximum is moved from the end RF cells to the middle of the RFQ. With this effect, the plates in the outer RF cells can be kept low, following the results of section 6.1. In addition, the field maximum in the middle of the RFQ assures optimum bunching performance of the RFQ which is important for the transmission of

the structure (see Fig. 4.1). The model in Fig. 7.1 has this kind of RF cell length variation with three shorter RF cells at the ends.

Enhanced Space for the Magnetic Field Around the Last Stem The studies of the electrode's overlap and the analysis of the stem voltage in section 6.1 showed that the fringe fields can be lowered if the distance between the last stem and the vessel wall is increased. This creates more space for the magnetic field around the last stem to develop what increases the field symmetry at the ends of the RFQ. The same effect can be supported with a waist form applied to the design of the last stem as illustrated in the model in Fig. 7.1 where the waisted end stem is combined with an enhanced space to the vessel wall.

RF Shielding Position In comparison to all elements that were studied in section 6.1, the RF shielding insert at the end flanges of the RFQ has the strongest influence on the fringe field. Simulations of the electric field of the RFQ's electrodes show the boundaries of this field can reach into the aperture of the RF shielding and can be perturbed by it. The easiest way to avoid this is to insert no RF shielding at all, like it is shown for the beam energy measurements in section 6.2.1. But if sensible devices are connected to the RFQ the shielding is needed to avoid RF leaking out of the RFQ. In this case there are two possibilities: Either the aperture can be big enough to fulfill the compromise between shielding and non perturbing the electrode's field or the RFQ vessel can be designed, such as in Fig. 7.1, where the RF shielding is attached from the outside of the connecting flange.

7.2 Conclusion of Field Flatness Simulation Methods

In chapter 5 three simulation methods of the field flatness are discussed. The advantages, disadvantages and limitations of these models will be discussed in this section.

CST Microwave Studio The first one is CST MWS that is the standard simulation software for the RF design of 4-rod RFQs. This program is able to calculate the eigenmodes of the resonator with its fields and all characteristics like resonant frequency or for example losses and current distributions. From these simulations, the field flatness of any tuning plate configuration can be extracted. Of all three methods that are compared, this is the only approach that does not rely on any input data from measurements of a structure but produces results from a computer model. In general this makes it a powerful tool that has been used successfully in the design of many different accelerator types. For the 4-rod RFQ, the MWS prediction of the eigenmodes in the initial state of the structure with MWS is accurate in the order of a few MHz for the resonance frequency. The relative distributions of currents or energy density distributions can be analyzed using this simulation tool. Still, the studies on the field flatness simulation show that the accuracy of its prediction is not good enough to be used in the tuning process [56][27]. The detailed resolution of the RFQ's modulated electrodes with its strongly inhomogeneous fields is still a challenge. Currently, MWS works well for calculations of the relative changes that are induced by parameter variations. For accurate predictions of detailed field distributions and the tuning plate's influences further improvements in the simulation of the transmission line resonator need to be made.

Effect Functions The other two simulation methods are both based on measured data of the RFQ which are then extrapolated for other tuning plate configurations using different approaches. The first that was followed is the calculation of the field flatness with effect functions in section 5.2 which were introduced in [10]. This theory was realized in a LabVIEW based software and shows really good results for RFQs that have an operating frequency around 100 MHz [48]. For RFQs at operation frequencies of 200 MHz, this theory does not working anymore. Simplifications that work well for lower frequency structures which show a more linear behavior in the tuning cannot be adapted

in more sensible resonators with higher frequencies. Even with refinements, the theory of effect functions in this form can not be used in these cases (see Fig. 5.8). Still, the inductance change $\delta L/L$ in the application of the lumped circuit model is the same as the height dependence $EC(h)$ in the effect function $EC(z,h) = EC(h_k) \cdot EC_k(z)$. This could be a possibility to implement in this model to improve its performance.

Lumped Circuit Model The experiences and calculation approaches that are known from the 4-vane RFQ community lead to the development of the lumped circuit model [56]. This model uses an analytic description of the RFQ as a chain of inductively coupled LC resonators, fits this model to MWS simulation results before it is adapted to the data of a measured RFQ. Its results are presented in section 5.3. Smooth tuning plate distributions are reflected precisely while for configurations in which the tuning plates are in high positions with deviations in their height from cell to cell the deviation between simulation and measurement grows in the high energy part of the RFQ. This behavior is similar to MWS simulations, but while MWS overestimates the effect of the tuning plates in this part of the RFQ the lumped circuit model underestimates it slightly. Of the three methods that were studied in this thesis, the lumped circuit model shows the most accurate results of the field flatness for certain tuning plate configurations when compared to its measurements of a 200 MHz RFQ.

7.3 Summary

In this thesis, the tuning process of the 4-rod RFQ has been analyzed and a theory for the prediction of the tuning plate's influence of the field flatness was developed together with RF design options for the optimization of the fringe fields.

The basic principles of the RFQ's particle dynamics and resonant behavior are introduced in the theory chapter 2. All studies that are presented are based on the work on four RFQs of recent linac projects. These RFQs are described in chapter 3. Here, the projects are introduced together with details about the RFQ parameters and performance. In the meantime two of these RFQs are a in full operation at NSCL at MSU and FNAL. One is operating in the test phase of the MedAustron Cancer Therapy Center and the fourth one for LANL is about to be built. In chapter 4, the longitudinal voltage distribution has been studied in detail with a focus on the influence of the RF design with tuning elements and parameters like the electrodes overlap or the distance between stems. The theory for simulation methods for the field flatness that were developed as part of this thesis, as well as its simulation with CST MWS have been analyzed and compared to measurements in chapter 5. The lumped circuit model has proven to predict results with an accuracy that can be used in the tuning process of 4-rod RFQs. Together with results from chapter 4, the studies that are presented in chapter 6 on the fringe fields of the 4-rod structure lead to a proposal for a 4-rod RFQ model with an improved field distribution in the transverse and longitudinal electric field as it is summarized in section 7.1.

In summary, it has been shown that the RF design has been improved in the last few years leading to a better performance of the 4-rod RFQ. The development of RFQs with tight requirements is possible using a combination of classical RFQ design codes like Parmteq, modern numerical simulation techniques like CST Microwave and Particle Studio together with advanced manufacturing technology and an enhanced strategy in the tuning process of the field flatness.

Bibliography

[1] Chao, A. W. and M. Tigner: *Handbook of Accelerator Physiks and Engineering*. World Scientific Publishing Co. Pte. Ltd., 2006.

[2] Chidley, B. G., R. M. Hutcheon and G. E. McMichael: *A heavy ion RFQ with high accelerating gradient*. In *Proc. LINAC 1986, Stanford, California, USA*, page 361, 1986.

[3] Chidley, B. G., G. E. McMichael and R. M. Hutcheon: *Tilted Field RFQ's - An Alternative Design Approach*. In *Proc. PAC 1987*, page 1913. IEEE, 1987.

[4] Comunian, M. and A. Pisent: *Input and output matching for a RFQ where a couple of electrodes are at ground potential*. In *Proc. LINAC 1994*, page 737, 1994.

[5] Comunian, M., A. Pisent and E. Fagotti: *The IFMIF-EVEDA RFQ: Beam Dynamics Design*. In *Proc. LINAC 2008, Victoria, BC, Canada*, page 145, 2008.

[6] Courant, E. D. and H. S. Snyder: *Theory of the Alternating Gradiant Synchrotron*. Ann. of. Phys., 3:1, 1958.

[7] Crandall, K. R.: *RFQ Radial Matching Sections and Fringe Fields*. In *Proc. LINAC 1984, Seeheim, Germany*, 1984.

[8] Crandall, K. R., T. P. Wangler, L. M. Young, J. H. Billen, G. H. Neuschaefer and D. L. Schrage: *RFQ Design Codes*. Technical Report LA-UR-96-1836, Los Alamos National Laboratories, 2005.

[9] Fang, J. X. and A. Schempp: *Equivalent Circuit of a 4-rod RFQ*. In Corbett, J. et al. (editors): *Proc. EPAC 1992, Berlin, Germany*, page 1331, March 1992.

[10] Fischer, P.: *Ein Hochleistungs-RFQ-Beschleuniger für Deuteronen.* PhD thesis, IAP, Goethe University, Frankfurt am Main, 2007.

[11] Fokas, E., G. Kraft, A. Hanxiang and R. Engenhart-Cabillic: *Ion beam radiobiology and cancer: Time to update ourselves.* Biochimica et Biophysica Acta (BBA) - Reviews on Cancer, 1796(2):216, 2009.

[12] Fortgang, C.: *A SPECIALIZED MEBT DESIGN FOR THE LANSCE H+ RFQ UPGRADE PROJECT.* In *Proc. NA-PAC 2013, Pasadena, CA, USA*, 2013.

[13] Garnett, R. W.: *Status of the LANSCE Front End Upgrade.* In *Proc. NA-PAC 2013, Pasadena, CA, USA*, 2013.

[14] GmbH, Firma Kress. Biebergemünd Wirtheim, Germany, www.firma-kress.de.

[15] Halbach, K. and R. F. Holsinger: *Superfish – a computer program for evaluation of RF cavities with cylindrical symmetry.* In *Part. Accel. 7*, page 213, 1976.

[16] Kapchinskiy, I. M. and V. A. Tepliakov: *Linear Ion Accelerator with Spatially Homogenous Focusing.* Prib. Tekh. Eksp., 2:119, 1970. Engl. Übersetzung.

[17] Kapin, V.: *A new analysis of 4-rod radio-frequency quadrupole linac with intrinsic field distortions.* Jpn. J. Appl. Phys., 36(Part 1, 4A):2415, April 1997.

[18] Kester, O., D. Bazin, C. Benatti, J. Bierwagen, G. Bollen, S. Bricker, A. C. Crawford, S. Chouhan, C. Compton, K. Davidson, J. DeLauter, M. Doleans, L. Dubbs, K. Elliott, A. Lapierre, W. Hartung, M. Johnson, S. Krause, F. Marti, J. Ottarson, G. Perdikakis, L. Popielarski, J. Popielarski, M. Portillo, R. Rencsok, D. Sanderson, S. Schwarz, N. Verhanovitz, J. Vincent, J. Wlodarczak, X. Wu, J. Yurkon, A. Zeller, Q. Zhao, A. Schempp, J. Schmidt and J. Haeuser: *ReA3 - the Rare Isotope Re-Accelerator at MSU.* In *Proc. LINAC 2010,*

Tsukuba, Japan. NSCL, Michigan State University, East Lansing, MI, USA and Goethe-Universitaet, Frankfurt, Germany, 2010.

[19] Koubek, B.: *Simulationen zu Randfeldern in 4-rod RFQs*. Talk, 2012.

[20] Koubek, B., U. Bartz, A. Schempp and J. S. Schmidt: *Development of a 325 MHz 4-Rod RFQ*. In *Proc. PAC 2011, New York, NY, USA*, page 1888. IAP, Frankfurt am Main, Germany, 2011.

[21] Koubek, B., H. Podlech, A. Schempp and J. Schmidt: *Power Tests of the 325 MHz 4-rod RFQ Prototype*. In *Proc. IPAC 2013, Shanghai, China*, page 3800. IAP, Frankfurt am Main, Germany, 2013.

[22] Koubek, B., A. Schempp, J. S. Schmidt and L. Gröning: *RF Design of a 325 MHz 4-ROD RFQ*. In *Proc. IPAC 2011, San Sebastian, Spain*, page 2568. IAP, Frankfurt am Main, Germany and GSI, Darmstadt, Germany, 2011.

[23] Koubek, B., J. Schmidt and A. Schempp: *RF Setup of the MedAustron RFQ*. In *Proc. LINAC 2012, Tel-Aviv, Israel*, page 957. IAP, Frankfurt am Main, Germany, 2012.

[24] Koubek, B., J. Schmidt, A. Schempp and L. Groening: *Status of the 325 MHz 4-ROD RFQ*. In *Proc. IPAC 2012, New Orleans, Louisiana, USA*, page 3815. IAP, Frankfurt am Main, Germany and GSI, Darmstadt, Germany, 2012.

[25] Küpfmüller, K. et al.: *Theoretische Elektrotechnik*. Springer, 2008.

[26] Kurennoy, S.: *CST results: transmission vs. V profile at fixed V_{av}*. Technical Report, 2012.

[27] Kurennoy, S. S., R. W. Garnett and L. J. Rybarcyk: *Electromagnetic and multi-particle beam dynamics modeling of 4-rod RFQs*. In *Proc. IPAC 2013, Shanghai, China*, page 3978, 2013.

[28] Kurennoy, S. S., E. O. Olivias and L. J. Rybarcyk: *Design Analysis of the new LANL 4-rod RFQ*. In *Proc. NA-PAC 2013, Pasadena, CA, USA*, 2013.

[29] Leitner, D., C. Benatti, S.W. Krause, D. Morris, S. Nash, J. Ottarson, G. Perdikakis, M. Portillo, R. Rencsok, T. Ropponen, L. Tobos, N.R. Usher, D. Wang, J. Haeuser, O. K. Kester, F. Marti, E. Tanke, X. Wu, Q. Zhao, A. Schempp, J. S. Schmidt and H. Zimmermann: *Commissioning Results of the ReA RFQ at MSU.* In *Proc. PAC 2011, New York City, NY, USA*, page 1912. NSCL, East Lansing, Michigan, USA and Kress GmbH, Biebergemuend, Germany and GSI, Darmstadt, Germany and FRIB, East Lansing, Michigan, USA and IAP, Frankfurt am Main, Germany, 2011.

[30] Magnus, K., K. Popp and W. Sextro: *Schwingungen - Eine Einführung in die physikalischen Grundlagen und die theoreische Behandlung von Schwingungsproblemen.* Vieweg + Teubner Verlag, 2008.

[31] Maus, J. M.: *Untersuchungen zur Teilchendynamiksimulation in RFQs.* Master's thesis, Goethe Universität, Frankfurt am Main, 2008.

[32] Maus, J. M.: *Development of RFQ Particle Dynamics Simulation Tools and Validation with Beam Tests.* PhD thesis, Goethe Universität, Frankfurt am Main, 2010.

[33] Müller, N.: *Untersuchungen zum Funneling von Ionenstrahlen.* PhD thesis, IAP, Universität Frankfurt am Main, 2010.

[34] Nagle, D. E., E. A. Knapp and B. C. Knapp: *Coupled resonator model for standing wave accelerator tanks.* Rev. Sci. Instrum., 38(11):1583, 1967.

[35] n.n.: *Computer Simulations Technoloy: CST Microwave Studio.* Band 31 der Reihe A. Worls Scientific Series on Nonlinear Science, Singapure, 1998.

[36] n.n.: *Der FAIR-Komplex*, 2013. webpage http://www.fair-center.de/de/oeffentlichkeit.html.

[37] Palmieri, A. et al.: *Perturbation Analysis on a Four-Vane RFQ.* In Noda, A. et al. (editors): *Proc. IPAC 2010, Kyoto, Japan*, page 606, 23–28 May 2010.

[38] Piergrossi, J.: *So long, Cockcroft-Walton.* website, 2012. www.fnal.gov.

[39] Pisent, A.: *Design of the heavy-ion injector PIAVE.* In Shepard, K. (editor): *AIP Conference Proceedings 473 of Heavy Ion Technology 98 Conference*, page 214, 1998.

[40] Podlech, H., M. Grieser, R. v. Hahn, R. Repnow and D. Schwalm: *Electrodynamic Calculations of the 4-ROD-RFQ Resonator for the Heidelberg High Current Injector.* In *Proc. PAC 2001, Chicago, IL, USA*, page 3069, 2001.

[41] Rybarcyk, L. J.: *Design Requirements and Expected Performance of the New LANSCE H+ RFQ.* In *Proc. NA-PAC 2013, Pasadena, CA, USA*, 2013.

[42] Schempp, A.: *Design of Compact RFQs.* In *Proc. LINAC 1996, Geneva, Switzerland*, page 53. Institut für Angewandte Physik, Johann Wolfgang Goethe-Universität, D-60054 Frankfurt am Main, Germany, 1996.

[43] Schempp, A.: *Overview of Recent RFQ Projects.* In *Proc. LINAC 2008, Victoria, BC, Canada*, page 41. Institut für Angewandte Physik, J.W. Goethe-Universität, D-60437 Frankfurt am Main, Germany, 2008.

[44] Schempp, A. et al.: *Zero-mode-RFQ development in Frankfurt.* In Grundinger, U. et al. (editors): *Proc. LINAC 1984, Seeheim, Germany*, page 2415, 1984.

[45] Schempp, A.: *The Application of RFQs.* In *Proc. LINAC 1992, Ottawa, Ontario, Canada*, 1992.

[46] Schmidt, J. S., B. Koubek and B. Klump A. Schempp: *Tuning Studies on 4-rod RFQs.* In *Proc. LINAC 2012, Tel-Aviv, Israel*, page 963. IAP, Frankfurt am Main, Germany, 2012.

[47] Schmidt, J. S., B. Koubek and A. Schempp: *Tuning of the New 4-Rod RFQ for FNAL.* In *Proc. IPAC 2011, San Sebastian, Spain*, page 2580. IAP, Frankfurt am Main, Germany, 2011.

[48] Schmidt, J. S., B. Koubek and A. Schempp: *Tuning Studies on 4-Rod RFQs.* In *Proc. PAC 2011, New York City, NY, USA*, page 1894. IAP, Frankfurt am Main, Germany, 2011.

[49] Schmidt, J. S., B. Koubek and A. Schempp: *Simulations of the Influence of 4-Rod RFQ Elements on its Voltage Distribution.* In *Proc. IPAC 2012, New Orleans, Louisiana, USA*, page 3818. IAP, Frankfurt am Main, Germany, 2012.

[50] Schmidt, J. S., B. Koubek, A. Schempp, C. Y. Tan, D. S. Bollinger, K. L. Duel, P. R. Karns, W. A. Pellico, V. E. Scarpine, B. A. Schupbach and S. S. Kurennoy: *Investigations of the output energy deviation and other parameters during commissioning of the four-rod radio frequency quadrupole at the Fermi National Accelerator Laboratory.* Phys. Rev. ST Accel. Beams, 17:030102, Mar 2014.

[51] Schmidt, J. S., B. Koubek and A. Schmepp: *Simulations on the Boundary Fields of 4-rod RFQ Electrodes.* In *Proc. IPAC 2013, Shanghai, China*, 2013.

[52] Schmidt, J. S., J. Maus, N. Mueller, A. Schempp, O. Kester and J. Haeuser: *Tuning of the 4-Rod-RFQ for MSU.* In *Proc. IPAC 2010, Kyoto, Japan*, page 762. IAP, Univ. Frankfurt, Germany and NSCL - MSU, USA and Kress GmbH, Germany, 2010.

[53] Sieber, T.: *Entwicklung von 4-Rod- und IH- Radio-Frequenz-Quadrupol RFQ-Beschleunigern für radioaktive Ionenstrahlen bei REX-ISOLDE und MAFF.* PhD thesis, Ludwig-Maximilians-Universität München, 2001.

[54] Slater, J. C.: *Microwave Electronics.* D. van Nostrand Co. Inc., New York, 1950.

[55] Tan, C. Y. et al.: *The 750 keV RFQ INJECTOR UPGRADE.* Technical Report Beams-doc-3646-v14, Fermilab, 2013.

[56] Tan, C. Y., J. S. Schmidt and A. Schmepp: *Simple lumped circuit model applied to field flatness tuning of four-rod radio frequency quadrupoles.* Phys. Rev. ST Accel. Beams, 17:012002, 2014.

[57] Vretenar, M.: *Low-beta Structures.* In *CAS - RF for accelerators, Ebeltoft, Denmark, 2010*, 2010.

[58] Vretenar, M.: *The Radio Frequency Quadrupole.* In *CAS - Intermediate Accelerator Course, Chinos, 2011*, 2011.

[59] Wangler, T. P.: *RF Linear Accelerators.* Wiley-VHC, 2008.

[60] Weiland, T.: *A discretization method for the solution of Maxwell's equations for six-component fields.* Electronics and Communication (AEÜ), 31:116, 1977.

[61] Weiland, T.: *Time domain electromagnetic field computation with finite difference methods.* International Journal of Numerical Modelling, 9:295, 1996.

List of Figures

Danksagung

Zuallererst möchte ich meinem Doktorvater Prof. Dr. A. Schempp für seine Unterstützung während meiner Zeit in seiner Arbeitsgruppe danken. Ich habe mich immer gefördert gefühlt und viel von Ihnen gelernt. Mein Dank gilt auch Prof. Dr. O. Kester für sein Interesse an meiner Arbeit und Prof. Dr. H. Podlech für seine Unterstützung.

Bedanken möchte ich mich auch bei meiner Arbeitsgruppe M. Baschke, U. Bartz, P. Till und besonders bei meinem Bürokollegen B. Koubek, für die vielen gemeinsamen Erlebnisse. Danke auch an die Ehemaligen der AG Schempp. Ich bin froh euch alle kennen gelernt zu haben. Auch allen anderen Mitgliedern des IAP möchte ich Danke sagen, ich war wirklich gern Teil dieses Instituts. Dabei möchte ich auch unsere techn.-admin. Mitarbeiter(-innen) auch in der Werkstatt unter Leitung von S. Reploeg nicht vergessen. Vielen Dank für eure tatkräftige Unterstützung. An A. Hergt, danke dass du immer ein offenes Ohr hast. I would also like to thank the injector crew at FNAL for the great working atmosphere and especially C. Y. Tan. Thank you for expecting the best I can do, it was a pleasure to work with you. Danke auch an J. Häuser für die gute Zusammenarbeit.

Ich möchte hier auch all denen Danken, die mich in meinem Uni-Leben begleitet haben. Besonders bei M. Geese, G. Gräf, R. Märtin, B. Klump und natürlich bei meinem "Mentor" S. Vogel. Danke für all eure Unterstützung. An dieser Stelle möchte ich mich auch bei meinem Cousin T. Burschil bedanken, ich bin froh, dass du schon in der Schulzeit, aber auch im Studium und danach immer da warst. Ein riesen Dankeschön geht hier auch an T. Schlöter, P. Becker und V. Fuchs - danke, dass ihr immer für mich da seid.

Zu guter Letzt möchte ich meiner Familie und vor allem meinen Eltern einen ganz besonderen Dank aussprechen. Danke, dass Ihr immer hinter mir steht und an mich glaubt. Danke, dass ihr mir immer wieder Mut macht und für all eure liebevolle Unterstützung.